SURFACE MODIFIED HALLOYSITE NANOTUBES INCORPORATED POLYL-LACTIDE NANOCOMPOSITES FOR FOOD PACKAGING APPLICATIONS

A Thesis Submitted to
The Graduate School of Engineering and Sciences of
İzmir Institute of Technology
in Partial Fulfillment of the Requirements for the Degree of

MASTER OF SCIENCE

in Chemical Engineering

by
Ece Zeynep TÜZÜN

July 2019
İZMİR

We approve the thesis of **Ece Zeynep TÜZÜN**

Examining Committee Members:

Prof. Dr. Funda TIHMINLIOĞLU
Department of Chemical Engineering, İzmir Institute of Technology

Prof. Dr. Figen KOREL
Department of Food Engineering, İzmir Institute of Technology

Assoc. Prof. Dr. Aylin ZİYLAN
Department of Metallurgical and Materials Engineering, Dokuz Eylül University

16 July 2019

Prof. Dr. Funda TIHMINLIOĞLU
Supervisor,
Department of Chemical Engineering,
İzmir Institute of Technology

Prof. Dr. Erol ŞEKER
Head of the Department of Chemical Engineering

Prof. Dr. Aysun SOFUOĞLU
Dean of the Graduate School of Engineering and Sciences

ACKNOWLEDGMENTS

I would like to thank and express my gratitude to Prof. Dr. Funda Tıhmınlıoğlu for her supervision, guidance, support and patience throughout my thesis study.

I would like to thank Dr. Dildare Metin and Dr. Sedef Tamburacı for their help and advices during my thesis study. I would like to thank my other friends in the laboratory; Sibel Değer, Merve Perpelek, Aylin Kara and Çağlar Ersanlı for their supports.

I would like to thank Burcu Ceren Hallaç and Eczacıbaşı ESAN Co. for supplying ESAN HNT.

I would like to thank the technical staff; Ahmet Köken, Ahmet Kurul and Nazil Karaca for their sincere help during the experimental section of my thesis study. Also, I would like to thank Belgin Tunçel Kırkar for her help during optical measurements.

I would like to thank İzmir Institute of Technology, Center for Materials Research for SEM and XRD analysis. I thank to the specialists; Mutlu Devran Yaman, Zehra Sinem Yılmaz and Duygu Oğuz Kılıç for SEM-EDX training, in particular.

I would like to thank Deniz Şimşek for FTIR analysis, Nesrin Ahıpaşaoğlu for BET analysis, Şefika Çağla Sayılgan and Özgün Deliismail for TGA analysis and Ebru Kuzgunkaya for DSC analysis.

Special thanks to Zeynep Ay for her help during contact angle measurements.

I am thankful to my office mates and friends; Esin Balcı, Azime Arıkaya, Burcu Sırma, Gözde Gözel, Ayşe Metecan, Esin Gökmen, Merve Gençoğlu and Yağmur Dağa for their friendship and supports during my master study.

I am grateful to my mother Jale Akınan and my brother Kaan Sami Tüzün for their endless support for all my life.

ABSTRACT

SURFACE MODIFIED HALLOYSITE NANOTUBES REINFORCED POLYL-LACTIDE NANOCOMPOSITES FOR FOOD PACKAGING APPLICATIONS

Biodegradable Poly (L-lactide) (PLA) can replace petroleum based packaging materials to solve environmental problems. PLA lacks of ductility and have moderate barrier properties. In this study, halloysite nanotubes (HNTs) possessing unique surface chemistry and tubular structure were incorporated into PLA matrix to overcome drawbacks of PLA.

Firstly, HNT surface was modified with aminopropyltriethoxysilane (APTES) to enhance interfacial adhesion between HNTs and PLA matrix by decreasing the hydrophilicity of HNTs. Modified HNTs (m-HNTs) were characterized by SEM, FTIR, TGA, N_2 adsorption-desorption analysis, XRD and XPS. FTIR, XRD and XPS results revealed that APTES was successfully grafted onto HNTs. The optimum pH and APTES concentration for the silanization of HNTs were determined as 3.50 and 1%, respectively.

HNT/PLA and m-HNT/PLA nanocomposite films with different wt% of nanofiller loadings were prepared by solution casting. The films were characterized by FTIR, XRD, tensile test, water vapor permeation, DSC, TGA, contact angle and SEM analysis and color measurements. Better dispersion and consequently better mechanical properties were obtained with m-HNT addition compared to unmodified ones. Tensile strength at break of PLA was increased by 4.7% and 16.6% with 2 wt% HNT and m-HNT addition, respectively. m-HNT/PLA nanocomposites had better water vapor barrier properties than unmodified HNT/PLA nanocomposites while both of them improved the barrier property.

Best mechanical and water vapor barrier properties were achieved with 2% modified HNT (1% APTES) containing PLA nanocomposites. Therefore, nanocomposite films produced in this study with high transparency and good barrier property can be a suitable candidate for fresh food packaging.

ÖZET

GIDA AMBALAJI UYGULAMALARI İÇİN YÜZEY MODİFİYE HALLOYSİT NANOTÜP TAKVİYELİ POLİL-LAKTİD NANOKOMPOZİTLERİ

Biyobozunur Poli (L-laktid) (PLA), çevre sorunlarını çözmek için petrol bazlı ambalaj malzemelerinin yerini alabilir. PLA süneklikten yoksundur ve orta derecede bariyer özelliklerine sahiptir. Bu çalışmada, PLA'nın dezavantajlarının üstesinden gelmek için, özgün yüzey kimyasına ve tübüler yapıya sahip olan halloysite nanotüpler (HNT'ler) PLA matrisine dahil edilmiştir.

HNT'lerin hidrofilikliğini azaltarak HNT'ler ve PLA matrisi arasındaki arayüzey yapışmasını attırmak için HNT yüzeyi, aminopropiltiltrietoksisilan (APTES) ile modifiye edilmiştir. Modifiye HNT'ler (m-HNT'ler), SEM, FTIR, TGA, N_2 adsorpsiyon-desorpsiyon analizi, XRD ve XPS ile karakterize edilmiştir. FTIR, XRD ve XPS sonuçları APTES'in HNT'lere başarıyla aşılandığını göstermiştir. HNT'lerin silanizasyonu için optimum pH ve silan konsantrasyonu sırasıyla 3.50 ve %1 olarak belirlenmiştir.

Ağırlıkça farklı yüzdelerde modifiye edilmemiş ve modifiye edilmiş HNT içeren PLA/HNT nanokompozit filmleri çözelti dökümü ile hazırlanmıştır. Filmler FTIR, XRD, çekme testi, su buharı geçirgenliği, DSC, TGA, temas açısı ve SEM analizi ve renk ölçümleriyle karakterize edilmiştir. Modifiye edilmemiş olanlara kıyasla m-HNT ilavesi ile daha iyi dağılım ve sonuç olarak daha iyi mekanik özellikler elde edilmiştir. PLA'nın kopmasındaki çekme dayanımı, ağırlıkça %2 HNT ve m-HNT ilavesi ile sırasıyla %4.7 ve %16.6 artmıştır.

%2 modifiye edilmiş HNT (%1 APTES) içeren PLA nanokompozitleri ile en iyi mekanik ve su buharı bariyeri özellikleri elde edilmiştir. Bu nedenle, bu çalışmada üretilen yüksek şeffaflık ve iyi bariyer özelliğine sahip nanokompozit filmler, taze gıda ambalajları için uygun bir aday olabilir.

TABLE OF CONTENTS

LIST OF FIGURES

Figure **Page**

Figure **Page**

Figure **Page**

LIST OF TABLES

Table **Page**

CHAPTER 1

INTRODUCTION

Plastics are the most widely used packaging materials. Since most of packaging materials are petroleum based and non-degradable, concerns over the persistence of plastic packaging materials in the environment have led the researchers to the development of biodegradable polymers. Thus, biodegradable packaging materials can be an alternative solution to overcome environmental problems.

Among various biodegradable polymers, Poly(L-Lactide) (PLA) is the most widely used biodegradable polymer due to easy processing and availability in the market which has gained enormous attention as the replacement of conventional polymers.

PLA may have advantages over other polymers because of its biodegradability and origin from renewable resources, it also has some disadvantages such as brittleness, poor thermal stability, low toughness, and low elongation at break for a wide range of applications (Sonchaeng et al, 2018).

In order to overcome the drawbacks of biodegradable polymers, nanoparticles such as carbon nanotubes, graphite, and clays, are generally incorporated into polymer matrixfor the development of many properties of polymers. Among many of the nanofillers, nanoclays are the most commonly used nanofillers which have relatively lower price compared to carbon nanotubes. Various nanoclays in the form of layered silicates have been used in PLA polymers to enhance thermal, mechanical and barrier properties. However, property enhancement depends on the dispersion levels of layered silicates in the polymer matrix (Ray and Okamoto, 2003).

Halloysite is a natural, tubular nanoclay mineral consisting of aluminosilicate clay layers. Unit clay layers are separated by water molecules. The external surface consisting of siloxane is partially negatively charged and the internal surface consisting of Al-OH groups is partially positively charged. Tubular lumen of HNTs can be enlarged by acid or base treatments and antimicrobial agents and drugs can be loaded inside the lumen of HNTs, efficiently. Drug loading is more favorable for charged ingredients. The external

surface of HNTs can be easily coated with a positively charged polymer such as chitosan and polyethyleneimine.

Aggregation of the filler is the most encountered problem in polymeric nanocomposites. The affinity between the filler and the matrix should be high to obtain better composite properties than the neat polymer. PLA is a hydrophobic polymer and HNT is a hydrophilic nanofiller due to the large number of hydroxyl groups. Aggregation of HNTs after 5 wt% was generally observed in the literature (Kim et al, 2016). Thus, various methods including encapsulation, coating, and chemical bond formation using functional molecules are used to enhance interfacial adhesion between the nanoadditive and polymeric matrix. However, surface modification of HNTs with different silane coupling agents is the most commonly used method for enhancement of interfacial adhesion in PLA polymer. The functional groups of silane molecules form covalent bonds with nanoclays. When the nanoclay surface is covered with silane coupling agents, the clay surface become more hydrophobic and more compatible with polymer matrices.

APTES was successfully grafted onto the internal surface and the external surface defects of HNT in many studies (Peixoto et al, 2016; Yuan et al, 2012; Zeng et al, 2016; Zhang et al, 2013). Incorporation of up to 5wt% APTES-modified-HNTs into PLA matrix resulted in better dispersion, thermal and mechanical properties of PLA.

In this study, surface of HNT obtained from local source (Turkey) was modified using APTES coupling agent to enhance interfacial attraction between HNT and PLA polymer. In the preliminary studies, silanization pH and silane concentration were optimized. PLA/HNT nanocomposite films were prepared using unmodified and modified HNTs by solution casting method. Effect of HNT loading on chemical, thermal, mechanical, water vapor barrier, surface and optical properties of the nanocomposites were examined.

This report consists of six chapters. A brief summary is given in the introduction part. Information about generally used materials in food packaging, biodegradable polymers, production of PLA and important properties of PLA was mentioned in Chapter 2. Information of polymeric nanocomposites, nanoadditives used in polymeric composites, halloysite properties and surface modification of nanoclays were given in Chapter 3, experimental method and characterizations are given in Chapter 4. Results and discussions are given in Chapter 5. The last chapter, Chapter 6 includes conclusions and recommendations of the study.

CHAPTER 2

FOOD PACKAGING MATERIALS

Accelerated speed of daily life increased the demand of packed food to minimize the time consumed for nutrition, therefore, disposable food packaging materials were produced. Nowadays, the usage of these materials has become very common. Petroleum based plastic food packaging materials have been widely used and leads to serious environmental problems due to their non-degradability in nature.

A decent food packaging material should provide food safety, preserve food quality and increase shelf-life of the packed food (Rhim et al. 2013)(Sorrentino et al. 2007). Important properties of food packaging materials are listed in Figure 2.1.

The ideal food packaging material is preferred to be heat-tolerant, impermeable to gases (such as O_2 and CO_2) and water vapor, possessing good mechanical properties while preserving food quality. Impermeability to O_2 is very important because the presence of oxygen can cause quality changes such as flavor, color and odor. Furthermore, oxidation damages nutrients and may lead the growth of aerobic bacteria and molds.

Liquid water absorbable packagings are helpful to minimize moisture problems during storage to prevent growth of microorganisms on especially fresh food, frozen meat and seafood due to the water produced from respiration and melting of ice (Suppakul et al, 2003).

Among the varieties of different materials such as metal, glass or papers, petrochemical-based polymers; plastics, are the most commonly used packaging materials due to their processability, strength, durability, lightness, good heat sealability and low price. Unfortunately, the over usage of plastics causes contamination, lessen oil resources, raises oil prices and their toxic monomers and oligomers may migrate to food when used as food packaging materials (Jamshidian et al, 2010).

Polymers are formed by polycondensation or addition polymerization of monomers. Thermosets and thermoplastics are two major categories of polymers. Thermosets cannot be remolded. Conversely, thermoplastics can be returned to their original state and can be remolded. Thermoplastics can be easily shaped and molded into

various forms needed for food packaging. Plastics are easily shaped, cheap and lightweight. They have variable permeability, optical and physical properties. Residual monomer components plasticizers are safety concerns in plastic food packaging. Polyolefins and polyesters are the most commonly used plastic packaging materials. Polypropylene and polyethylene are callled polyolefin polymers. They are both easily processible, stable, moisture and chemical resistant, flexible, strong, recyclable and reusable. Polyesters are condensation polymers including Polyethylene terephthalate (PET), polyethylene naphtalate and polycarbonate. PET is the most widely used polyester in the form of bottles, jars, bags, appetizer wrappings due to its good strength, stiffness, hardness, ductility, barrier to O_2, CO_2 and moisture (Marsh & Bugusu, 2007).

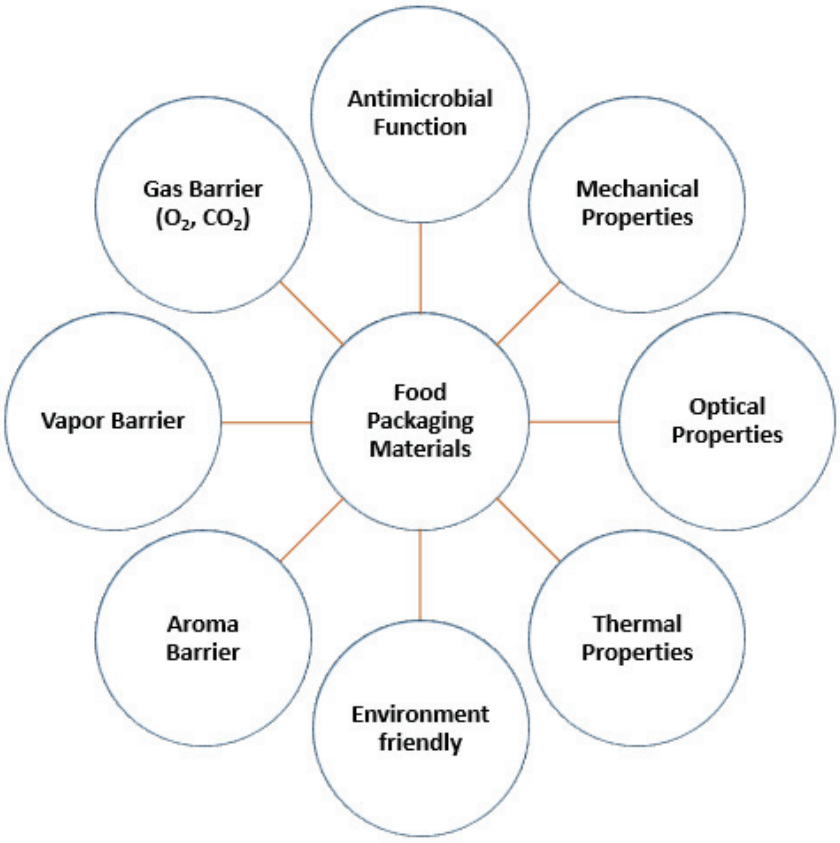

Figure 2.1. Desired Properties of Food Packaging Materials (Source: Rhim et al, 2013)

The environmental effect of the packaging materials is extremely important. Plastic wastes do not degrade in nature, they are accumulated on landfills and have become a serious problem for governments. This may cause pollution of water and soil. Mishandling of natural sources can danger natural habitats. To provide sustainability, immediate action should be taken to replace plastics with biodegradable materials.

Replacing commonly used synthetic packaging materials such as polypropylene, polyethylene, polystyrene, and polycarbonate with poly(lactic acid) or polylactide (PLA) which is a biodegradable polymer, can reduce CO_2 emissions by 75% (Jamshidian et al, 2010).

A polymer degrades CO_2, water, minerals, biomass etc. with temperature, O_2 presence, humidity and pH effecting their degradation rate and degradation products (Jamshidian et al, 2010). It is highly desired for a packaging material to be biodegradable and its degradation products to be non-toxic to the environment.

2.1. Biodegradable Polymers

Polymers obtained from plant derived feedstocks, animal sources and microbial sources which breaks into environmentally friendly products are called as biodegradable polymers.

Biopolymers can be extracted from natural sources, synthesized from bio-based monomers or produced by microorganisms or bacteria (Figure 2.2). Polysaccharides are polymers that are composed of monosaccharides as monomers bound together by glycoside linkage. Starch, chitin, chitosan and pectin are in this category. Proteins are made of amino acid monomers. Casein, silk and gelatin are examples of proteins. Polyhydroxyalkanoates (PHA), polyhydroxy-butyrate (PHB), hydroxyl-valerate (PHV), bacterial cellulose, xanthan, pullan etc. are polymers produced by microorganisms or genetically modified bacteria (Jamshidian et al, 2010).

There are numerous application areas of biodegradable polymers such as food packaging materials including disposable food packages, health care products, agricultural mulch films, drug delivery, tissue engineering scaffolds, orthopedic and dental devices (Schmidt et al, 2002).

2.1.1. Polylactide (PLA)

Polylactide isproduced by polycondensation and ring-opening polymerization of lactide or direct polymerization of lactic acid. In 1932, Carothers synthesized low molecular weight PLA for the first time by polycondensation of lactic acid. Later on, scientists were able to obtain high molecular weight PLA by ring-opening polymerization of lactide. Lactide is produced from lactic acid by fermentation of renewable agricultural resources. PLA can be hydrolyzed easily and is recyclable. Its usage reduces the volume of packaging waste on landfills. Because of these advantages, PLA is distinguished

among other biopolymers and it is a 'generally recognized as safe' (GRAS) material for food packaging applications. Only high molecular weight PLA is used in packaging industry due to its proximate optical and mechanical properties to most commonly used packaging materials (Table 2.1) (Jamshidian et al. 2010, Mehta et al. 2006).

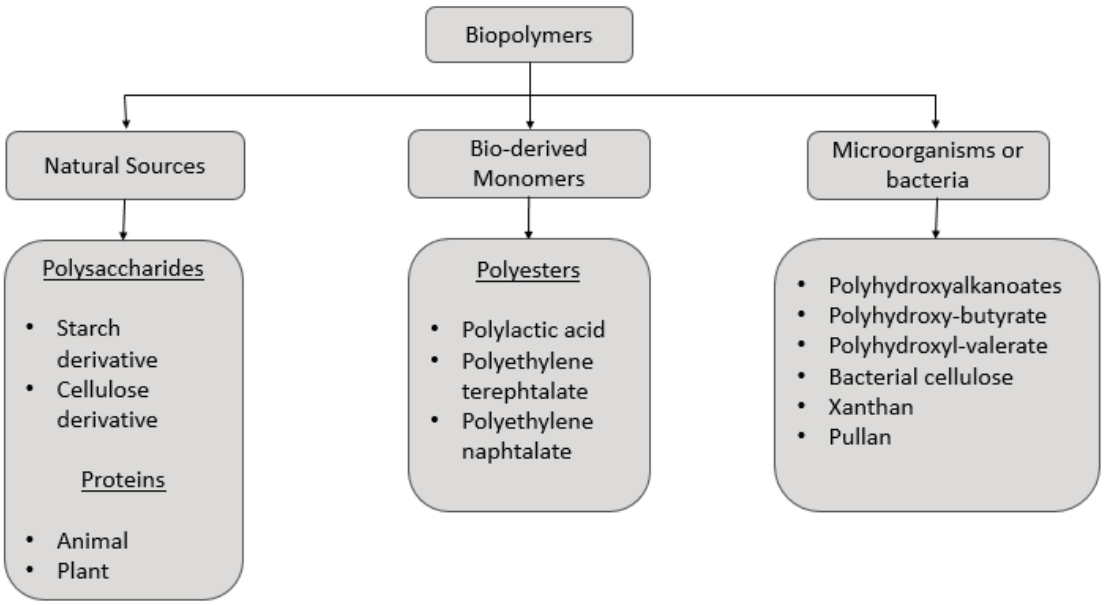

Figure 2.2. Classification of Bio-based Polymers (Thangavelu and Subramani 2016, Jamshidian et al. 2010)

PLA is a biodegradable polymer under composting conditions. However, PLA has some drawbacks such as high gas permeability, brittle nature and slow crystallization rate (Ruiz-Hitzky et al, 2014).

Table 2.1. Properties of Films (Mehta et al, 2006)

Properties	PLA	PP	PET	Nylon	Cellophane
Density (g/cm^3)	1.25	0.9	1.4	1.2	1.45
Haze (%)	2.1	1-4	2-5	2-3	1-2
Tensile strength (MPa)	109.97	189.95	204.95	249.94	89.977
Tensile Modulus (MPa)	3299.14	2399.38	3799.01	1824.53	4098.93
Ultimate Elongation (%)	160	110	140	125	23

According to Table 2.1, transparency of PLA is within the range of opacity of the most commonly used packaging materials. Its tensile strength is lower than PP and PET, tensile modulus of PLA is between PP and PET, and its % elongation at break is the best within other packaging materials (Mehta et al, 2016).

2.1.1.1. Production of Lactic Acid

Lactic acid (2-hydroxy propionic acid) is a chiral molecule possessing two stereoisomers; L-lactic acid and D-lactic acid (Figure 2.3). Lactic acid is obtained from the fermentation of corn starch and sugar cane which are 100% renewable agricultural stocks.

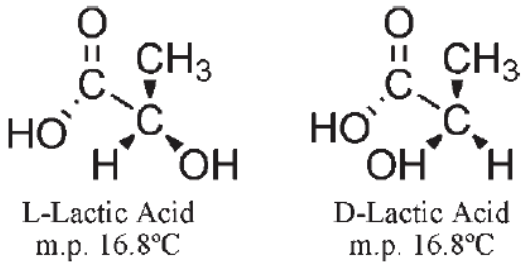

Figure 2.3. Conformational Structure of L- and D-Lactic Acid (m.p.: melting point) (Source: Auras et al, 2004)

Lactic acid is the simplest hydroxyl acid. D- and L- enantiomers of lactic acid can be produced by bacteria. Homofermentative method yields higher amount of lactic acid (1.8 moles of lactic acid/1 mole of hexose) while being accompanied by minor levels of other metabolites i.e. acetic acid, glycerol, CO_2, ethanol and mannitol compared to heterofermentative method. The yield obtained by homofermentative pathway is more than 90%. Homofermentative genus, Lactobacilli is used in this pathway. Maltose and glucose obtained from potato and corn, sucrose obtained from sugar beet or sugar cane, lactose obtained from cheese whey are used as sugar sources. With the usage of rich corn steep liquor, amino acids, B-vitamins and nucleotides are provided. Optimum process conditions are; optimum temperature: 40 °C, pH between 5.4-6.4 and low oxygen concentration. If lactic acid will be used in food derivative products or pharmaceutical applications, purification by distillation is needed (Auras et al, 2004).

2.1.1.2. Production of PLA

There are three methods applicable for high molecular weight PLA (above 100,000 Da); (1) direct condensation polymerization, (2) azeotropic dehydrative

condensation, (3) polymerization via lactide formation. Although direct condensation polymerization is the most cost effective pathway, it is not possible to obtain high molecular weight, solvent-free PLA without using expensive chain coupling agents and excipients.

High molecular weight PLA can be obtained by azeotropic dehydrative condensation without additional cost of chain extenders or adjuvants. Lactic acid is distilled at 130 °C for 2-3 hours, then the condensed water is mostly removed. Required catalyst and additive (diphenyl ester) are added. 3 Å sized molecular sieves were used to separate solvent from the polymer after additional 30-40 h at 130 °C. Then the polymer is further purified (Auras et al., 2004).

Polymerization via lactide formation was developed and patented by Cargill Dow LLC, in 1992. It is an inexpensive and continuous process. In this process, first, low molecular mass PLA is produced from the continuous condensation reaction of aqueous lactic acid. After that, the pre-polymer is converted into a mixture of lactide stereoisomers; L-lactide (L-lactic acid + L-lactic acid), D-lactide (D-lactic acid + D-lactic acid), meso-lactide (D-lactic acid + L-lactic acid) in the presence of a tin catalyst to improve rate and selectivity of the cyclization reaction. Conformational structures of lactide molecules are shown in Figure 2.4.

Subsequently, vacuum distillation is applied to purify molten lactide mixture. Eventually, using a tin catalyst, for the ring-opening polymerization of lactide in the melt, high molecular weight PLA is produced. Residual monomers are removed by evacuation and recycled back. This methodology eliminates hazardous and expensive solvent usage. Schematic representation for PLA production methods can be examined from Figure 2.5. Therefore, it is the most cost effective and the most widely used method for high molecular weight PLA production (Drumright et al, 2000).

Divergence of stereotype of the monomer results in different types of the polymer; L-PLA, D-PLA, D,L-PLA (the polymer obtained from a racemic mixture of L-lactic acid and D-lactic acid), meso-PLA (obtained from D,L-PLA, but rarely used). Since L-lactic acid is the naturally occurring form of lactic acid, L-PLA is used more frequently where good mechanical properties are needed; i.e. sutures, orthopedic devices. Disorganized structure of PDLA (amorphous) is not preferred in these applications.

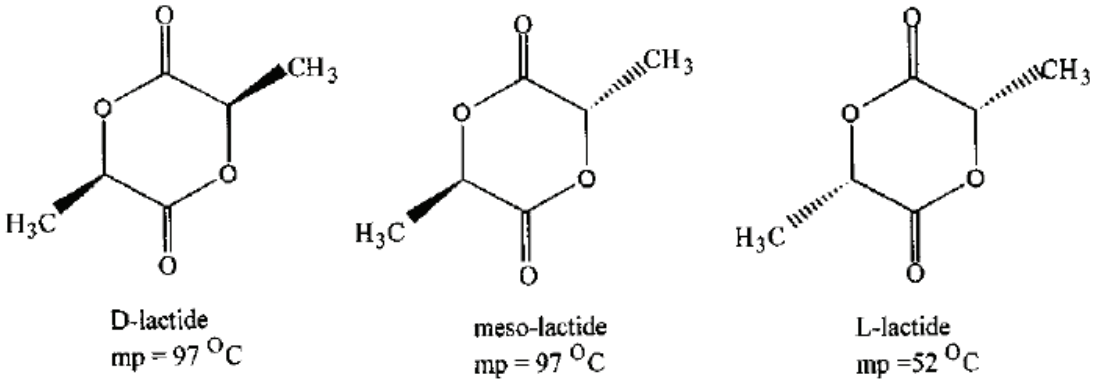

Figure 2.4. Structures of Lactide Molecules (m.p.: melting point)(Source: Garlotta, 2002)

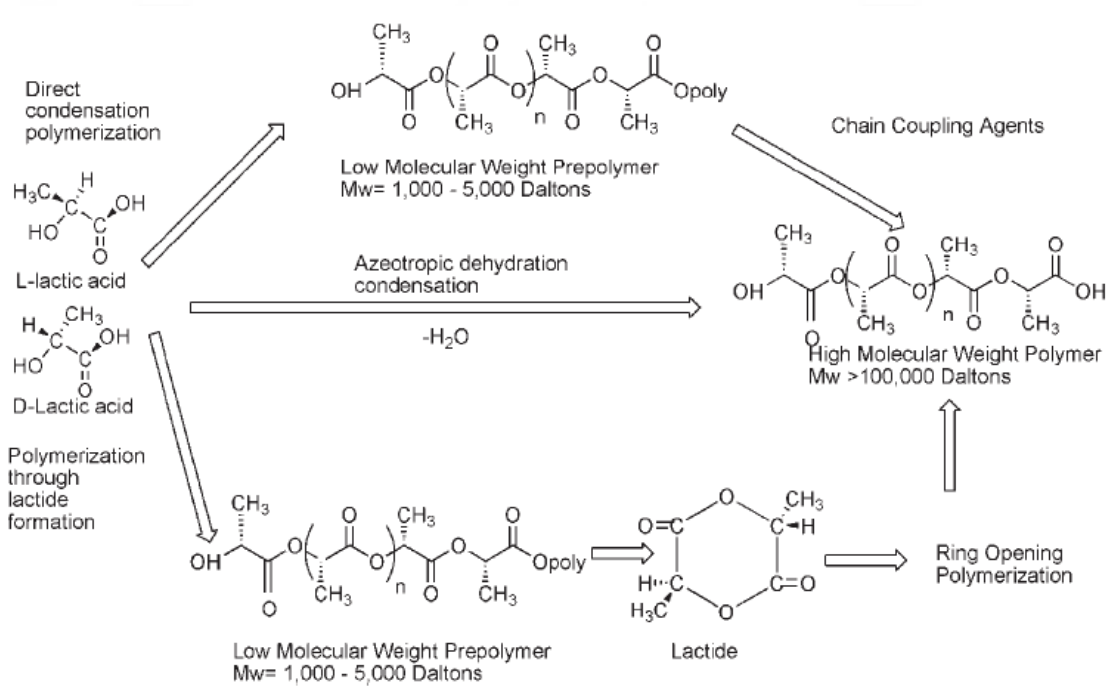

Figure 2.5. Production Methods of PLA (Source: Auras et al, 2004)

2.1.1.3. Chemical Properties of PLA

Stereotype of the monomer and polymerization conditions significantly affect extent of crystallization, tensile properties and molecular weight of the polymer. Chemical structure, chemical changes, and weak interactions of PLA can be determined using Fourier-Transform Infrared Spectra (FTIR). Chemical structure can be found in Figure 2.5 and characteristic vibration bands of PLA are listed on Table 2.2.

Ester groups in the PLA backbone gives the highest absorbance within 60-2995 cm^{-1} range. CH stretching region includes strong IR bands addressed to 2997, 2946, and 2877 cm^{-1}. C=O stretching is corresponded to the large band at 1748 cm^{-1}. CH_3 band is observed between 1500 and 1360 cm^{-1}. The peaks at 1365 and 1382 cm^{-1} are corresponding to CH asymmetric and deformation band, respectively. The peaks at 1300 and 1315 cm^{-1} are related to CH bending modes. The peaks at 1090 and 1225 cm^{-1} are assigned to C-O bonds of ester groups. The peaks at 921 and 956 cm^{-1} represent CH_3 vibrations of the backbone at rocking mode. Crystalline phase can be detected from the peak at 755 cm^{-1}. Amorphous phase can be identified from the peak at 869 cm^{-1} (Auras et al, 2004; Garlotta, 2002).

Table 2.2. Characteristic Vibration Wavenumbers of PLA for IR Spectra

Vibration	**Wavenumber (cm^{-1})**
-C-C- stretching	926, 868
-CH_3 stretching (rocking mode)	956, 921
-OH bend	1047
-C-O- stretching	1194, 1130, 1093 (asymmetric)
-C=O bend	1225
-CH- deformation (symmetric and asymmetric bend)	1382, 1365
-CH_3 bend	1456
-OC=O carbonyl stretching	1748
-CH- stretching	2997 (asymmetric), 2946 (symmetric), 2877
-OH stretching (free)	3571

2.1.1.4. Thermal and Mechanical Properties of PLA

Glass transition temperature (T_g), melting temperature (T_m) and degradation temperature are important parameters for polymers. When the glass transition temperature of a polymer is reached, polymer chains start to move and the polymer goes from a glassy state to a rubbery state. T_g of PLA effects heat capacity, density, rheological and mechanical properties of PLA (Farah et al, 2016).

If the polymer is cooled down from above T_g, it turns back to its initial state reversibly. Only semi-crystalline polymers have melting temperature. The cooling rate from above T_m, directly influences crystallinity of the polymer.

Mechanical properties of materials are obtained from stress-strain curves which are constituted under a continuous load until the material breaks. Slope of the initial linear

region of stress-strain curve is the Young's modulus. The end of the linear region is the yield of the tested material. The maximum stress the material can resist is the ultimate tensile strength of the material. Toughness is the energy needed to break the material and calculated from the area of the stress-strain curve.

Brittle materials such as glass, ceramics possess relatively low strain but higher tensile strength values. Ductile materials possess higher elongation at break and toughness but lower tensile modulus and strength.

Stress-strain curves of high and low molecular weight PLLA and PDLLA are shown in Figure 2.6. L-PLA follows a brittle trend which proves PLLA is semicrystalline. D-PLA is an amorphous polymer and show more ductile behavior. Decrease in molecular weight of the polymer results in lower tensile strength but higher toughness for both PLLA and PDLA.

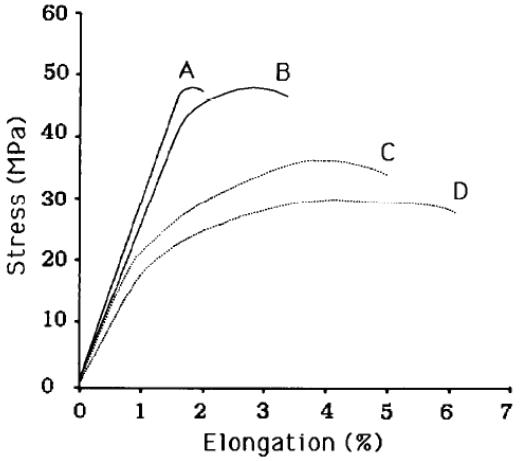

Figure 2.6. Stress-strain curves for PLA (A) PLLA (Mw: 300,000), (B) PLLA (Mw:100,000), (C) PDLLA (Mw: 550,000), (D) PDLLA (Mw: 107,000)(Source: Engelberg & Kohn, 1991)

Thermal properties data obtained from differential scanning calorimeter and tensile testing properties of PLA polymers are given in Table 2.3 (Engelberg & Kohn, 1991).

Differential scanning calorimetry is an analytical technique to determine glass transition temperature (T_g), melting temperature (T_m) and crystallization enthalpy of a polymer. Since D,L-PLA is an amorphous polymer, melting temperatures are not available for high and low molecular weight D,L-PLA. Glass transition temperatures were increased by increased chain length due to the increase in the entanglements for longer polymer chains to move. Additionally, the usage of D-lactide in the production of

PLA reduces T_g (Sonchaeng et al, 2018). Molecular mass of the polymer is highly effective on the mechanical properties of the polymer as the Young's modulus was doubled and elongation values was clearly decreased.

Table 2.3. Thermal and Mechanical Properties of PLA

Polymer	T_g (°C)	T_m (°C)	Tensile Strength (MPa)	Flexural Modulus (MPa)	Elongation at Yield (%)	Elongation at Break (%)
L-PLA (Mw:50,000)	54	170	28	1400	3.7	6.0
L-PLA (Mw:100,000)	58	159	50	3000	2.6	3.3
L-PLA (Mw:300,000)	59	178	48	3250	1.8	2.0
D,L-PLA (Mw:107,000)	51	-	29	1950	4.0	6.0
D,L-PLA (Mw:5500,000)	53	-	35	2350	3.5	5.0

2.1.1.5. Barrier Properties

PLA shows moderate barrier properties which may affect its performance as a packaging material. Similar to other properties, enantiomer compositions of lactic acid influences barrier properties of PLA. High temperature or relative humidity (RH) can increase mass transfer rate. High RH may also cause plasticization of the polymer.

Gases (small molecules) are transferred through a polymer from high chemical potential to low chemical potential (μ) to reach thermodynamic equilibrium. The chemical potential difference is the main driving force. Permeation in polymers takes place in three steps; (1) sorption of permeant onto the high potential polymer surface, (2) diffusion of the permeant through the polymer, (3) desorption of the permeant from the low potential surface of the polymer. Chemical potential of a permeant i, can be calculated from the equation 2.1;

$$\mu_i = \mu_i^0 + R \cdot T \cdot \ln a_i \qquad (2.1)$$

where μ_i^0 is the chemical potential of component i at standard state, R is the gas constant, T is the temperature (K), a_i is the activity of component i.

Concentration (c_i) can be expressed as partial pressure (p_i) in the gaseous phase. Using ideal gas law;

$$p_i = c_i \cdot R \cdot T = \frac{n_i}{V} \cdot R \cdot T \tag{2.2}$$

where n_i is the number of moles of i and V is the volume. Fugacity can be used instead of pressure for a non-ideal gas.

Assuming that the diffusion occurs only at x-direction, applying Fick's law of diffusion:

$$F = -D \cdot \frac{dc}{dx} \tag{2.3}$$

D: diffusion coefficient. At steady-state conditions, the amount of permeant passing through a polymer film per unit area per unit time is the flux (F) of the permeant which can also be described by Eq. 2.4:

$$F = \frac{Q}{A \cdot t} \tag{2.4}$$

where Q is the amount of permeant, A is the cross-sectional area of the polymer film normal to the direction of flow and t is time. If the permeant concentration is constant at both sides of the film, (dc/dx) at Eq. (2.3) may be replaced by $(c_2-c_1)/L$ (where L is the film thickness) and inserting Eq. (2.4) into Eq. (2.3) yields:

$$Q = D \cdot \frac{\left(c_1 - c_2\right) \cdot A \cdot t}{L} \tag{2.5}$$

If there is no interaction between the polymer and the permeant, Henry's law can be applied, equation (2.5) transforms into Eq. (2.6):

$$Q = D \cdot S \cdot \frac{\left(p_1 - p_2\right) \cdot A \cdot t}{L} \tag{2.6}$$

where Δp, the partial pressure difference of the permeant equals to (p_1-p_2). By rearranging Eq. (2.6), the permeability coefficient (P) of a permeant can be calculated from Eq. (2.7):

$$P = D \cdot S = \frac{Q \cdot L}{A \cdot t \cdot \left(p_1 - p_2\right)} = \frac{Q \cdot L}{A \cdot t \cdot \Delta p} \tag{2.7}$$

where P is permeability, D is coefficient of diffusion and S is the solubility. Eq. (2.7) is applicable to rubbery polymers while permeability may deviate for glassy polymers due to the chain constriction (Sonchaeng et al, 2018).

2.1.1.6. Degradation of PLA

Natural degradation process of PLA consists of two steps. First step is the hydrolysis of high molecular weight chains into oligomers. Moisture and temperature are highly effective at this stage, also acids or bases can expedite the reaction rate.

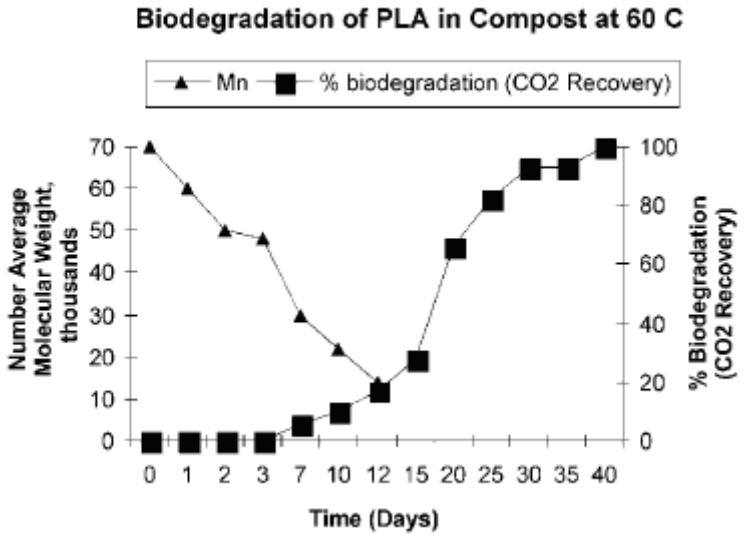

Figure 2.7. Degradation of PLA at 60 °C under composting conditions (Source: Drumright et al, 2000)

When the average molecular weight of the chains decreases below 40,000, the degradation process is continued by microorganisms in the environment by converting these low molecular weight fragments to water, CO_2 and humus. Figure 2.7 represents a typical degradation curve of PLA. Due to the ease of degradation, PLA is suitable for many applications where recovery of the product is not practically possible (Drumright et al, 2000).

CHAPTER 3

POLYMERIC NANOCOMPOSITES

Polymer based food packaging materials, especially made of biodegradable polymers may suffer from poor mechanical and barrier properties which are hindering the protection and shelf-life increments. Various types of additives are used in the production of polymer based packaging materials to enhance polymer properties. Poor dispersion or aggregation of the filler causes changes in the crystallization, transparency, thermal and mechanical properties and increase in the overall weight of the polymer. Nano-scale reinforcement instead of micron-scale fillers may preclude these problems to some extent. Layered clay or silicate minerals, carbon nanotubes, carbon black and graphene oxide are some examples of the most studied nanoadditives on the past decade.

There are three types of intercalation (represented in Figure 3.1.) between polymer matrices and fillers; tactoid dispersion, intercalated dispersion and exfoliation. If the filler and the polymer are immiscible, the type of dispersion is tactoid. Tactoid dispersion is observed in macrocomposites, besides desired improvements of the composite material are very hard to achieve. In the intercalated dispersion, polymer chains penetrate into the layers of nanofiller with the help of mixing or sonication. If exfoliated dispersion is achieved, nanofiller is distributed very well in the polymeric matrix. In this case, a continuous network is formed that enables to distribute mechanical energy uniformly to delay rupture. Besides improving mechanical properties, thermal and barrier properties are also enhanced by the barrier formed against O_2, N_2, water vapor, etc. (Dewangan & Marathe, 2018; Rouf & Kokini, 2018).

3.1. Nanocomposite Production Methods

Methods used for the preparation of nanocomposites are; (1) in situ intercalative polymerization, (2) in situ template synthesis, (3) melt extrusion, (4) solution intercalation. For solution casting, the compatibility of the nanofiller and the polymer matrix and the dispersion of the filler within the matrix are very important to provide strong interfacial adhesion between the nanofiller and the polymer.

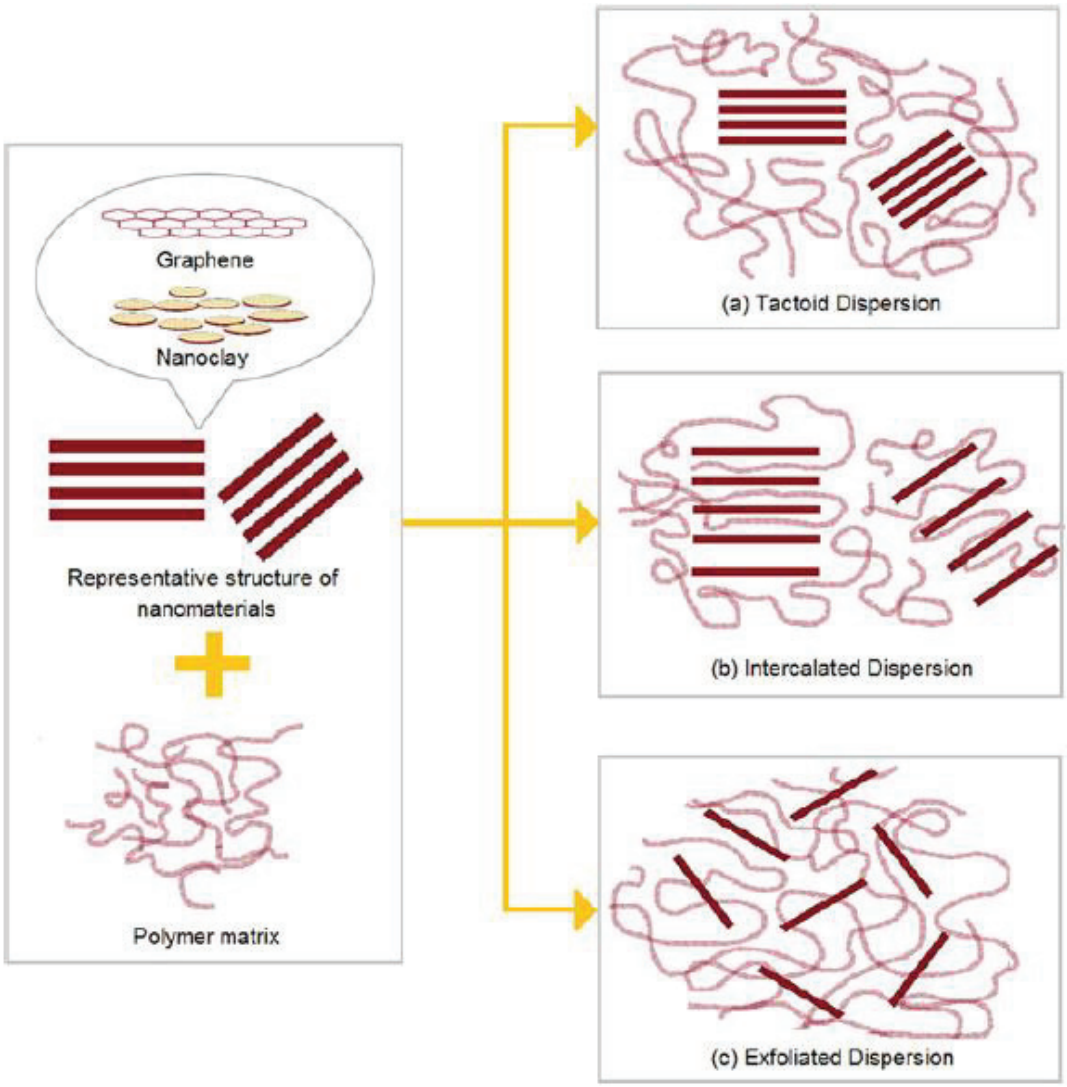

Figure 3.1. Dispersion types of the nanomaterials within polymer matrices (a) tactoid dispersion, (b) intercalated dispersion, (c) exfoliated dispersion (Source: Rouf and Kokini 2018)

3.1.1. In-situ Intercalative Polymerization

In in-situ polymerization, nanoparticles are swollen in and monomers interfere within layers of the nanofiller. Subsequently, the polymerization of the monomers takes place and the basal spacing between the layers of the nanofiller increases. To initiate the polymerization reaction heat or radiation is applied.

3.1.2. In-situ Template Synthesis

This methodology includes synthesis of clay minerals within the polymer matrix. An aqueous solution or gel which contains polymer and nanofiller building units is used.

As the inorganic crystals grow, polymer chains are trapped within the layers. Well-dispersed nanocomposites can be obtained with this method, nevertheless, the polymer can be degraded exposing to high temperature or nanomaterial may tend to aggregate as the layers grow.

3.1.3. Melt Intercalation

Melt mixing includes blending of the nanofiller and the molten polymer. If the intercalated materials are compatible with each other, exfoliated structure can be easily achieved.

3.1.4. Solution Intercalation

In the solution intercalation method, polymer chains replace a previously intercalated solvent within the layers of the nanofiller in case of negative Gibbs free energy. This technique has been mostly used with water-soluble polymers. Besides being costly, it is not an environmentally-friendly procedure due to the solvent requirement (Dewangan & Marathe, 2018).

3.2. Properties of Polymeric Nanocomposites

Permeability to water vapor and gases such as oxygen and carbon dioxide, mechanical, optical, thermal, and rheological properties of food packaging materials are critical properties for application point of view.

3.2.1. Barrier Properties of Polymeric Nanocomposites

Barrier properties of polymeric nanocomposites are significantly higher than the pristine polymer. It is easy to permeate through the voids of polymer matrices for small gas molecules. Addition of nanomaterials lengthen the diffusion path as shown in Figure 3.2, therefore, reduces permeability against gases and vapors. Exfoliated structure is less permeable than intercalated or partially exfoliated structure.

Different empirical models were developed based on the tortuosity effect to determine the permeability in nanocomposite systems. These models give about the possible structure of the nanocomposites with aspect ratio prediction.

Nielsen developed a first model based on tortuosity to predict the permeability in filled polymers. Relative permeability (P_{rel}) is given by Eq. 3.1:

$$P_{rel} = \frac{P_{nc}}{P_p} = \frac{1 - \phi_c}{\tau} \tag{3.1}$$

where P_{nc} is the permeability of the nanocomposite, P_p is the permeability of the neat polymer, ϕ_c is the volume fraction of the clay and τ is the tortuosity factor. Tortuosity factor is given in Eq. 3.2:

$$\tau = 1 + \frac{L}{2W} \cdot \phi_c \tag{3.2}$$

where L is the length and W is the width of the filler. For better prediction, Nielsen's model was modified by Lape et. al and Waché considering two dimensional trasmission of the permeant (Waché et al., 2015). Permeability models based on the assumptions and geometry of the filler is listed on Table 3.1. Aspect ratio of the nanofiller can be predicted by using these models based on the dispersion levels and the geometry of filler. It is also known that nanofillers having higher aspect raitos gave better dispersion where exfoliated structures were obtained.

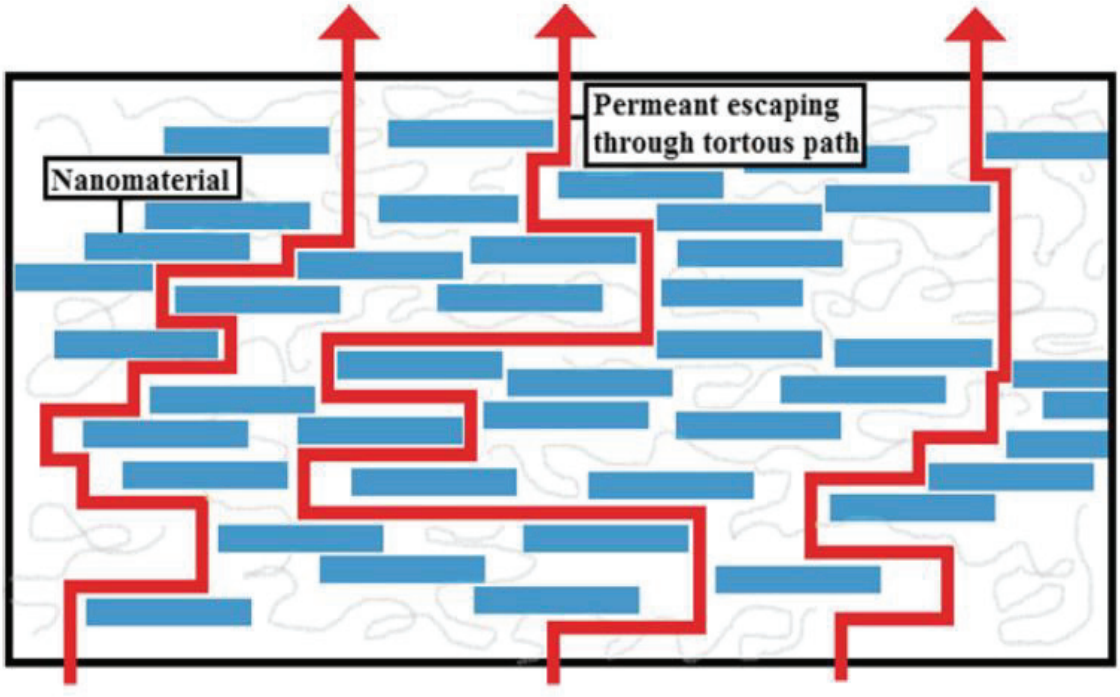

Figure 3.2. Tortuous pathway of the permeant in the nanocomposite material (Source: Rouf and Kokini 2018)

Table 3.1. Permeability Models (Source: Sun 2008)

Nielsen	Ribbon 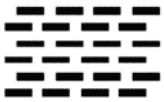	Regular array / oriented	2D	$\frac{P}{P_o} = \frac{1-\phi}{1+(\alpha/2)\phi}$
Cussler-regular array	Ribbon 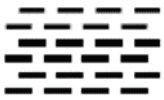	Regular array / oriented	2D	$\frac{P}{P_o} = \frac{1-\phi}{1+(\frac{\alpha}{2}\phi)^2}$
Cussler-random array	Ribbon 	Random array / oriented	2D	$\frac{P}{P_o} = \frac{1-\phi}{(1+\frac{\alpha}{3}\phi)^2}$
Bharadwai	Ribbon 	Random array / non-oriented	2D	$\frac{P}{P_o} = \frac{1-\phi}{1+\frac{\alpha}{3}\phi(S+1/2)}$

Jong-Whan Rhim prepared agar/montmorillonite (MMT) (Cloisite Na^+) composites using solution intercalation method. In the study, water vapor permeability of the neat agar film was decreased from 2.22 to 1.07 g m/m^2s Pa via 20 wt% MMT addition. Additionally, tensile strength was improved from 28.0 MPa to 36.9 MPa up to 10 wt% clay loading (Rhim, 2011).

Mohan et al. prepared corn-starch based nanocomposites with MMT (Cloisite 30B). Glycerol was used as the plasticizer. MMT formed aggregates at higher loading levels than 5 wt%. Water sorption, oxygen and water vapor transmission rates were reduced by 30-40% for 3 to 5 wt% MMT loaded films. Also, biodegradation of the corn-starch-MMT films was delayed by nanoclay addition (Mohan, Devchand, & Kanny, 2017).

Li et al. prepared MMT/PLA nanocomposites by solution intercalation. They reported a 25.9% decrease in the water vapor transmission rate of PLA (from 29.3 g/m^2.day to 21.7 g/m^2.day) when 5 wt % MMT was incorporated into PLA matrix by lengthening the diffusive path for water molecules (Li et al, 2013).

3.2.2. Mechanical Properties

Increments in the properties of the nanocomposite material such as Young's modulus, tensile strength, dimensional stability, creep resistance etc. are expected compared to the pristine polymer.

Tensile strength, flexural strength and Young's Modulus are directly influenced by high aspect ratio, exfoliated structure, and high affinity at the interface between the polymer and the nanofiller. In addition to these, mechanical properties are drastically influenced by surface area. Without increasing the mass (increase in mass can cause aggregation of nanofillers), the higher the area available for interfacial interaction, the better the dispersion. Layered silicate or nanoclays possesses a surface area of 800 m^2/g on average while nanoparticles have approximately 100 m^2/g surface area (Hanemann & Szabó, 2010).

Drown et al. prepared poly(trimethylene terephthalate)-MMT nanocomposites by melt compounding using five different types of montmorillonite differing by the compatibilizer type through production and obtained increased tensile modulus and strength but the elongation at break was decreased by half in the presence of 2 wt% clay while there was a more significant decrease for higher filler loadings (Drown et al, 2007).

PLA nanocomposites with lyophilized and activated smectite clay was prepared by Rapacz-Kmita et al. using injection molding method. Degradation and mechanical properties of PLA was enhanced by 3 wt% clay addition. Higher filler loadings lead to decrease in mechanical properties (Rapacz-Kmita et al., 2013).

Li et al. reported that the tensile strength and Young's modulus values of PLA/MMT nanocomposites were increased up to 3 wt% loading and then decreased at higher filler loadings due to agglomerations of the nanofiller. In comparison to neat PLA, they obtained a 83.8% increase (from 1.73 GPa to 3.18 GPa) in the Young's modulus of the PLA/MMT nanocomposites with 3 wt% MMT addition. Also the tensile strength was increased from 25.1 MPa to 44.1 MPa (by 76%) with 3 wt% MMT nanoclay addition (Li et al, 2013).

3.2.3. Thermal Properties

Nanoclays are generally more heat-resistant than biopolymers. Thermal stability of nanocomposites can be improved by addition of nanoclays up to clay addition generally

5% by weight. Thermal stability decreases at higher nanoclay loadings due to the aggregation of nanoparticles.

Cho et al. prepared thermoplastic polyurethane (PU) and Montmorillonite (MMT) (Cloisite 30 B) nanocomposites. Thermal, mechanical and gas barrier properties of PU was enhanced by clay addition (Cho & Kim, 2011).

3.2.4. Rheological Properties

Materials show elastic or viscous properties. Viscosity of a polymer is quite important for its suitability for processing. Rheological properties of nanocomposites are influenced by the structural properties of the additive such as particle size and shape. It was seen that polymer nanocomposites generally have solid-like behavior due to their anisotropy at lower shear rates and at low filler loadings. However, at high shear rates, shear-thinning behavior was usually observed. Viscosity of neat PLA decreases with increasing shear rate (shear-thinning behavior). High molecular weight PLA has melt viscosity between 500-1000 Pa.s at 10 to 50 reciprocal seconds (Garlotta 2002).

It is found that loss and storage modulus and complex viscosity of the nanocomposites was increasing by increasing angular frequency with nanoclay addition (Barick &Tripathy 2011).

3.2.5. Optical Properties

Transparency is an important property of composite materials for example; contact lenses and packaging materials. It is desired for a fresh food packaging to be transparent to make it clear for consumers to ensure that the product is not spoilt. When the light hits onto polymeric macro- or nanocomposites, it interferes with the additive, being scattered or absorbed by the filler which reduces the transparency of the packaging material. Percentage of haze and the light transmittance affect transparency. Polymeric nanocomposites gives better optical properties such as good transmittance and good optical clarity than the composites including macroscale fillers unless the filler loadings are very high (Loste et al. 2019; Yu et al. 2010).

Li et al. synthesized highly transparent tetraethylorthosilicate (TEOS)(core)-titania(shell)/epoxy nanocomposites possessing 87% transmittance at 800 nm with a negligible decrease in refractive index (1.52-1.54) compared to the epoxy matrix (1.54-1.55) (Li et al. 2008).

Strange et al. reported that the PLLA has itself excellent transparency and the transparency is still good when 2 wt% nanoclay (Cloisite 20A) was incorporated within the PLLA matrix (Strange et al. 2008).

3.3. Additives Used in Composite Materials

Nanomaterials are nanofillers which possess at least one nano-scale dimension. Incorporating nanomaterials into polymers can enhance strength, stiffness, heat distortion temperature of the nanocomposite materials significantly much higher than microscale additives with a lower additive content and lower the overall weight of the composite (Schmidt et al, 2002).

Nanofillers can be classified according to their origin, function etc. Classification of nanofillers can be examined from Figure 3.3.

Carbon based nanoadditives such as carbon black, graphene, graphene oxide, single- walled carbon nanotubes and multi-walled carbon nanotubes (MCWNTs) are widely used to enhance nanocomposite properties. Carbon nanotubes (CNTs) possess high tensile strength (11-63 GPa) and Young's modulus (270-950 GPa) and low density. CNTs are more promising to form exfoliated nanocomposites than nanoclays due to the hydrophobic and large surface area nature of CNTs. However, CNTs are more expensive than layered clay minerals. Graphene is also a functional nanofiller with its high electrical conductivity with sp^2 hybridized 1-atom thick carbon sheet structure (Harito et al, 2019).

Clays and layered silicates have been gained enormous attention on the last years as filler materials in composites. Nanoclays are inexpensive and widely available. Usage of nanoclays increases tortuosity and provide better gas and vapor barrier properties.

Montmorillonite (MMT) is the most widely used clay mineral in polymer-clay composites. Molinaro et al. prepared PLA nanocomposite films with various types of MMT (C10A, C20A, C30B and C93A) using extrusion. Oxygen barrier property was enhanced by 50% via C30B MMT addition. Water vapor barrier property was improved by 53% with the addition of C20A MMT (Molinaro et al, 2013).

Scarfato et al. prepared a three layered biodegradable potential food packaging film using blown-film co-extrusion. A MMT (C30B) loaded PLA layer was sandwiched between two neat PLA film layers in order to avoid direct MMT contact with the packed food. Compared to three layered neat PLA films, oxygen barrier, tensile strength and heat sealability were increased (Scarfato et al, 2015).

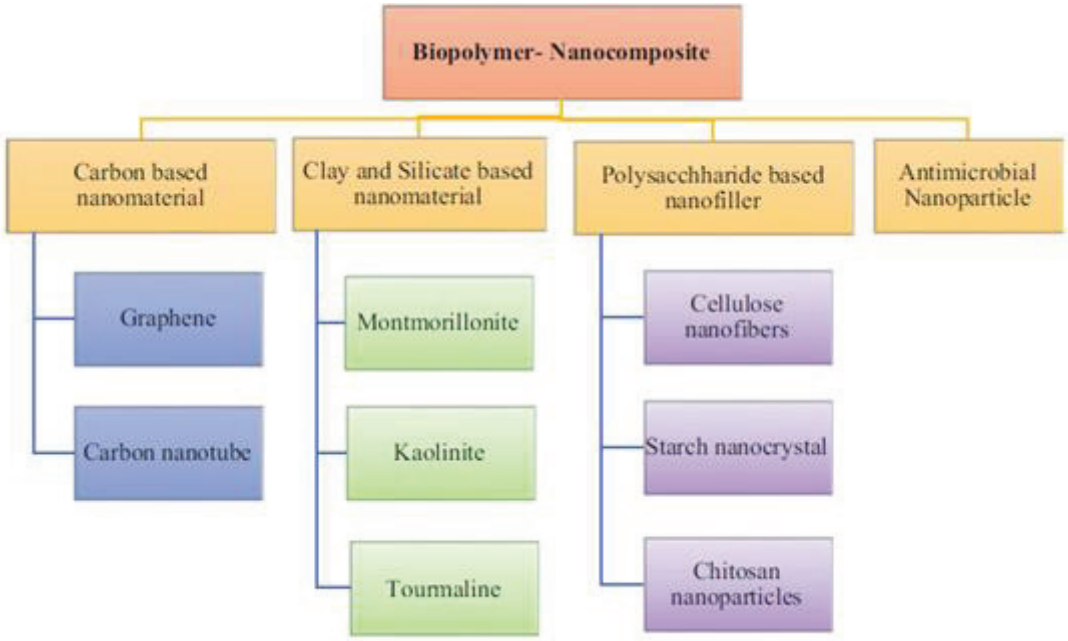

Figure 3.3. Classification of Nanomaterials used in Food Packaging (Rouf & Kokini, 2018)

Kaolinite is also a layered silicate with the chemical formula of; $Al_2Si_2O_5(OH)_4$. Kaolinite loading increased mechanical properties of starch but did not improve thermal stability. Oxygen barrier properties of PLA was enhanced by 50% with kaolinite reinforcements.

Tourmaline $[Na(Li,Al)_3Al_6(BO_3)_3$ is a hydrous silicate mineral which possesses antibacterial property against *Staphylococcus aureus* (Rouf & Kokini, 2018).

Sepiolite and palygorskite are silicate nanofillers with a high aspect ratio (around 100) and high surface area; 300 and 200 m^2/g respectively. Due to the increased interface area, these fibrous nanofillers have a very high potential to enhance mechanical properties (Ruiz-Huitzky et al., 2014). Tsai et al. improved the draw ratio of silane modified palygorskite/polyamide6 electrospun nanocomposites from 6.7 to 7.3 with an optimum filler concentration of 2 wt% with an increased filler surface area of 381 m^2/g (Tsai et al., 2012). Shafiq et al. produced linear low-density polyethylene (LDPE)/sepiolite nanocomposites by melt intercalation of unmodified and silane modified sepiolite. Sepiolite addition increased the onset temperature, ultimate tensile strength and Young's modulus while silane treatment increased interfacial adhesion (examined by SEM) and crystallinity by 5.1% (Shafiq et al, 2011). Wang et al. produced 3-aminopropyltriethoxy

silane (APTES) modified palygorskite-epoxy nanocomposites by casting onto a steel mold. Similar to LDPE/sepiolite composites prepared by Shafiq et al., APTES modified filler has enhanced mechanical properties and interfacial adhesion at 2 wt% loading (Wang et al, 2013).

Another type of layered silicate is Halloysite (HNT) which is a potential nanofiller for polymer nanocomposites.

3.3.1. Halloysite Nanotubes

Halloysite is a naturally occurring, layered, tubular clay mineral from kaolin clay family. Chemical formula of halloysite nanotubes (HNTs) is $Al_2Si_2O_5(OH)_4.nH_2O$. Halloysite is distinguished among other clays in the kaolin clay family which have a typically platy morphology by the unique structure of it. The existence of water molecules at the interlayer causes the tubular morphology. Typical dimensions of HNT are; 100-1000 nm length, 40-70 nm of outer diameter and 10-15 nm of lumen diameter. Detailed structure of HNT is given in Figure 3.4.

The structure of carbon nanotubes (CNTs) are similar to HNTs. HNTs are low-priced, environmentally-friendly, nontoxic and biocompatible nanomaterials compared to CNTs. Kaolin clay including HNTs, is classified as GRAS to be used in food packaging materials by U.S. Food and Drug Administration (FDA). Halloysite has been studied as an additive in the production of nanocomposites to enhance mechanical and barrier properties and to bring functional properties such as antioxidant, antimicrobial, and insect repellent properties (Lee et al, 2017).

There is a surface charge difference between the inner and outer layers of HNTs. The inner layer is partially positively charged due to the surface aluminol groups, the outer layer is partially negatively charged due to the siloxane groups. Antimicrobial agents and drugs can be loaded into HNTs which make HNTs suitable to be used in drug delivery, and active food packaging systems.

The tubular lumen of HNTs can be loaded by vacuum-pulling methods with active compounds. In the vacuum pulling method, HNTs are mixed with the active ingredient and sonicated. Then, the mixture is evacuated for 30 mins to remove air in the nanotubes, subsequently, air is slowly added into the vacuum chamber until atmospheric pressure is reached to push the ingredients into the lumen of HNTs. The evacuation process can be applied repetitively to increase loading efficiency (Jang et al, 2017).

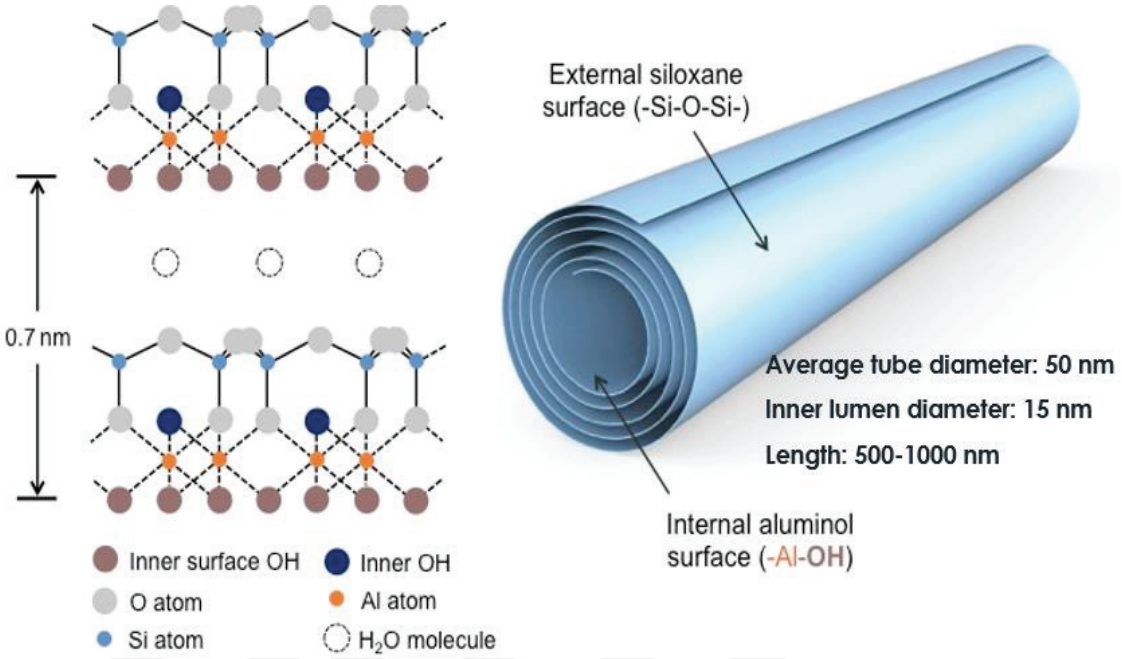

Figure 3.4. Structure of Halloysite Nanotube (Modified from WEB_1)

The tubular lumen of HNT can be enlarged up to 2-3 times its initial volume by lumen etching methods (Abdullayev et al, 2012). Usually acid treatment is applied. Usage of strong acids such as H_2SO_4 may cause the breakage HNTs at high concentrations. Weak acids such as acetic acid creates milder etching conditions (Garcia-Garcia et al. 2017).

The surface charge difference provides ease of application for multiple drug delivery and ease of loading of drugs, antioxidants, insect repellent ingredients. Oppositely charged ingredients can be easily loaded onto different surfaces of HNTs easily. Tubular morphology provides prolonged release of the ingredients (Abdullayev et al, 2012; Lvov et al, 2016).

Since the external surface of HNT is negatively charged, HNT-polymer nanocomposites with positively charged polymers represent good dispersion even at high filler contents. Liu et al. prepared chitosan-HNT nanocomposites with high filler contents up to 80 wt% HNT loading as tissue engineering scaffolds. The viscosity of chitosan decreased in the presence of 33 wt% HNT loading, due to strong interactions between the nanofiller and the matrix. There was no significant difference in the viscosity between 50 wt% HNT loaded chitosan and neat chitosan, so its processability did not affected. To obtain high loadings of drug and antimicrobial agent into HNTs with a prolonged release

is very promising. In case of CNT usage, the maximum CNT loading to preserve good dispersion is around 2 wt% and toxicity of CNTs is still contradictive (Harito et al., 2019; Liu et al, 2013).

3.3.2. Additive-Polymer Interactions

If the attractive forces are dominating between the nanofiller and the polymer, interfacial adhesion is strong, polymer chain mobility decreases and consequently tensile modulus, strength and T_g increases. In case, if repulsive forces are dominant, tensile properties decrease and T_g decreases due to the increased mobility of polymer chains. Besides, regular shape of nanofillers is a plus for the structural uniformity of polymeric nanocomposites. The rheological behavior of polymeric nanocomposites is governed by the large interfacial area as a consequence of the large specific surface area of the nanofillers and filler loading percentage.

Even at low levels of nanofiller loading, the properties of the polymer at the interface are quite different than the bulk polymer and most of the polymer can be considered as the interface polymer. Properties of the interface are critical for the overall composite properties and unique to the polymer, nanofiller and compatibilizers if used. Chain mobility is greatly influenced from the distances between the nanofillers and effect the diffusion properties. If the adhesion between nanofillers and the polymer is strong, the interfacial region is more stiff than the bulk polymer and represent a slower stress-relaxation mechanism (Schadler et al, 2007).

Nanoclay minerals consisting of hydrophilic inorganic silicate layers, tend to agglomerate in hydrophobic polymer matrices. Poor dispersion of the layered silicates may cause decrease in mechanical and optical properties. Cation or anion exchange, copolymerization with a nanoclay surface compatible polymer, or silane treatment can be used to compatibilize the nanoclay-polymer interface. If the organosilanes are polymerizable, attachment of the surface modified nanoclay onto polymer network can be achieved (Hanemann & Szabó, 2010; Schmidt et al, 2002). Penetration into strongly bonded nanofiller agglomerates is challenging for the modifiers.

Physical or chemical compatibilization methods can be utilized to enhance the interfacial adhesion. In physical methods, the surface of the nanofiller is covered by a surfactant or polymer containing a functional group by means of secondary forces. Surface modifications by chemical actions are more effective than the physical methods due to covalent bond formation (Rong et al, 2006).

3.3.3. Surface Modification with Silane Coupling Agents

Polyfunctional molecules containing two or more reactive moieties are used for surface modification. Silane reagents having the common formula of X_n-Si-$(R)_{4-n}$, where X is halide or other reactive species and R is the alkyl or organic fragment, are examples to polyfunctional molecules. Organofunctional silanes are widely used for surface modification of silicate materials in polymeric nanocomposites. R groups must be compatible with the polymer and adhere to the surface of nanoclay.

Modification with silane coupling agents occurs in two steps; first hydrolysis step, and then condensation step. In the hydrolysis step, silane coupling agents react with water to form silanols. Water content should be sufficient for the hydrolysis step. Peroxides may be used to catalyze hydrolysis reactions. In the second step, polysiloxanes are formed by the condensation of silanols and form chemical or hydrogen bonding. Acidity or basicity of the reaction medium, temperature, mixing time are other important parameters effecting silylation efficiency (Thuo, 2015; Atikler, 2004). Examples of the different common siloxane reactions are represented in Figure 3.5.

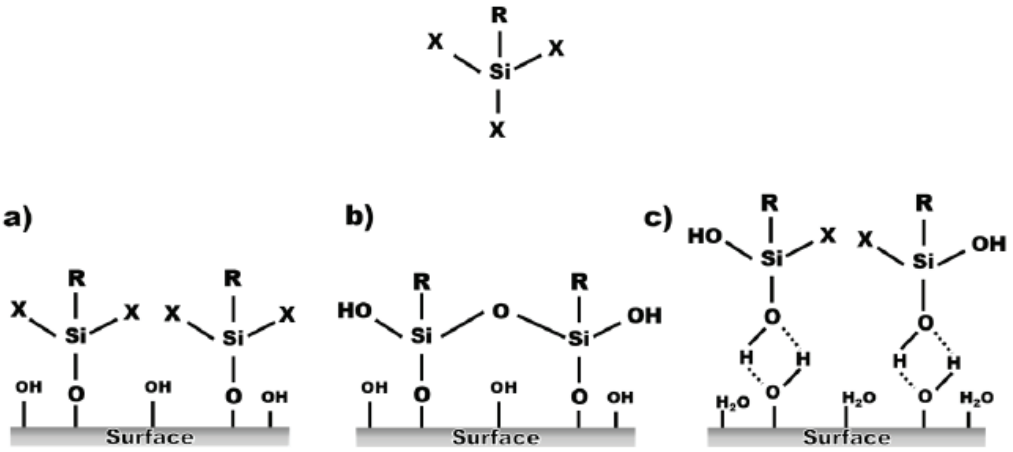

Figure 3.5. Scheme of common siloxane reactions (a,b) covalent bonding, (c) hydrogen bonding (Source: Thuo 2015)

Peixoto et al. employed silane treatment using different types of silane coupling agents. APTES, N-2-aminoethyl-3-aminopropyltrimethoxysilane (AEAPTMS), vinyltrimethoxysilane (VTMS), (3-mercaptopropyl)trimethoxysilane (MPTMS), phenyltriethoxysilane (PhTES) and (3-bromopropyl)-trimethoxysilane (BrTMS) were used in their study. Silylation efficiency was the highest when APTES coupling agent

was used (Peixoto et al., 2016). Reaction steps for the APTES modification of HNTs were represented in Figures 3.6 and 3.7.

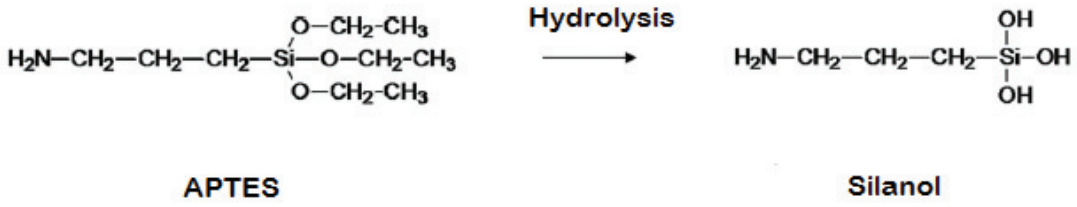

Figure 3.6. Hydrolysis of APTES (Adapted from Wang et al. 2013)

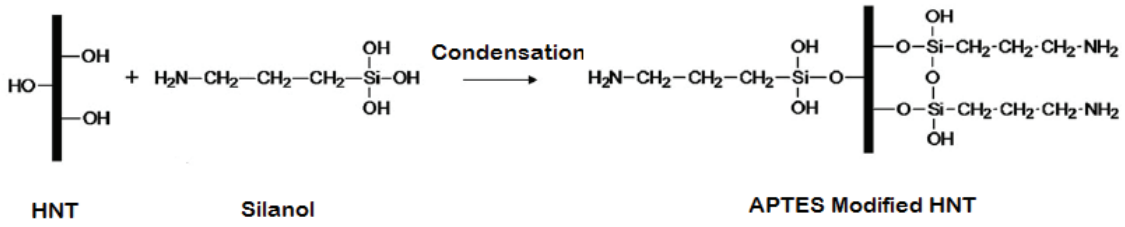

Figure 3.7. Condensation Step of APTES Modification of HNT (Adapted from Wang et al. 2013)

Grafting organic molecules onto inorganic fillers increases the interfacial affinity between the filler and the polymeric matrix. Kim et al. prepared APTES modified MMT incorporated PP films compatibilized with maleic anhydride grafted PP. The affinity between PP matrix and the clay was enhanced by APTES treatment. Improvement in the dispersion was obtained by APTES modified MMT (Kim et al, 2016).

Literature studies for various application areas with APTES modified HNTs are listed on Table 3.2.

3.4. PLA-HNT Nanocomposites

Nanoclay addition to PLA is widely studied to overcome low thermal stability, brittleness and low toughness of PLA. Similar to other composites, the most applied method is the melt intercalation for the production of PLA-HNT nanocomposites. Kim et al. studied the effects of HNT loading on the thermal and mechanical properties of the PLA/HNT nanocomposites. HNT/PLA nanocomposites were fabricated by melt-blending with five different clay levels (1, 3, 5, 7, and 9 wt %). TEM images are shown in Figure 3.8.

HNTs were well-dispersed in the PLA matrix at low loading levels. At 5 wt % loading, tensile strength was slightly decreased from 59 MPa to 56 MPa, strain at break was tripled and toughness was improved significantly. Agglomerations formed after 5 wt % loading. Surface modification of the nanotubes may be applied to enhance compatibility of HNTs with PLA (Kim et al., 2016).

Graft polymerization can be used to modify HNTs instead of blending PLA with other polymers to compatibilize HNTs and PLA matrix. Luo and coworkers surface grafted HNTs with PLLA oligomer under microwave irradiation and then blended with PLLA matrix to enhance the compatibility of HNT and PLA. The HNTs/PLLA and grafted-HNTs/PLLA (g-HNTs/PLLA) nano-composites with various amounts (5, 10, 20 and 40 wt%) by solution casting method. The grafted PLLA chains on the surfaces of HNTs improved the adhesive strength between the g-HNTs and the polymer matrix. The enhanced interaction among g-HNTs and PLLA matrix resulted in a better tensile strength and modulus compared to the pristine PLLA and HNTs/PLLA. Cell culture results indicated that g-HNTs promoted both adhesion and proliferation of M3T3 fibroblasts on the g-HNTs/PLLA composite film (Luo et al. 2013).

Wu et al. produced HNT-PLA nanocomposites by melt blending and thereafter neat PLA and HNT/PLA was foamed for the first time with supercritical CO_2. Good dispersion was achieved. The thermal stability was decreased due to the release of the absorbed water from HNTs. HNT incorporation improved the Young's modulus of PLA significantly. Supercritical CO_2 usage as a blowing agent is devastating to constitute a highly porous biomedical scaffold structure and the method does not require hazardous solvent usage but the risk originated from high pressure should be taken into account. Compared with neat PLA foam, PLA/HNT nanocomposite foams showed much higher cell density and smaller cell size due to HNT serving as the heterogeneous nucleating agents (Wu et al, 2013).

Xu et al. grafted L-lactic acid and poly (L-lactide) onto HNTs separately by direct condensation polymerization and nanocomposites were prepared by solution casting. The interfacial adhesion was increased and better dispersion of HNTs was obtained in both cases. Better grafting yield and tensile properties was reached with the poly(L-lactide) grafted HNTs (Xu et al, 2015).

Luo et al. firstly prepared polydopamine coated HNT (D-HNT) by oxidative polymerization of polydopamine. Fiber membranes consisting of PLLA/HNT and PLLA/D-HNT was produced by electrospinning. Polydopamine treated HNTs showed

better affinity with PLLA matrix than the unmodified HNTs, therefore, higher strength and higher modulus Cell adhesion and proliferation was also the best for polydopamine coated HNTs/PLLA nanocomposites (Luo et al, 2016).

Table 3.2. APTES Modified HNT Studies

Purpose	**Method**	**Important Outcomes**	**Author & Year**
Modification of different types of clays	3 Types of HNT and kaolinite was surface modified with APTES dissolved in dry toluene and refluxed at 120 °C for 20 h.	In addition to surface grafting, APTES was self-condensed via hydrolysis and formed H-bonds resulting in further enhancement of interfacial adhesion. Grafting was more successful with HNT due to higher number of surface –OH groups than kaolinite.	(Yuan et al., 2008)
Gene Therapy	Fluorescent-labeled antisense oligo-deoxylucleotides (ADONS) loaded APTES modified HNT	APTES-Modified-HNT-ADONS complex have very high potential to improve intracellular delivery and antitumor activity.	(Shi, Tian, Zhang, Shen, & Jia, 2011)
Prolonged dye release	Hydrophilic and anionic dye encapsulation in HNTs	The dye loading efficiency is increased with APTES modification by 32%. Lowering pH from 10 to 3.5 lead to three times prolonged dye release.	(Yuan, Southon, et al., 2012)
Catalytic activity	Palladium (Pd) was deposited on HNTs	Pd deposited on modified HNTs showed more uniform distribution and higher catalytic activity in the hydrogenation of styrene.	(Zhang et al. 2013)

Table 3.2. (Cont'd)

Purpose	Method	Important Outcomes	Author & Year
Polymeric Nanocomposites	Modified HNT-Polyamide6 nanocomposites produced by extrusion	Relatively low concentration of APTES and pH of the solution gave better silanization efficiency. Better interfacial adhesion and tensile properties.	(Erdogan et al, 2014)
Drug delivery	Chitosan-alginate Layer-by-layer self-assembly nanocomposties with lumen etched (H_2SO_4) and modified HNT nanocomposites	Increased Loading Capacity, Decreased drug release rate	(Li et al. 2016)
Ultrafiltation membrane for oil-water separation	Modified-HNT/poly(vinylidene fluoride) ultrafiltration membranes	Increased pure water outflow with modification due to homogeneous dispersion, Increased oil rejection	(Zeng et al., 2016)
Corrosion Inhibitor	Epoxy nanocomposites of corrosion inhibitor encapsulated TEOS+APTES modified HNTs	pH-controlled release of the corrosion inhibitor Long-term protection from metal corrosion	(Hemmatpour, Haddadi-asl, & Roghani-mamaqani, 2015)

HNTs are functional nanotubes with their unique surface chemistry and structure. Since HNTs are very hydrophilic, hydrophilic drugs can be easily loaded into HNT lumen. Zhang et al. designed a multiple drug-delivery system by electrospinning for burn treatments. Electrospun mats of hydrophilic drug (polymyxin B sulphate) encapsulated HNTs and hydrophobic drug (dexamethasone) incorporated PLLA was prepared. HNTs were uniformly dispersed in the PLLA matrix. No inhibition zones were observed against gram positive and gram negative bacteria. Immunohistochemical analysis have shown

that wound healing can be enhanced by 5 wt% HNT/PLLA nanofiber mats due to the lower cytokine formation (Zhang et al, 2015).

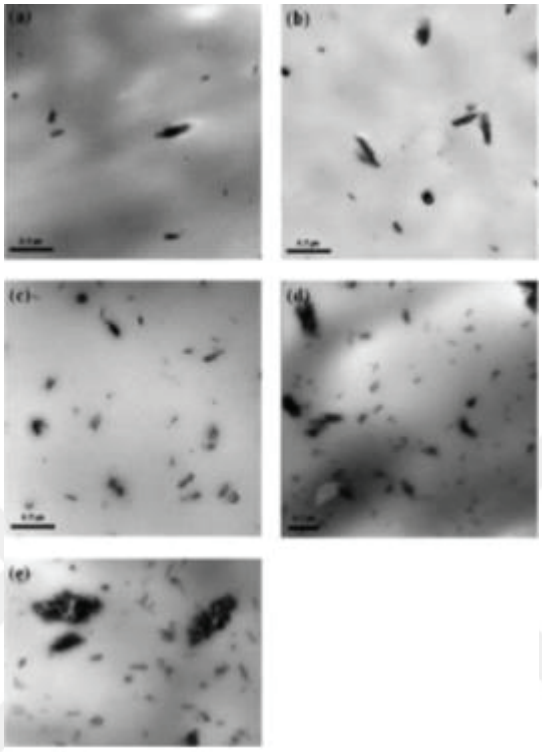

Figure 3.8. TEM images of PLA/HNT nanocomposites. (a) 1 wt%, (b) 3 wt%, (c) 5 wt%, (d) 7 wt%, and (e) 9 wt%. (Kim et al., 2016)

Pluta et al. added N,N'ethylene-bis-stearamide (ES) treated HNTs into PLA by compression molding then rapid quenching applied. HNT loading significantly affected the light transmittance and the storage modulus. However, ES treated HNTs decreased the storage modulus. ES modification improved the dispersion of HNTs (Pluta et al., 2017).

In another studies, aminopropyltriethoxy silane (APTES) modified halloysite nanotubes incorporated PLA nanocomposites were prepared by melt-compounding (Krishnaiah et al, 2017; Chen et al, 2018). Surface modification method differs by the reaction temperature, pH and the solvent mixture used.

Krishnaiah et al. reported that interfacial adhesion between HNT and PLA matrix was increased and tensile strength improvement by 26.5% was achieved with 4 wt% of modified HNT addition compared to 4 wt% unmodified HNT/PLA nanocomposite. 8 wt% modified HNT addition resulted in 20% increase in the Young's modulus, increase

in the storage modulus by 10% and elastic properties of PLA/HNT nanocomposites were enhanced. Additionally, they reported improvements in thermal stability by 17 ºC and in crystallinity by 10% (Krishnaiah et al, 2017).

Chen et al. reported that better dispersion was obtained by modified HNT incorporated PLA nanocomposites compared to unmodified HNT containing PLA nanocomposites. 12.9% increase with 5 wt% unmodified HNT loading and 25% increase with 5 wt% HNT loading in the tensile modulus were observed. Modified HNTs acted as nucleating agents and improved crystallinity. They also reported that modified-HNT/PLA nanocomposites were suitable to be used as coronary stent materials because the nanocomposites preserve their strength up to 6 months and then, degrade (Chen et al., 2018).

CHAPTER 4

MATERIALS AND METHODS

Materials used in surface modification and film preparation are given in section 4.1. Experimental methodology and characterizations are given in section 4.2.

4.1. Materials

Ingeo 2003D PLA with a specific gravity of 1.24 from NatureWorks were used as the polymeric matrix material. HNT (EHO-01) was kindly supplied from ESAN Eczacıbaşı Co. APTES with 0.946 g/mL density and 99% purity was purchased from Merck Co. Chloroform was used as the solvent to dissolve PLA. Absolute grade ethanol, ultrapure water and acetic acid were used as the solvent mixture for the surface modification of HNT.

4.2. Experimental Method

Experimental method section consists of three sections; (1) HNT modification with APTES, (2) film preparation, (3) characterization of nanoclays and (4) characterization of films.

4.2.1. Surface Modification of HNT with APTES

HNT was dried at 100 °C for 24h in a vacuum oven. 100 mL of 95% (v/v) ethanol/water solutions were prepared. pH of the solutions was adjusted by adding acetic acid. HNT was added to each solution and mixed for 1 hour. Then, APTES was added to the solutions. Temperature of the solutions was kept between 60-70 °C while mixing for 2h. Vacuum filtration was done and modified HNTs (m-HNTs) were washed with ethanol twice and m-HNTs were left to dry at room temperature overnight. Subsequently, modified HNTs were dried in a vacuum oven at 100 °C for 24h.

4.2.2. Film Preparation

Prior to process, PLA was dried at 65 °C for 24h. PLA was dissolved in chloroform (5% (w/v)). Dried (24h at 100 °C) unmodified HNTs or m-HNTs were dispersed in chloroform and sonicated for 30 min. Sonicated HNTs subsequently added to the PLA solution. HNT or m-HNT to PLA ratio was 0, 2, 4, 6 and 8 wt %. Then, PLA and HNT mixture was sonicated for 30 min. Subsequently, films were casted on glass petri dishes, left to dry for 2 days in a fume hood, then caps of the petri dishes were removed and films were continuously dried in the fume hood for 2.5 days. Afterwards, films were removed from petri dishes using a small amount of ultrapure water and right after, they were put in a vacuum oven and dried for 48 h at 70 °C.

4.2.3. Characterization of Nanoclays

Unmodified HNT and m-HNTs were characterized by scanning electron microscopy, X-ray fluorescence spectrometry, X-ray photoelectron spectroscopy, X-ray diffraction, Fourier transform infrared spectroscopy, N_2 adsorption-desorption analysis, and thermogravimetric analysis.

4.2.3.1. Morphology of Nanoclays

Morphology of the nanoclays were determined using SEM and nitrogen adsorption-desorption analysis.

4.2.3.1.1. Scanning Electron Microscopy (SEM)

Morphology of unmodified and modified HNTs were examined by scanning electron microscopy (SEM) using the secondary electron detector of a FEI QUANTA 250 FEG scanning electron microscope.

4.2.3.1.2. N_2 Adsorption-Desorption Analysis (BET)

N_2 adsorption-desorption analysis was performed with a Micromeritics Gemini V device to determine the changes in Braun-Emmet-Teller (BET) surface area, pore volume, pore diameter and adsorption-desorption isotherms.

4.2.3.2. Chemical Properties of Nanoclays

Chemical properties of modified and unmodified HNTs were investigated using XPS, XRD and FTIR.

4.2.3.2.1. X-Ray Photoelectron Spectroscopy (XPS)

XPS was used to describe elemental composition of nanoclay samples with a Thermo Scientific K-Alpha X-ray photoelectron spectrometer using 1486.68 eV X-ray source with 300 μm X-ray spot. Two points were scanned for each sample.

4.3.2.2.2. X-Ray Diffraction (XRD)

To describe the effect of surface modification, XRD analysis was performed between 2θ = 3-80° using Philips X'pert Pro XRD analyzer with a scanning rate of 0.02°/min. Bragg's law (Eq. 4.1) was used to determine the d-spacing (the interlayer distance between the layers of HNT).

$$\lambda = 2d \cdot \sin\theta \tag{4.1}$$

λ is the wavelength of the X-ray sent on the samples, θ is the diffraction angle.

4.3.2.2.3. Fourier Transform Infrared Spectroscopy (FTIR)

To determine chemical structures of nanotubes and APTES, FTIR analysis was done using a Shimadzu IRPrestige-21 FTIR-8400S FTIR spectrometer. 3 mg of HNTs were mixed with 147 mg of KBr and pelletized for FTIR analysis. Samples were scanned within 400 to 4000 cm^{-1} wavelength range.

4.3.2.4. Thermal Properties

Thermal properties of the nanotubes were determined by thermogravimetric analysis.

4.3.2.4.1. Thermogravimetric Analysis (TGA)

Thermal stability of the nanotubes was investigated using a Shimadzu TGA-51 Seteram thermogravimetric analyzer from room temperature to 800 ºC, by 10 ºC/min heating rate under 20 mL/min N_2 atmosphere with using approximately 10-12 grams of each sample.

4.3.3. Characterization of Films

Nanocomposite films were characterized by FTIR,XRD, mechanical test, water vapor permeation test, differential scanning calorimetry, TGA, SEM, contact angle and color measurements.

4.3.3.1. Chemical Properties

Chemical properties of the nanocomposite films were determined by FTIR analysis.

4.3.3.1.1. FTIR

Changes in the chemical structure of PLA and interactions between PLA and HNT/mHNTs were examined by FTIR using a Shimadzu IRPrestige-21 FTIR-8400S FTIR spectrometer.

4.3.3.1.2. XRD

Chemical properties and crystallinity of HNT/PLA nanocomposite films were determined by XRD analysis using a Philips X'pert Pro XRD analyzer with a scanning rate of 0.01°/min within a 2theta range of 5-45°.

4.3.3.2. Mechanical Properties

Mechanical properties of the PLA-HNT nanocomposites were investigated using a texture analyzer (TA XT Plus) according to ASTM D882 standards. Prior to testing, (1 cm) x (9 cm) specimens were exposed to 50% relative humidity at 25 ºC for 24h. Tensile test was done with a testing speed of 5 mm/min. At least 5 specimens were tested.

4.3.3.3. Transport Properties

Transport properties of the PLA/HNT nanocomposite films were determined by water vapor permeability analysis.

4.3.3.3.1. Water Vapor Permeability (WVP)

Water vapor permeability of the nanocomposite films were investigated using MOCON Permatran-W permeability tester. Schematic representation of the tester is given in Figure 4.1. (3cm) x (3cm) nanocomposite film samples were masked with aluminum sheets leaving 5 cm^2 sample area at the middle for testing. The device consists of two chambers. Relative humidity (RH) is adjusted to 90% at the outside chamber. Nitrogen, the carrier gas, is sent to the inside chamber. N_2 carries the water vapor passing through the film to the sensor at the inside chamber and the water vapor transmission rate (WVTR) is reported.

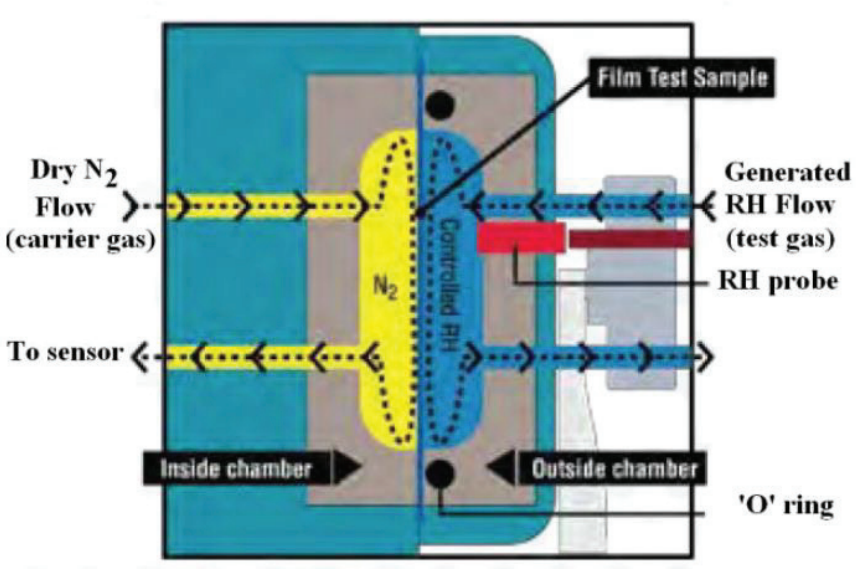

Figure 4.1. Working Principle of MOCON Permatran (Source: MOCON Manual Book)

Permeance of the nanocomposite films was calculated using Eq. 4.2:

$$\text{Permeance} = \frac{\text{WVTR}}{S\left(R_1 - R_2\right)} \tag{4.2}$$

where R_1 is the relative humidity at the outside chamber (~90%), R_2 is the relative humidity at the inside chamber (0%) and S is the vapor pressure at the test temperature (37.8 ºC).

Finally, permeability was calculated using Eq. 4.3:

$$\text{Permeability} = \text{Permeance} \cdot \text{Thicknes} \tag{4.3}$$

4.3.3.4. Thermal Properties of Nanocomposite Films

Thermal properties of the nanocomposite films were determined by differential scanning calorimetry and thermogravimetric analysis.

4.3.3.4.1. Differential Scanning Calorimetry (DSC)

Glass transition, melting and degradation temperatures and crystallinity of PLA and nanocomposite films were determined by differential scanning calorimetry (DSC) (TA Instruments Q10). For the measurements, three steps were followed:

(1) heating from 25 to 200 ºC,

(2) cooling from 200 to 25 ºC,

(3) heating from 25 to 400 ºC with a heating and cooling rate of 10 ºC/min.

4.3.3.4.2. Thermogravimetric Analysis (TGA)

Thermal stability of the nanocomposite films was investigated using a Shimadzu TGA-51 Seteram thermogravimetric analyzer from room temperature to 400 ºC, by 10 ºC/min heating rate under 20 mL/min N_2 atmosphere with approximately 10-12 grams of each sample.

4.3.3.5. Surface Wettability

Surface wettability of the nanocomposite films were investigated by contact angle measurements.

4.3.3.5.1. Contact Angle

The hydrophobicity of the nanocomposite films was determined by contact angle analysis using Attension Theta Optical Tensiometer, KSV with an ultrapure droplet size of 3 µl. At least 10 measurements were done for each sample.

4.3.3.6. Optical Properties

Optical properties of the nanocomposite films were determined by color measurements.

4.3.3.6.1. Color Measurements

The color measurements of PLA and PLA-HNT nanocomposite films were performed using a Avantis, AvaSoft 6.2 color measurement device. The total color difference was determined using Eq. 4.4:

$$\Delta E = \sqrt{(\Delta L)^2 + (\Delta a)^2 + (\Delta b)^2} \quad (4.4)$$

where ΔE is the total color difference, L is the lightness (ranging from black to white), a is the chromatic coordinate ranging from greenness to redness and b is the chromatic coordinate ranging from blueness to yellowness.

4.3.3.7. Morphology of the Fracture Surface

Dispersion of HNT and m-HNTs in PLA matrix was investigated by SEM analysis.

4.3.3.7.1. SEM

The dispersion of the nanoclay in the polymer matrix and the fracture surface of the polymer were examined using a FEI QUANTA 250 FEG scanning electron microscope by examining the cross sectional rupture areas after tensile testing.

CHAPTER 5

RESULTS AND DISCUSSION

In this study, HNTs were surface modified with APTES to improve the interaction between PLA and HNT to alter the compatibility between HNTs and the polymeric matrix. Results of the surface modification of HNTs are given first. Then, the results of the characterization of PLA-HNT nanocomposite films are reported next in this chapter.

5.1. Optimization of pH and APTES Concentration

In the preliminary studies, the surface of halloysite nanotubes were modified with APTES coupling agent at different pH and silane concentrations (Table 5.1).

Table 5.1. Silane Concentration and pH of the Samples

Sample Code	**Silane (APTES) Concentration (v/w)%**	**pH**
HNT	0	-
S1-3.50	1	3.50
S1-4.00	1	4.00
S1-4.50	1	4.50
S15-3.50	15	3.50
S15-4.00	15	4.00
S15-4.50	15	4.50
S30-3.50	30	3.50
S30-4.00	30	4.00
S30-4.50	30	4.50

5.1.1. Results for the Surface Modification of Halloysite with APTES

Modified and unmodified halloysite nanotubes at different pH and silane concentrations were characterized by SEM, FTIR, and TGA.

5.1.1.1. SEM

Scanning electron micrographs of HNTs and m-HNTs under a voltage of 5.0 kV at 50,000x magnification are given in Figure 5.1.

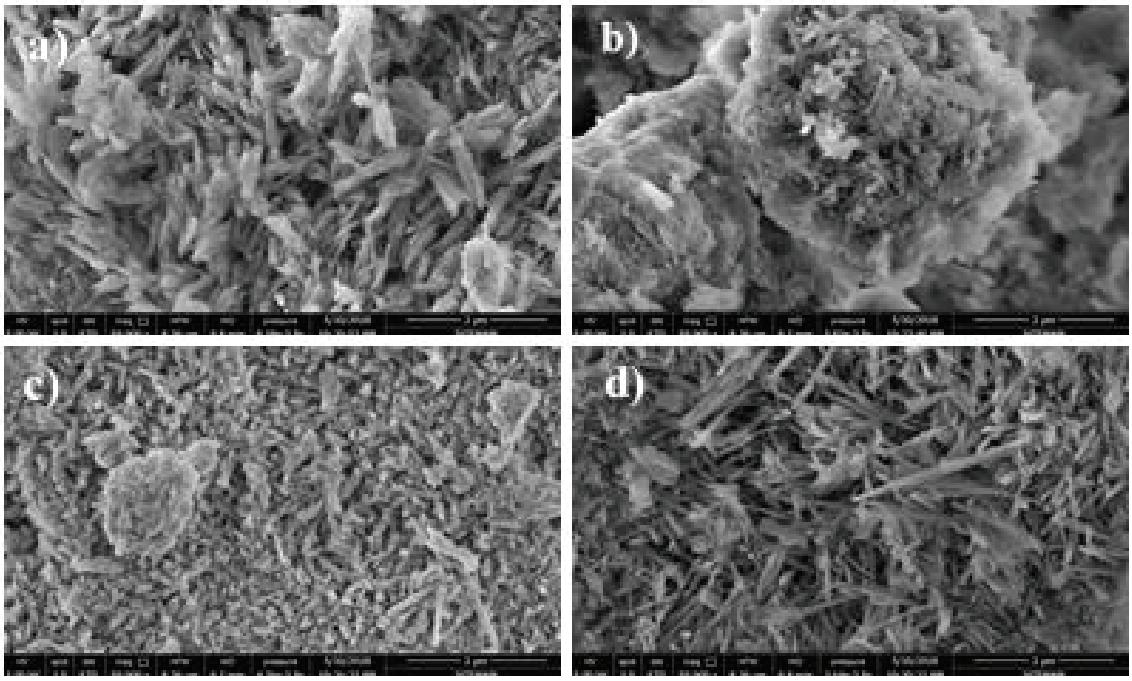

Figure 5.1. SEM Images of (a) HNT, (b) S1-3.50, (c) S15-3.50, (d) S30-3.50

According to Figure 5.1, HNT morphology changed after silanization especially for S1-3.50 sample. There is no clear change for S30-3.50 sample, apart from that the styloid structure of m-HNTs is clearer than the unmodified HNT, probably due to washing with ethanol following the modification.

5.1.1.2. FTIR

FTIR spectra of nanoclay samples were shown in Figures 5.2 and 5.3. According to Figure 5.2, peak intensities at 3695 cm^{-1} (-OH stretching of inner surface OH groups), 3600 cm^{-1} (-OH stretching of inner OH groups) were decreased indicating coating with APTES from the inner surface, edges and surface defects of HNTs. Peak intensity indicating water presence at 1630 cm^{-1} (O-H stretching of water) were decreased with the

decreased pH, which means that HNT surface become more hydrophobic due to silane modification with APTES coupling agent. Decreased pH lead to better silanization.

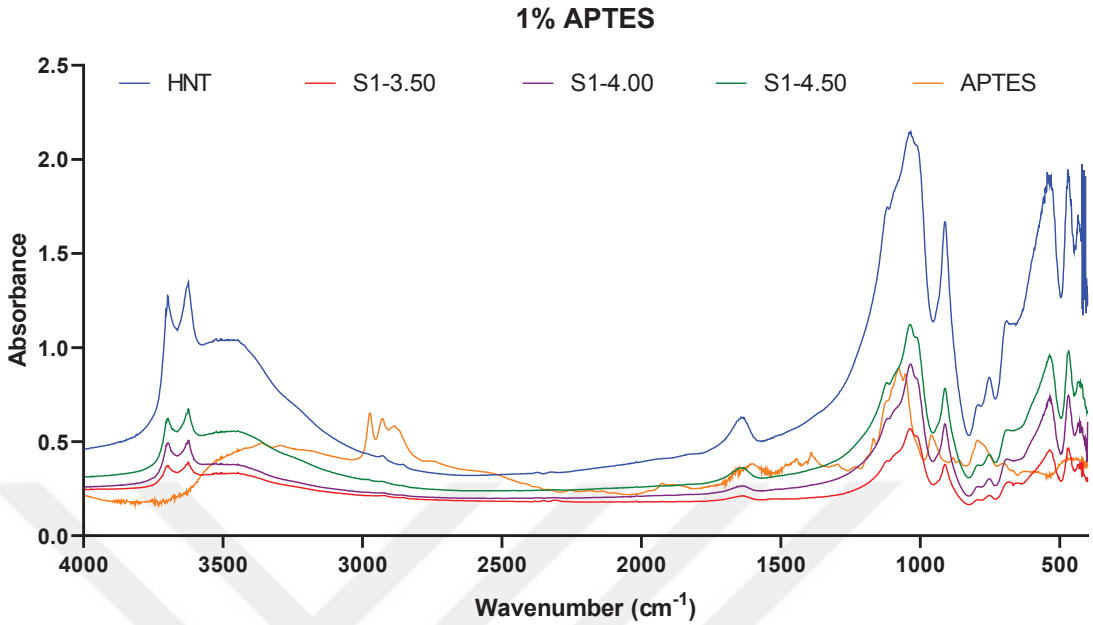

Figure 5.2. Effect of pH at 1% APTES Concentration

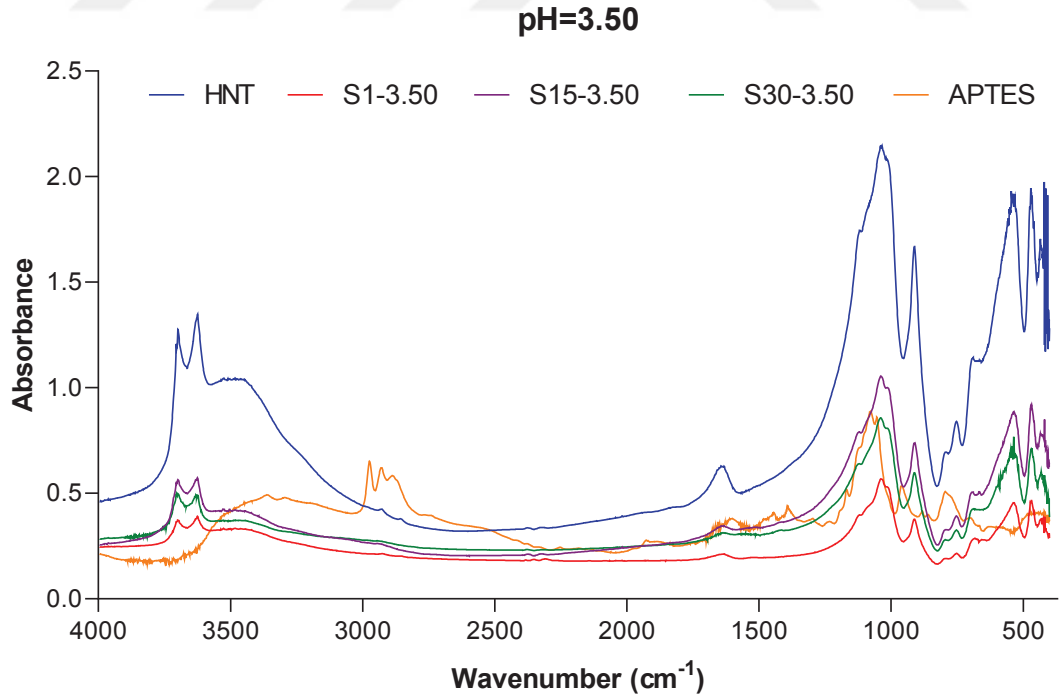

Figure 5.3. Effect of APTES Concentration at pH=3.50

According to Figure 5.3, the aforementioned peak intensities were decreased in a similar manner. S1-3.50 sample gave the best results according to FTIR results. Wavenumbers of characteristic peaks of HNT and APTES were shown in Table 5.2.

Table 5.2. Wavenumbers of Characteristic Peaks of HNT and APTES

	Si-O stretching	OH- stretching of hydroxyl groups	H_2O bending	NH_2 stretching	Al-OH deformation	CH_3
HNT	1022	3620-3693	1646	-	912	-
APTES	1076	-	1605	1556	-	2967
S1-3.50	**1031**	3631-3708	1649	-	**901**	-
S15-3.50	1021	3618-3692	1630	-	**903**	-
S30-3.50	1021	3637-3686	1611	-	**903**	-
S1-4.00	**1030**	3614-3689	1652	-	**903**	-
S15-4.00	1025	3612-3683	1653	**1536**	**905**	-
S30-4.00	1025	3625-3681	1641	**1564**	**904**	-
S1-4.50	1025	3629-3681	1614	-	**917**	-
S15-4.50	**1032**	3633-3707	1614	**1545**	**918**	-
S30-4.50	**1032**	3614-3706	1608	**1545**	**918**	-

According to Table 5.2, chemical shifts were detected for Si-O stretching and Al-OH deformation peaks, meaning that APTES was covalently bonded onto inner surface of HNT, edges of HNT tubular lumen and external surface defects of HNT (Peixoto et al, 2016; Yuan et al, 2012; Zeng et al., 2016; Zhang et al, 2013). NH_2 stretching peak of APTES was shifted by 20 cm^{-1} for S15-4.00 sample, 9 cm^{-1} for S15-4.50 and S30-4.50 samples and 8 cm^{-1} for S30-4 sample which confirms covalent bonding of APTES onto HNT.

5.1.1.3. TGA

% Mass loss and derivative of the % mass loss of the samples was represented in Figure 5.4 and Figure 5.5, respectively. First peak in Figure 5.5 is related to removal of adsorbed water from the samples. The interlayer spacing of HNTs change from 10 Å to 7 Å after the thermal water removal. The second peak asserts the dehydroxylation of Al-OH groups of HNTs(Yuan, Tan, et al., 2012). Table 5.3 was constructed based on Figure 5.5 and mass loss vs. temperature DATA.

According to Table 5.3, water removal peak of HNT was shifted due to the more hydrophobic surface of m-HNTs after silane modification. Structural dehydroxilation

between 450-600 (°C) was observed in the literature for organosilane modified HNTs (Barrientos-Ramírez et al. 2011). The organic group presence decreased thermal stability of HNTs and shifted the 2nd peak to lower temperatures.

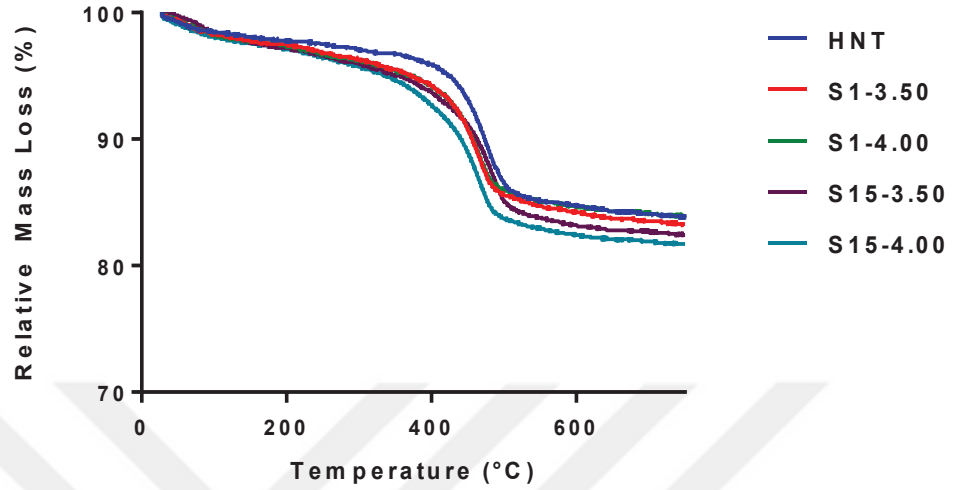

Figure 5.4. % Mass loss vs. Temperature

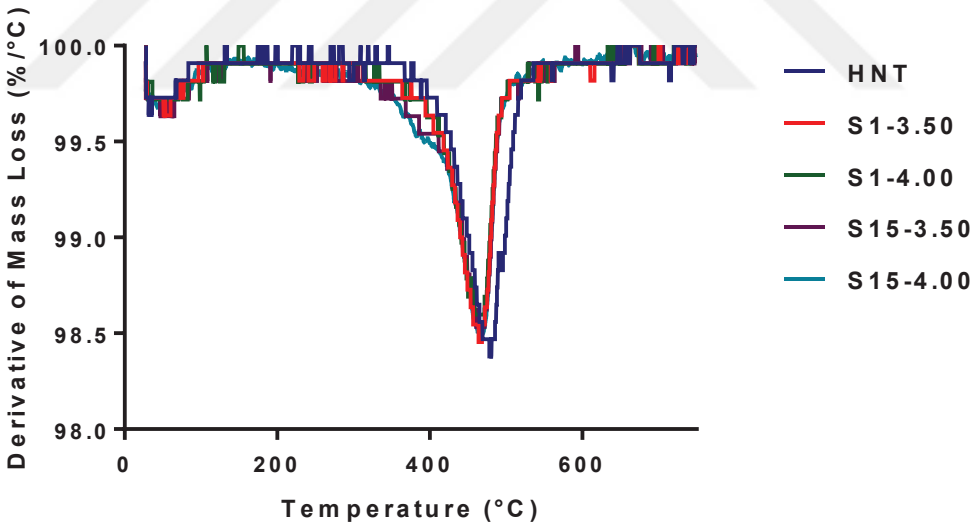

Figure 5.5. Derivative of Mass Loss vs. Temperature

Similarly, the temperature required for 5% mass loss was significantly lowered by 50-90 °C, proving the successful modification of HNTs. The temperature at 5% mass loss for m-HNTs modified with 15% APTES is lower than 1% modified APTES. However, the peak temperatures are similar for m-HNTs and the 1st peak temperature of S15-4.00 sample was lower than S1-4.00 sample. This means that HNTs modified with 1% APTES are more hydrophobic and more thermally stable than HNTs modified with

15% APTES. The better thermal stability of S1-3.50 and S1-4.00 samples may be addressed to more oligomerization of APTES and poor thermal stability of oligomer chains at higher concentrations of APTES.

Table 5.3. Peak Temperatures and Mass Losses of the Samples

	1st Peak (°C)	% Mass loss (1st peak)	2nd Peak (°C)	% Mass loss (2nd peak)	Temperature at 5% Mass Loss (°C)
HNT	71.8	1.4	500.4	11.3	443.1
S1-3.50	81.9	1.8	487.7	11.4	390.1
S1-4.00	82.0	2.3	492.9	10.9	391.2
S15-3.50	80.9	2.2	489.7	13.1	354.3
S15-4.00	72.6	1.9	490.7	12.8	362.4

In the literature higher APTES concentrations (10-100 (v/w)%) were used to modifiy surface of HNT. In our study, when overall properties of the HNT and m-HNT samples were considered, similar properties can be obtained with very less amount of APTES coupling agent (1% (v/w)). Instead of using higher APTES concentrations (15% APTES), 1% APTES was chosen as the optimum APTES concentration for further studies.

5.2. Effect of Sonication Time on the Mechanical Properties of PLA

Sonication is useful to evenly distribute nanoadditives in polymer matrices but ultrasonication of polymers using high power for a long time may result in chain cleavage and therefore, can significantly decrease mechanical and thermal properties. The effect of sonication on the mechanical properties of PLA was investigated by tensile testing with a load of 5 kgf. Sample names are given in Table 5.4.

Table 5.4. Sample Codes and Sonication Time of the Film Samples

Sample Code	Sonication Time (min)
PLA0	0
PLA15	15
PLA30	30

5.2.1. Mechanical Properties

Sonication of polymer solutions can cause chain cleavage of the polymer, therefore, the decrease in the molecular weight of the polymers may lower the mechanical properties of polymers significantly (Tayal and Khan 2000).

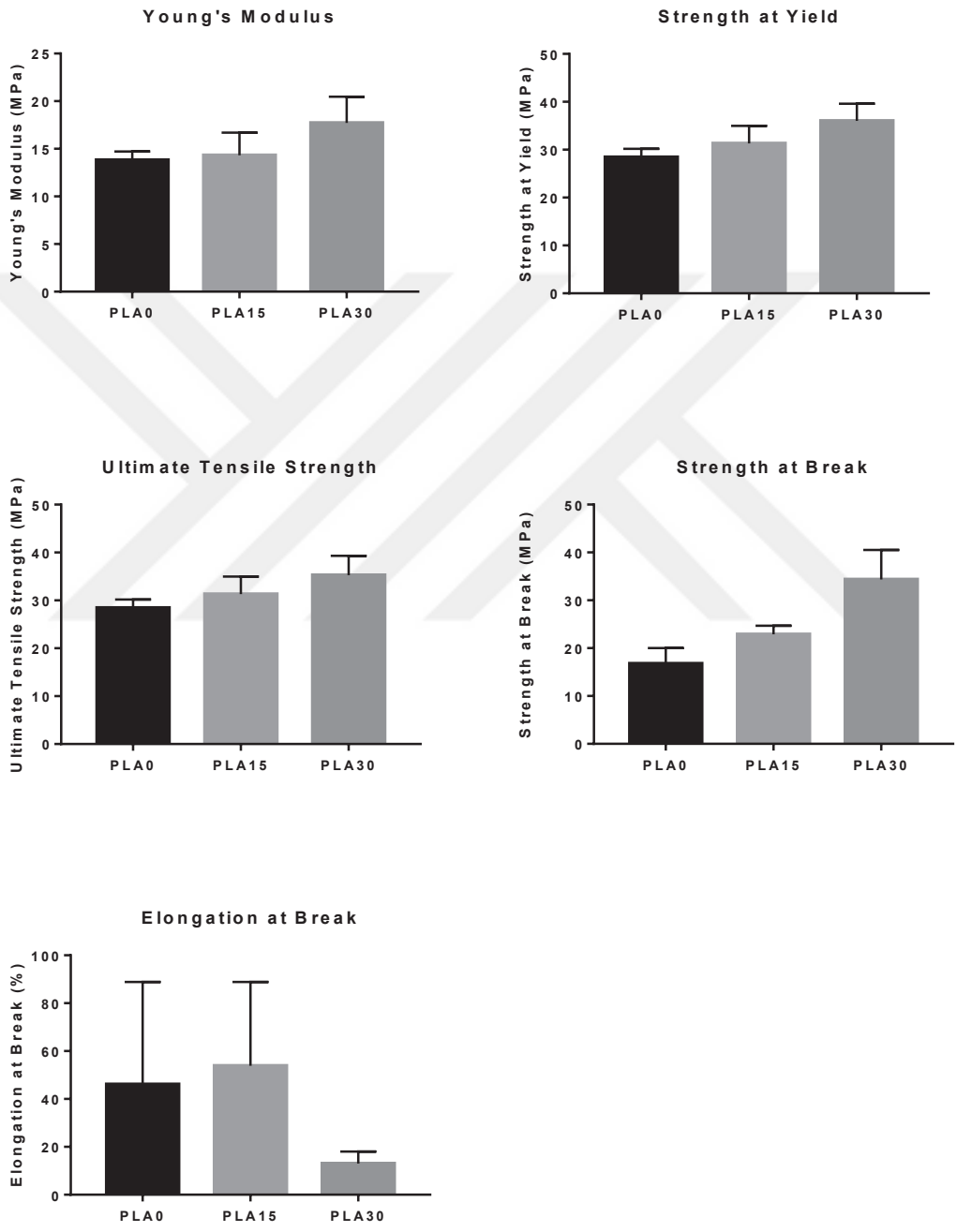

Figure 5.6. Effect of Sonication on the Mechanical Properties of the PLA Film

Effect of sonication time on the mechanical properties of PLA was studied to eliminate effect of degradation. Tensile properties of PLA with respect to sonication time is given by Figure 5.6.

According to tensile test results, Young's modulus, strength at yield, ultimate tensile strength and strength at break values of PLA were gradually increased with increasing sonication time. This is probably due to more even distribution of H-bonding between carbonyl groups of PLA and CH_3 and –H groups within PLA matrix. The decrease in the elongation at break of PLA when sonication time was increased from 15 to 30 min confirms shrunk structure of PLA due to more H-bonding in the polymer matrix.

5.3. Effects of Drying Temperature and Drying Time

Remaining solvents and water in PLA polymer matrix can cause plasticization of PLA. To avoid this, the effects of temperature and drying time were investigated. Sample properties are listed on Table 5.5.

Table 5.5. Sample Codes for Effect of Drying Temperature and Time

Sample Code	Drying Temperature (ºC)	Drying Time (day)
50-1	50	1
50-2	50	2
50-3	50	3
70-1	70	1
70-2	70	2
70-3	70	3

5.3.1. Mechanical Properties

The effects of temperature and drying time on the mechanical properties of the casted PLA films were investigated by tensile testing with a 50 kgf load. The results are given in Figures 5.7-5.13.

According to Figures 5.7 and 5.8, the tensile modulus and strength of all samples dried at 70 °C were higher than those of at 50 °C. 50-1 sample dried for 1 day possessed the poorest mechanical properties.

Strain at break and toughness of 50-1 sample were much higher than other samples indicating that PLA was highly plasticized. According to Figures 5.11 and 5.13, at 70 °C drying temperature, the samples of PLA dried for 1 day have higher strain at break and toughness.

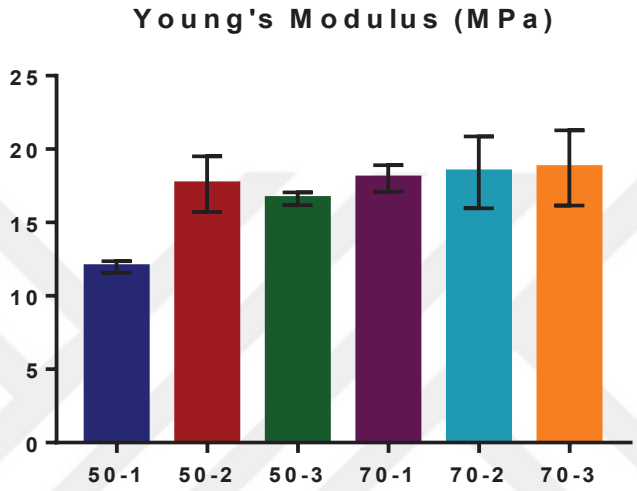

Figure 5.7. Young's Modulus

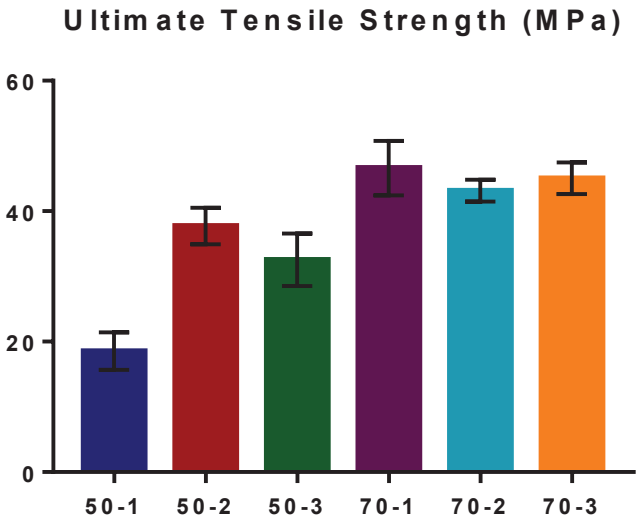

Figure 5.8. Ultimate Tensile Strength

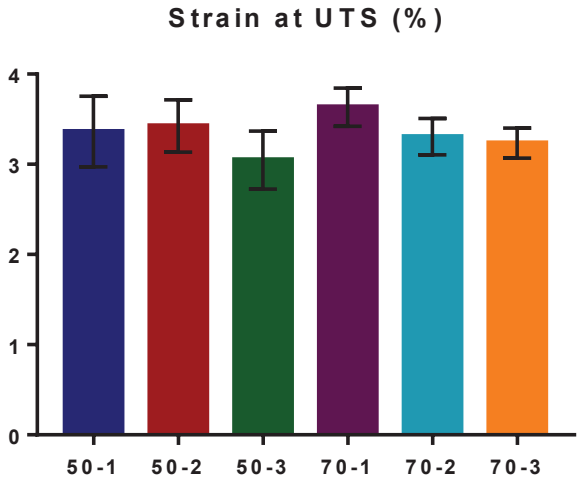

Figure 5.9. Strain at UTS

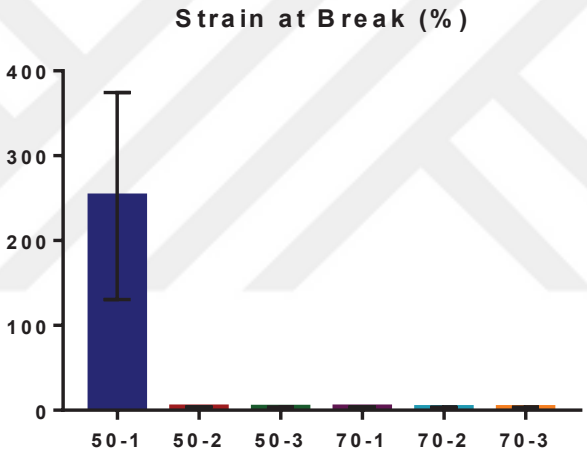

Figure 5.10. Strain at Break

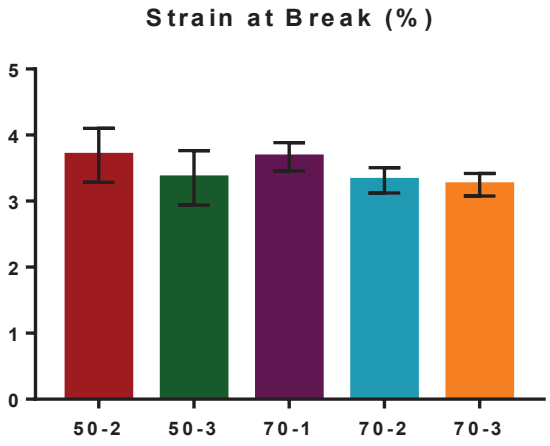

Figure 5.11. Strain at break (excluding sample 50-1)

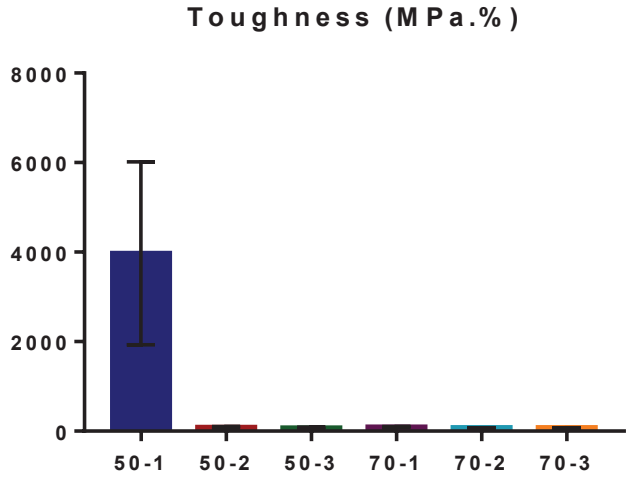

Figure 5.12. Toughness

Further increase in the drying time of PLA film caused decrease in both strain at break and toughness.

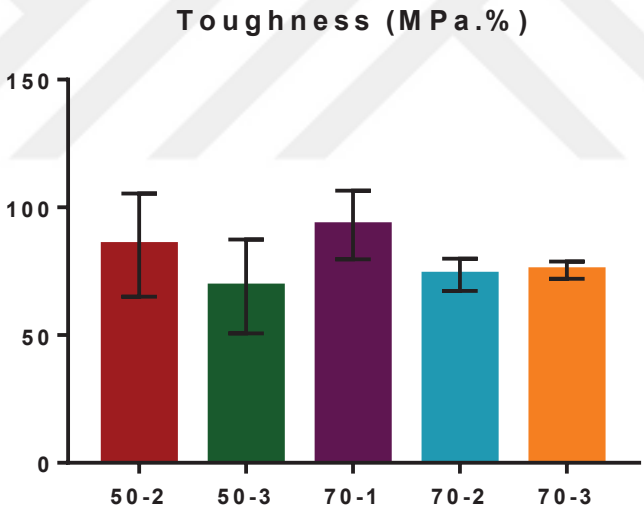

Figure 5.13. Toughness (excluding sample 50-1)

5.3.2. FTIR

For health concerns, food packaging materials should not release hazardous compounds onto the packed food. Since chloroform which is a gastrointestinal irritant was used as the solvent to dissolve PLA, there is a need to ensure that there was no remaining chloroform which may penetrate onto the food. Remaining solvent residue in PLA films was determined using FTIR analysis.

FTIR spectra of molten PLA and PLA film samples dried at 70 °C for 1 and 2 days between 800 and 600 cm^{-1} were shown in Figure 5.14. Chloroform possesses strong C-Cl stretching peaks at 774 and 680 cm^{-1} (Shen et al, 2019). According to FTIR spectra, both PLA films and melted PLA possessed peaks at 774 cm^{-1}. At 669 cm^{-1}, only 70-1 sample possessed a peak which is addressed to remaining chloroform within PLA chains. Therefore, based on the mechanical properties and FTIR results of PLA films, the films dried at 70 °C for 2 days was chosen as the optimum condition for the preparation of PLA films.

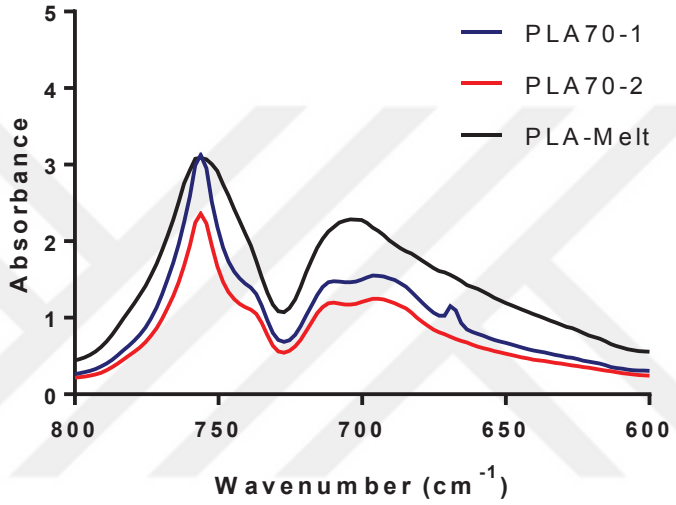

Figure 5.14. FTIR Spectra of Selected Film Samples and Molten PLA

5.4. Optimization of APTES and HNT Concentrations

Effect of APTES concentration on HNT surface modification was furtherly studied. Sample information is given in Table 5.6.

Table 5.6. Sample Names for Surface Modification of HNT

Sample Name	APTES Concentration (v/w)%
HNT	0
S1	1
S1.5	1.5
S2	2

HNT-PLA nanocomposites were prepared by solution casting with modified and unmodified HNT incorporation with nanoclay content up to 8 wt%. Information of film samples were listed on Table 5.7.

Table 5.7. Film Compositions

Sample Code	HNT/mHNT Content (% w/w)	APTES Content (% v/w)
PLA	0	-
U2	2	0
U4	4	0
U6	6	0
U8	8	0
M2S1	2	1
M4S1	4	1
M4S1.5	4	1.5
M4S2	4	2
M6S1	6	1
M8S1	8	1

5.4.1. Properties of Modified and Unmodified HNT

Morphological and chemical properties of modified and unmodified HNTs were investigated.

5.4.1.1. Morphological Properties

Tubular morphology of halloysite nanotubes before and after modification was investigated by SEM and N_2 adsorption-desorption analysis.

5.4.1.1.1. SEM

SEM images of the HNT and m-HNT samples are shown in Figure 5.15. According to Figure 5.15, HNTs are tubular structures with a nanoscale diameter and length. HNT dimensions change with silane modification. Smaller external tube diameters were observed with 1% APTES modification.

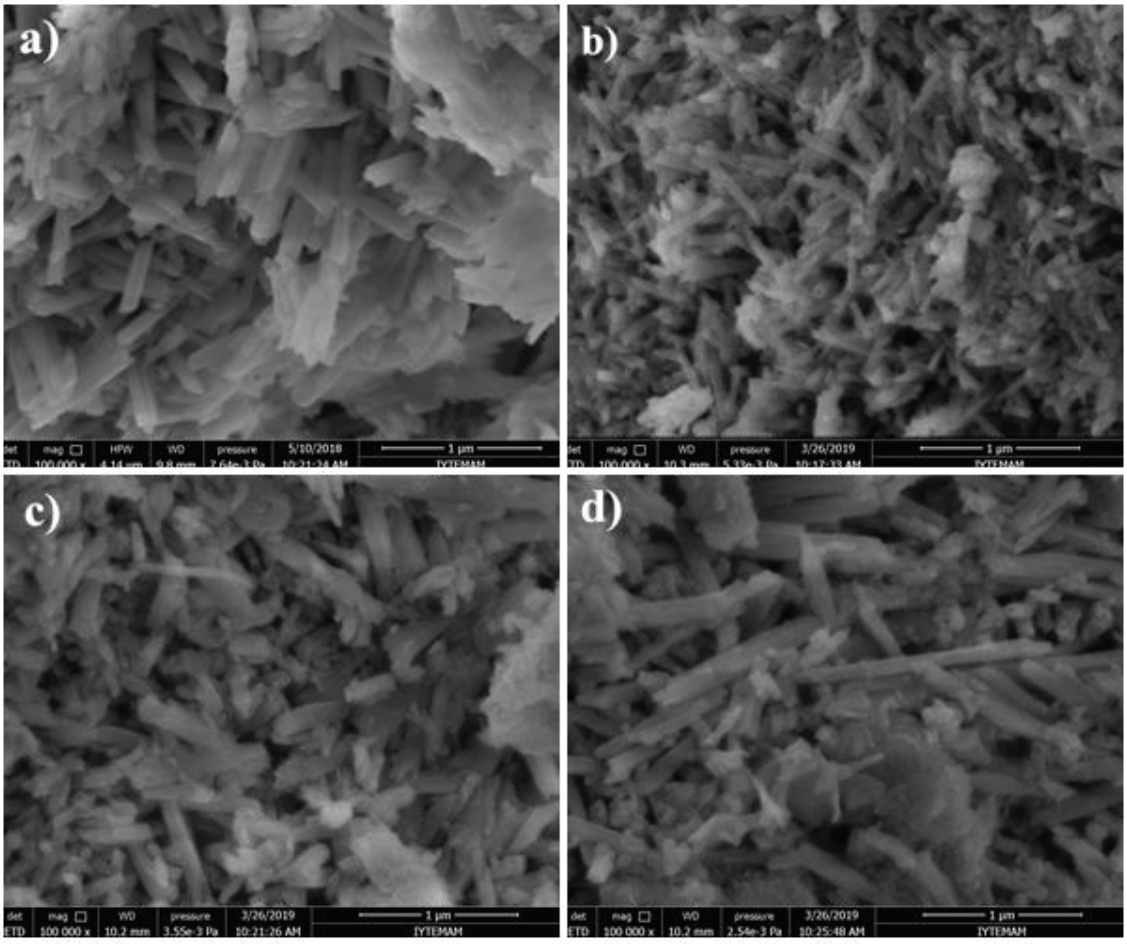

Figure 5.15. SEM Micrographs of the Samples (a) HNT, (b) S1, (c) S1.5, (d) S2

Since precise measurement of length of the nanotubes is not possible from the dense SEM micrographs, HNT and m-HNTs were dispersed in chloroform, sonicated for 30 min and diluted by hundredfold to examine diameter and length of the nanotubes correctly. SEM images of diluted HNT and m-HNT samples were shown in Figure 5.16. 1% and 2% APTES concentration resulted in agglomeration of m-HNTs even with sonication and dilution. APTES may formed a cross-linked structure at these concentrations. Unexpectedly, at 1.5% APTES concentration, conical shaped m-HNTs were obtained and each smaller diameter of the cones were close to another m-HNT.

Lengths of HNTs were within a range of 82-1000 nm with a diameter of 20-50 nm. Tubular structure of HNT was deteriorated with modification. The length of S1.5 samples were in a range between 130 and 1275 nm, and the largest diameter ranges are changing between 148 to 323 nm.

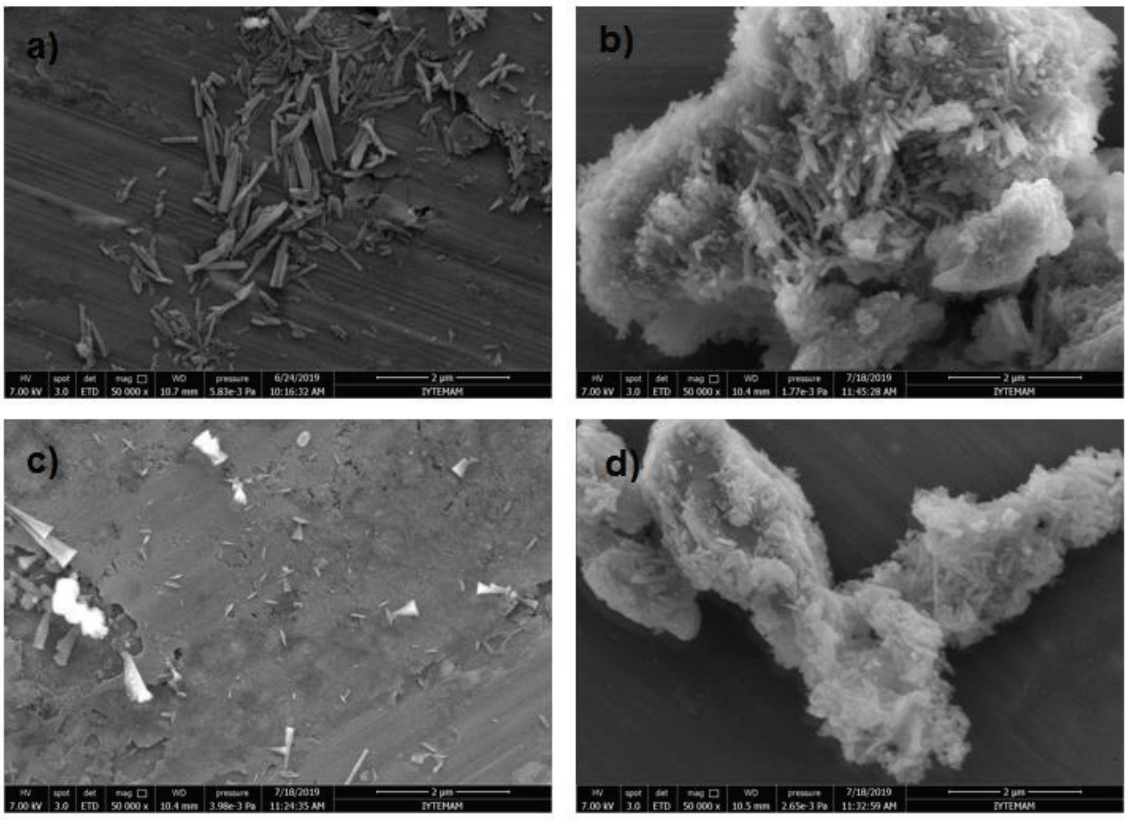

Figure 5.16. SEM Images of 100x Diluted HNT and m-HNT Samples (a) HNT, (b) S1, (c) S1.5, (d) S2

5.4.1.1.2. N_2 Adsorption Desorption Analysis

Figure 5.17 represents the nitrogen adsorption-desorption isotherms vs. relative pressure. HNT and m-HNTs have shown Type IV IUPAC isotherms and H4 Type hysteresis loops. Many mesoporous adsorbents show Type IV physisorption isotherms. H4 type hysteresis loops is associated with narrow, slit-like pores. Monolayer formation was completed around $p/p_0 = 0.05$, then multilayer adsorption of N_2 molecules occurs. Typically, halloysite has an inner dimeter around 10-15 nm and outer diameter of 50-60 nm with aluminosilicate layers (separated by 0.7-1.0 nm interlayer spacing) amongst them (Glotov et al. 2018). Halloysite has mesoporous (2-50 nm) structure and its tubular interlayer space is in microporous scale (<2nm) (Sing 1985).

Surface area and micropore volume of adsorption-desorption isotherms were given in Table 5.8. After $p/p_0 = 0.8$, relative adsorbed volume was increased and deviated from Type IV IUPAC isotherm which indicates that complete pore filling could not be achieved probably due to the specific interactions between polar groups and the hydroxylated silicate surfaces. Consequently, relative pressure was not achieved to 1.

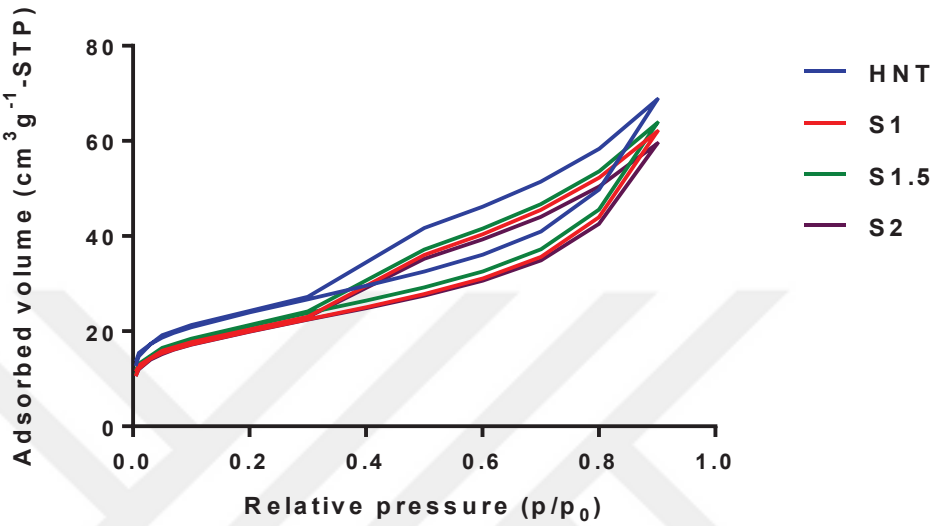

Figure 5.17. N_2 Adsorption-Desorption Isotherms of the Samples

Table 5.8. Surface Area and Micropore Volume of the HNT and m-HNT Samples

	BET Surface Area (m^2/g)	Langmuir Surface Area (m^2/g)	t-Plot Micropore Volume (cm^3/g)
HNT	82.46	116.40	0.0066
S1	69.57	97.59	0.0041
S1.5	73.93	104.35	0.0028
S2	69.37	97.68	0.0038

According to Table 5.8, BET surface area, Langmuir surface area and micropore volume of HNT were decreased after modification with APTES. Krishnaiah et al. reported a significant decrease in BET surface area from 61.74 to 18.38 m^2/g (70.2% decrease) and Langmuir surface area from 84.45 to 25.43 m^2/g (69.9% decrease) with HNTs modified with 24% (w/w) APTES and with a silanization pH of 4.5-5.5. Our samples have shown a decrease in BET surface area by 15.6% and a decrease in Langmuir

surface area by 16.2% using only 1% (v/w) (the density of APTES is close to 1 g/ml) APTES for S1 sample even with a silanization pH of 3.50. Low pH may have increased the pore volume due to the disintegration of Al-OH surface by acidic lumen etching. The decrease in BET and Langmuir surface areas, micropore volume and relative pressure difference at constant adsorbed volume may be addressed to the APTES linkage into HNT lumen and edges of HNT, hindering the N_2 passage through HNTs.

BET and Langmuir surface areas are not equal to each other. It should be noted that various assumptions were done and different empirical models were used to determine BET and Langmuir surface areas (Sing 1985).

5.4.1.2. Chemical Properties

Chemical properties of HNT and m-HNTs were determined by XRD, FTIR and XPS analysis.

5.4.1.2.1. XRD

The XRD patterns of HNT and m-HNTs were represented in Figure 5.18. The intensities of the peaks at 2Θ = 12, 20, 24.5, 26.8, 55 and 62.6° were significantly decreased. This means that the arrangement of HNT molecules were changed after APTES modification and crystallinity of HNT was decreased. The distinct peak of S1 sample at 2Θ = 36° may be attributed to silane modification.

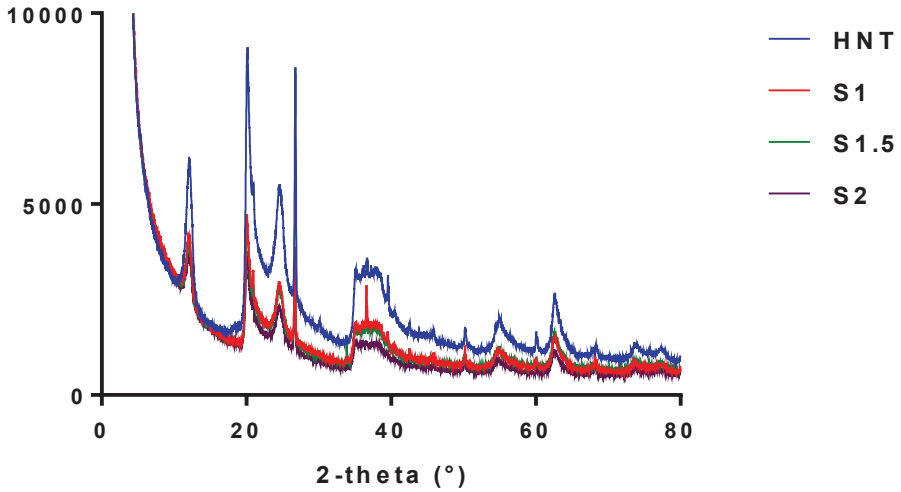

Figure 5.18. XRD Patterns of HNT and m-HNTs

XRD results were shown in Table 5.9. According to Table 5.9, the characteristic peak of HNT at 12.1° was shifted only by 0.1-0.2°. The interlayer spacing of aluminosilicate layers of HNT is about 7 Å which is the dehydrated form of HNT. The basal spacing was slightly decreased by silane modification for 1 wt% and 2 wt % APTES modified samples due to the water repellency.

Table 5.9. XRD Results

	HNT	S1	S1.5	S2
2Θ	12.1	12.2	12.0	12.3
d-spacing (Å)	7.3	7.2	7.4	7.2

5.4.1.2.1. FTIR

FTIR spectra of the nanoclay samples and closer view of the spectra where APTES modified HNTs depict different peaks than HNT were represented in Figure 5.19.

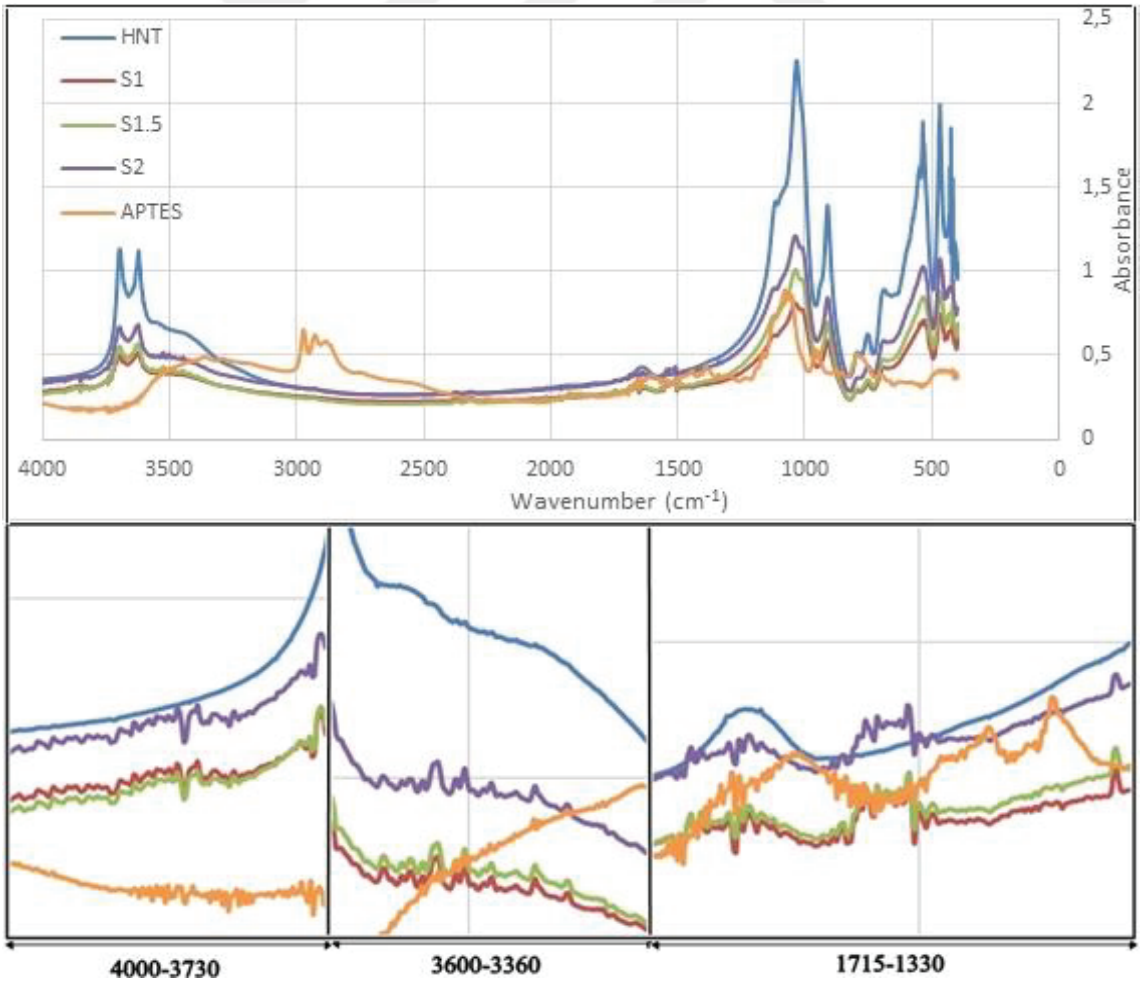

Figure 5.19. FTIR Spectra of HNT, m-HNTs and APTES

Characteristic peaks of HNT and m-HNTs were given in Table 5.10. According to Table 5.10 C-H_2 deformation and N-H_2 deformation peaks belonging to APTES were observed in the FTIR spectra of m-HNTs. Chemical shifting from 1556 to 1543 of N-H_2 deformation peak of APTES was observed for m-HNTs which means that APTES was covalently bonded onto HNTs for all m-HNT samples. Peak intensities of the important peaks were listed on Table 5.11.

Table 5.10. Wavenumbers of Important Peaks Obtained from FTIR Spectra

	Deformation of Si-O-Si	Deformation of Al-O-Si	Perpen-dicular Si-O stretching	Perpen-dicular Si-O stretching	Perpen-dicular Si-O stretching	Si-O Symmet-ric stretching
HNT	469	536	691	755	1112	791
S1	467	**529**	683	746	1117	793
S1.5	467	**532**	683	746	1113	791
S2	467	**532**	685	746	1117	793
APTES	-	-	-	-	-	-

Table 5.10. Wavenumbers of Important Peaks Obtained from FTIR Spectra (Cont'd)

	O-H deformation of inner OH groups	Si-O stretching	Deformation of C-H_2	Deformation of N-H_2	O-H deformation of water
HNT	912	1035	-	-	1636
S1	910	1032	1493	**1543**	1639
S1.5	912	1042	1485	**1543**	1640
S2	910	1034	1485	**1543**	1638
APTES	-	-	1491	1556	-
	C-H_2 stretching	C-H_2 stretching	OH-stretching of inner OH groups	OH-stretching of inner surface OH groups	C-O stretching
HNT	-	-	3621	3694	-
S1	-	-	3622	3694	-
S1.5	-	-	3622	3694	-
S2	-	-	3622	3694	-
APTES	2864	2931	-	-	1235

Table 5.11. Peak Intensities of the FTIR Spectra of Nanotubes

	Deformation of Si-O-Si	Deformation of Al-O-Si	Perpendicular Si-O stretching	Perpendicular Si-O stretching	Perpendicular Si-O stretching	Si-O Symmetric stretching
HNT	0.7837	1.0022	0.3758	0.1105	1.0269	0.1467
S1	0.2631	0.2295	0.1286	0.0876	0.3327	0.0499
S1.5	0.3387	0.3072	0.1571	0.1088	0.4426	0.0608
S2	0.4104	0.3669	0.2044	0.1400	0.5335	0.0793
APTES	-	-	-	-	-	-
	O-H Deformation of inner OH groups	**O-H Deformation of inner surface OH groups**	**Si-O stretching**	**Deformation of C-H_2**	**Deformation of N-H_2**	**O-H deformation of water**
HNT	0.5934	0.7743	1.9812	-	-	0.0508
S1	0.1572	0.2073	0.5766	0.0019	0.0562	0.0322
S1.5	0.2127	0.2836	0.7943	0.0010	0.0512	0.0444
S2	0.2594	0.3306	0.9425	0.0051	0.0497	0.0301
APTES	-	-	-	0.0059	0.0674	-
	C-H_2 stretching	**C-H_2 stretching**	**O-H stretching of water**	**OH- stretching of inner OH groups**	**OH- stretching of inner surface OH groups**	**C-O stretching**
HNT	-	-	0.3702	0.4265	0.7743	-
S1	-	-	-	0.1238	0.2073	-
S1.5	-	-	-	0.1604	0.2836	-
S2	-	-	-	0.1925	0.3306	-
APTES	0.1548	0.1065	-	-	-	0.0178

According to Tables 5.10, 5.11 and Figure 5.17, intensity of characteristic HNT peaks were decreased with APTES modification. Decrease in the peak intensities of inner surface OH- stretching and OH- stretching of inner OH groups indicate coating of HNT with APTES from the inner surface and inner OH groups. Peaks at 1636, 3621 and 3694 cm^{-1} were decreased significantly with modification. The surface of HNT became more hydrophobic with modification and water peaks decreased the most with 1% APTES modification. Characteristic peaks of APTES were observed at 1490 and 1543 cm^{-1} in the spectra of m-HNTs. The biggest peak intensity at 1543 cm^{-1} belongs to S1 sample which proves the presence of NH_2. Eventually, FTIR results revealed that the best APTES concentration was 1% among all the surface modified HNTs.

5.4.1.2.3. XPS

XPS spectra of unmodified and modified halloysite nanotubes were shown in Figure 5.20.

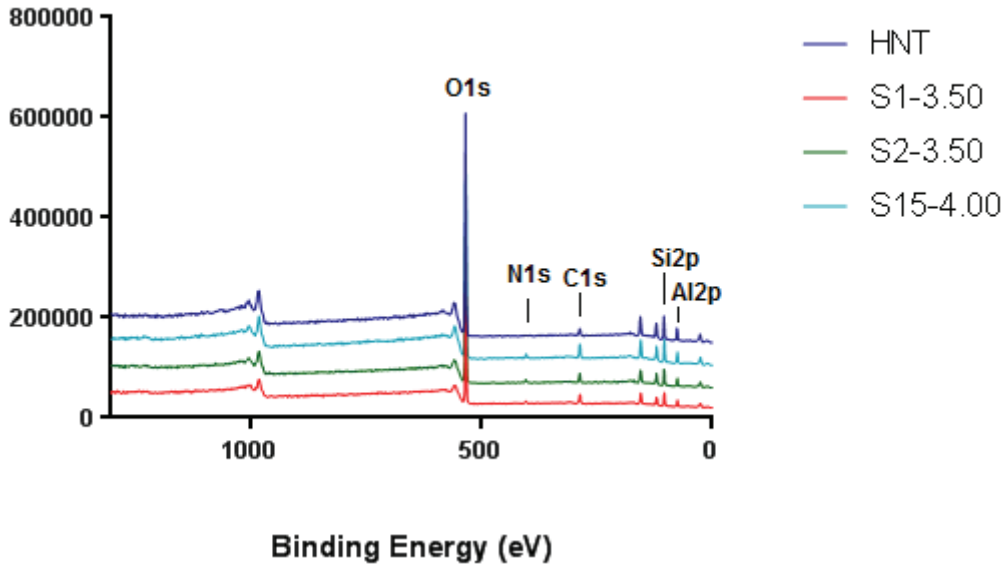

Figure 5.20. XPS Spectra of HNT and m-HNTs

According to XPS spectra of HNT and m-HNTs, N1s peak was not observed in HNT spectrum but all modified samples contained N element. Presence of N1s peak and increased intensity of C peak of HNT proves covalent bonding of APTES with HNT. CO_2 adsorbed in HNTs and C band lead to C peak formation in the XPS spectrum of HNT. Chemical compositions of HNT and m-HNT samples were determined via XPS analysis (Table 5.12).

According to Table 5.12, acetic acid caused lumen etching of HNTs due to the decreasing Al content. The increase in the C percentage, N presence and the decrease of Al/Si ratio of HNTs after modification with APTES, gives information about the covalent bonding of APTES onto HNTs. Al/Si ratio was furtherly decreased with lumen etching with acetic acid. The clearest information can be obtained from N percentage since it does not have signal for HNTs. According to this peak, best silanization percentage was 2% APTES modified samples. The lower concentrations gave better bonding results. 1% and 2% APTES provided better modification than 15% APTES. O1s spectra of HNT and m-HNTs were given in Figure 5.21.

Table 5.12. Elemental Compositions of HNT and m-HNTs

Atomic (%)	Al	Si	O	C	N	Al/Si
HNT	14.2	17.4	60.0	8.5	0.0	0.82
S1-3.50	10.5	16.6	55.2	13.9	3.8	0.64
S2-3.50	10.2	16.9	52.4	16.1	4.4	0.61
S15-4.00	11.0	16.1	53.1	16.6	3.0	0.68

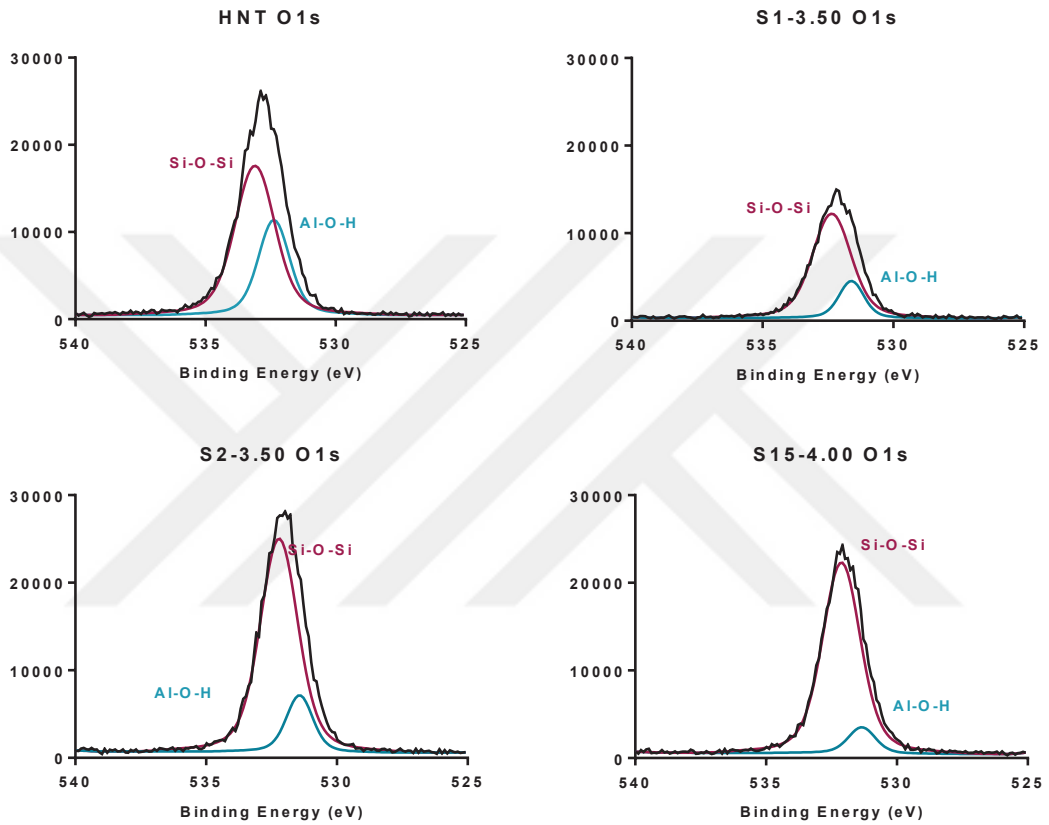

Figure 5.21. O1s Scan of HNT and m-HNTs

According to O1s spectra of the HNT and m-HNT samples, HNT had two main oxygen peaks. The peak at 532.7 eV corresponds to Al-O-H groups of HNT. The peak at 533.0 eV corresponds to Si-O-Si groups on the external surface of HNTs. C1s and N1s spectra of modified HNTs were represented in Figure 5.22.

According to Figure 5.22, C-C, C-N, Si-C bonds were detected in C1s spectra of modified HNTs showing that APTES was linked onto HNTs covalently. Nitrogen peaks are additional proofs. Peak intensity of N1s peak of S2-3.50 sample was higher than other modified HNT samples. Binding energies of the peaks in Figures 5.20-5.22 were given in Table 5.13.

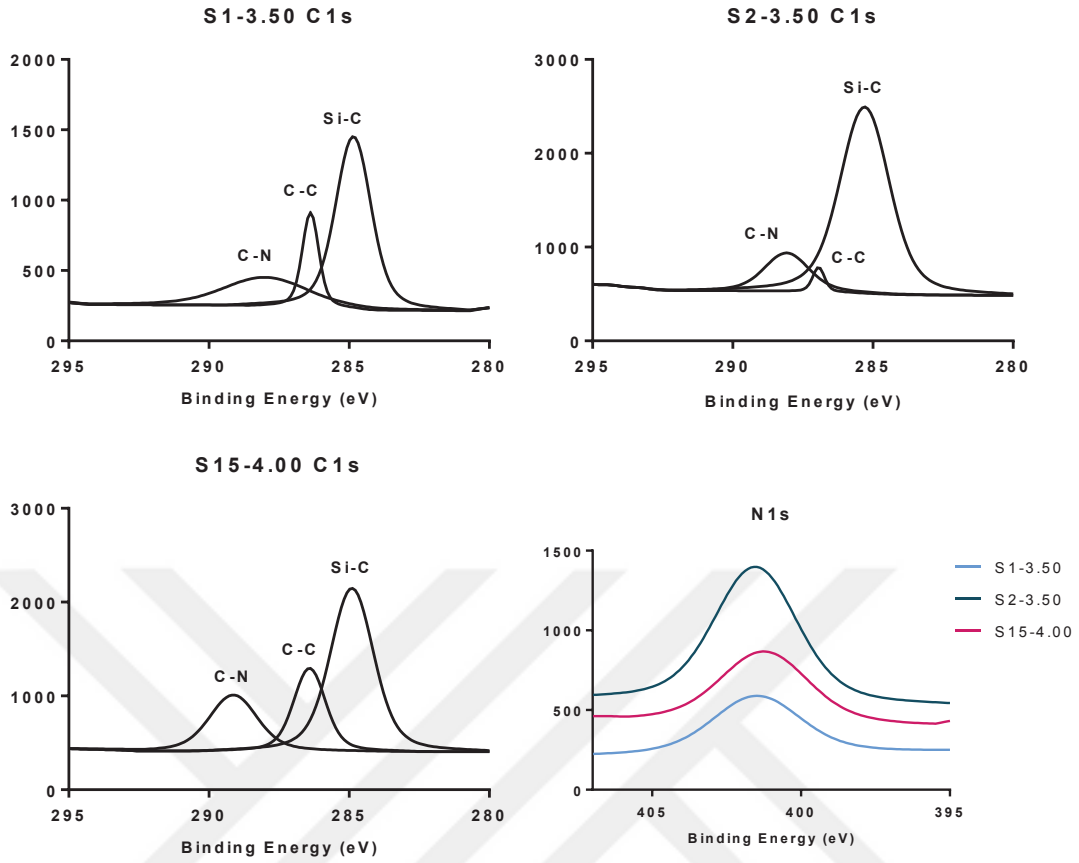

Figure 5.22. C1s and N1s Scans of m-HNTs

According to Table 5.13, binding energy of Al2p3 peak of HNT was shifted from 75.2 to 74.5-74.4 eV for modified HNTs, representing Al-OH surface etching. Si2p3 peak was also shifted from 103.4 to 102.8-102.5 eV for modified HNTs. C1s peaks (Si-C, C-C, C-N) were shifted by 1-1.4 eV, 1.3-1.7 eV, 0.6-1.4 eV respectively. O1s peaks (Al-OH, Si-O-Si) were shifted from 532.7 to 531.2-531.6 eV and from 533.0 to 532.1-532.4 eV respectively. All the mentioned peak shifts indicate APTES covalent bonding onto HNTs.

According to XPS results, the lower concentrations of APTES (1-2%) gave better silanization efficiency than the high concentration of APTES (15%). To eliminate the effect of pH, S15-3.50 sample and HNT exposed to silanization solution without adding APTES may be analyzed furtherly. In conclusion according to XPS results, S2-3.50 sample gave the best modification result (Sun et al. 2015, He et al. 2015, (Hemmatpour, Haddadi-asl, & Roghani-mamaqani, 2015).

Table 5.13. Peak Binding Energies of HNT and m-HNTs

BE (eV)	HNT	S1-3.50	S2-3.50	S15-4.00
Al2p3	75.2	74.5	74.5	74.4
Si2p3	103.4	102.8	102.7	102.5
C1s	283.8	285.2	285.2	284.8
C1s	285.1	286.8	286.5	286.4
C1s	287.5	288.3	288.1	288.9
N1s	-	401.7	401.5	401.4
O1s	532.7	531.6	531.5	531.2
O1s	533.0	532.4	532.3	532.1

5.4.1.3. Thermal Properties

Thermal properties of halloysite nanotubes and APTES modified halloysite nanotubes were investigated by TGA.

5.4.1.3.1. TGA

There are two major peaks at the relative mass loss vs. temperature and derivative of mass loss vs. temperature graphs of HNT and m-HNTs (Figures 5.23 & 5.24), indicating water loss and dehydroxylation from Al-OH surface (Krishnaiah et al. 2017).

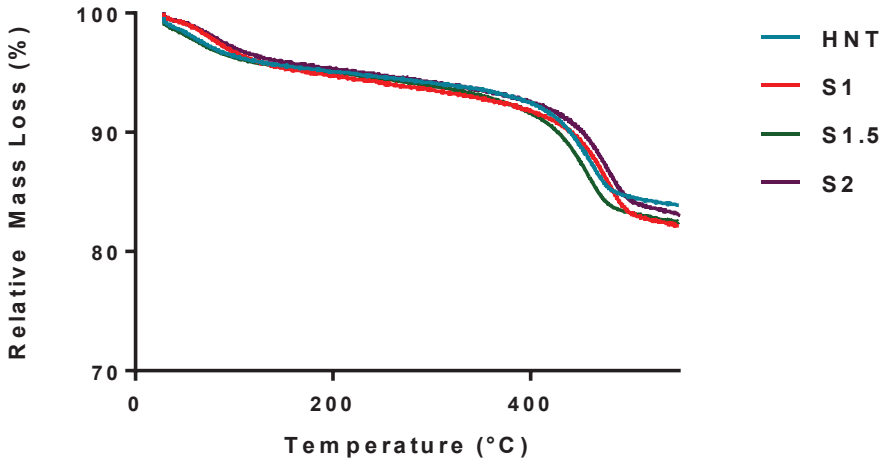

Figure 5.23. Relative Mass Loss of HNT and m-HNTs vs. Temperature

Utilizing from relative mass loss and mass loss vs. temperature data, important mass loss peak temperatures and % mass losses at the major peaks were given in Table 5.14. According to Table 5.14, no significant shifts were observed for the thermal removal of water (1st peak). In modified HNTs, enhanced water repellency due to the hydrophobic

groups of APTES may lead to less adsorbed water, hence lower % removal of water from nanoclay samples.

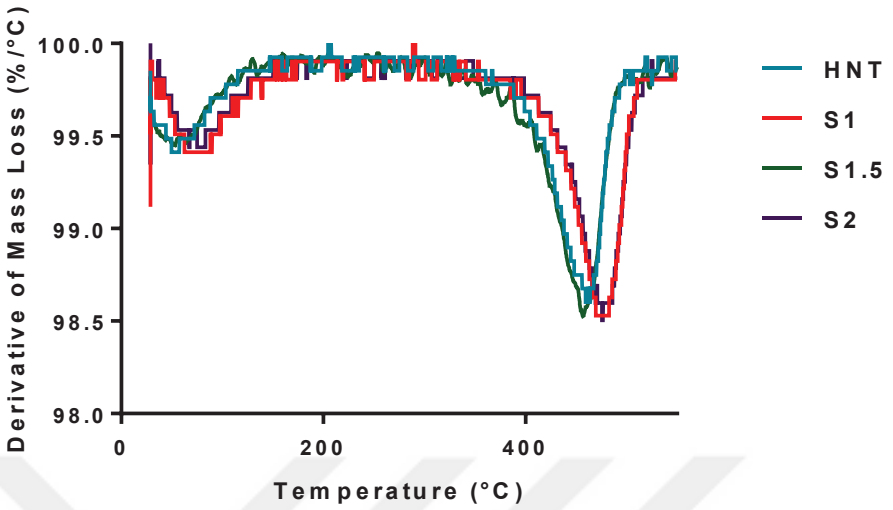

Figure 5.24. Derivative of Mass Loss vs. Temperature

2nd peak temperature which is addressed to dehydroxylation of Al-OH surface was shifted with APTES modification, mostly for S1 sample by 35.4 °C probably due to the organic group presence of APTES. The % mass loss at the 2nd peak was higher for modified HNT samples probably due to the decomposition of APTES groups. Thermal instability of APTES may lead to reduced thermal resistance of m-HNTs. The temperature required for 5% mass loss was decreased the most for S1 sample and the overall mass loss at maximum temperature was the highest for S1 sample, probably due to more effective silane modification than other m-HNTs.

Table 5.14. TGA Results of Modified and Unmodified Nanotubes

	1st Peak (°C)	% Mass loss (1st peak)	2nd Peak (°C)	% Mass loss (2nd peak)	T at 5% Mass Loss (°C)	Remaining % mass at T_{max}
HNT	78.0	4.1	482.7	9.6	227.9	83.7
S1	77.1	4.0	447.3	10.7	174.4	81.6
S1.5	75.4	3.9	476.3	10.2	221.9	82.1
S2	79.0	3.6	475.4	10.0	226.8	82.5

5.4.2. Properties of PLA-HNT Nanocomposite Films

Based on all characterization techniques, APTES concentration was optimized at 1 (v/w) %. Unmodified and modified HNT containing films were prepared. Chemical, mechanical and transport properties and surface wettability of HNT/PLA nanocomposite films were investigated.

5.4.2.1. Chemical Properties

Chemical Properties of PLA, HNT/PLA and m-HNT/PLA thin films were investigated by FTIR and XRD analysis.

5.4.2.1.1. FTIR

FTIR spectra of unmodified and modified HNT/PLA nanocomposites were given in Figures 5.25 and 5.26, respectively. Wavenumbers of important FTIR peaks in Figure 5.25 and 5.26 were listed on Table 5.15.

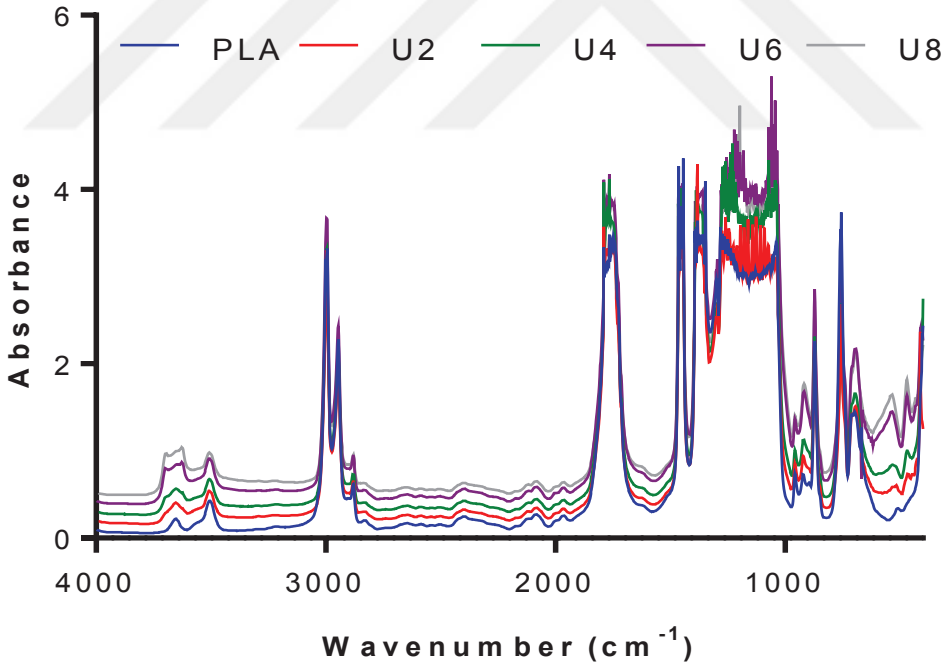

Figure 5.25. FTIR Spectra of Unmodified HNT/PLA Nanocomposite Films

The HNT/PLA nanocomposite films have shown characteristic PLA peaks given in Table 2.2. According to Figures 5.25. and 5.26, peak intensities at 468 (Si-O-Si deformation), 536 (Al-O-Si deformation), 3625 (-OH stretching of inner OH groups),

3700 (-OH stretching of inner surface OH groups) cm^{-1} belonging to HNT and m-HNTs were increased with increasing HNT/m-HNT concentrations as expected.

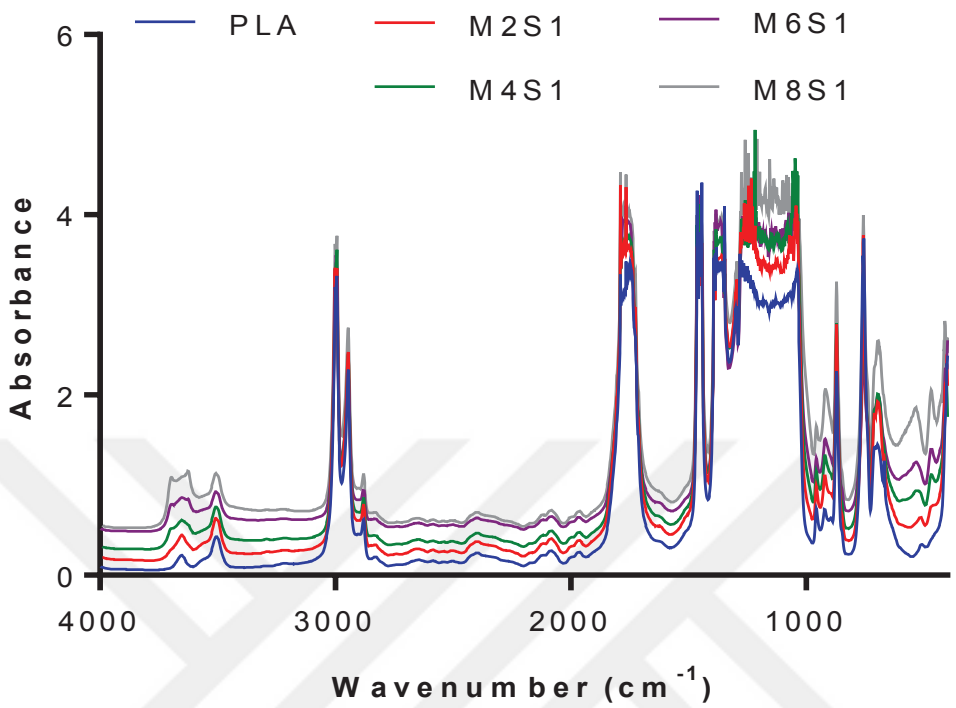

Figure 5.26. FTIR Spectra of Modified HNT/PLA Nanocomposite Films

Table 5.15. Wavenumbers of FTIR Peaks

Wavenumber (cm^{-1})	Deformation of Si-O-Si	Deformation of Al-O-Si	-C-C- Stretching		$-CH_3$ stretching	-OH bending
PLA	-	-	872	924	955	1038
U2	465	536	872	920	957	1041
M2S1	469	-	872	920	957	1044
U4	473	536	872	920	959	1044
M4S1	471	529	872	920	957	1047
U6	469	540	872	920	957	1044
M6S1	469	534	872	920	957	1044
U8	471	538	872	916	957	1051
M8S1	469	538	872	916	957	1051

Table 5.15. Wavenumbers of FTIR Peaks (Cont'd)

Wavenumber (cm^{-1})	-C-O- Stretching			-C=O bending	-CH_3 deformation		-CH_3 bending
PLA	1094	1128	1182	1231	1346	1381	1462
U2	1090	1126	1178	1226	1346	1381	1462
M2S1	1094	1128	1182	1233	1344	1383	1464
U4	1098	1128	1182	1229	1350	1387	1464
M4S1	1078	1121	1184	1217	1344	1383	1464
U6	1082	1126	1180	1221	1346	1383	1462
M6S1	1086	1128	1186	1217	1346	1383	1460
U8	1070	1125	1197	1221	1350	1383	1460
M8S1	1082	1130	1197	1217	1346	1383	1460

Table 5.15. Wavenumbers of FTIR Peaks (Cont'd)

Wavenumber (cm^{-1})	-OC=O Carbonyl Stretching	-CH- Stretching			OH- stretching of inner OH groups	OH- stretching of inner surface OH groups
PLA	1749	2881	2945	2996	-	-
U2	1749	2884	2945	2996	-	-
M2S1	1765	2884	2947	2994	-	-
U4	1765	2884	2945	2997	3626	3700
M4S1	1765	2880	2945	2994	3624	3702
U6	1765	2882	2947	2997	3628	3698
M6S1	1765	2880	2945	2997	3626	3698
U8	1765	2880	2945	2997	3628	3696
M8S1	1765	2880	2945	2994	3624	3698

According to Table 5.15, –OH stretching of inner OH groups and –OH stretching of inner surface OH groups of HNT and m-HNTs were shifted from 3621-3622 to 3624-3628 cm^{-1} and from 3694 to 3696-3702 cm^{-1} due to H-bond formation with PLA chains (Table 5.13). –C=O bending peak of PLA at 1231 cm^{-1} was shifted by 4-12 cm^{-1} with modification. –OC=O carbonyl stretching peak of PLA was shifted from 1749 to 1765 as an identifier of more H-bonding, which also shows the modification effect for M2S1

nanocomposite film (Garlotta 2002, Auras et al. 2014, Chen et al. 2017, Krishnaiah et al. 2017).

5.4.2.1.2. XRD

XRD patterns of PLA, HNT/PLA and m-HNT PLA films were shown in Figure 5.27. According to Figure 5.27, PLA had sharp peak at 2Θ = 16.7°, which means that it had a semi-crystalline structure. Peak positions and crystallinity percentages of the film samples were given in Table 5.16.

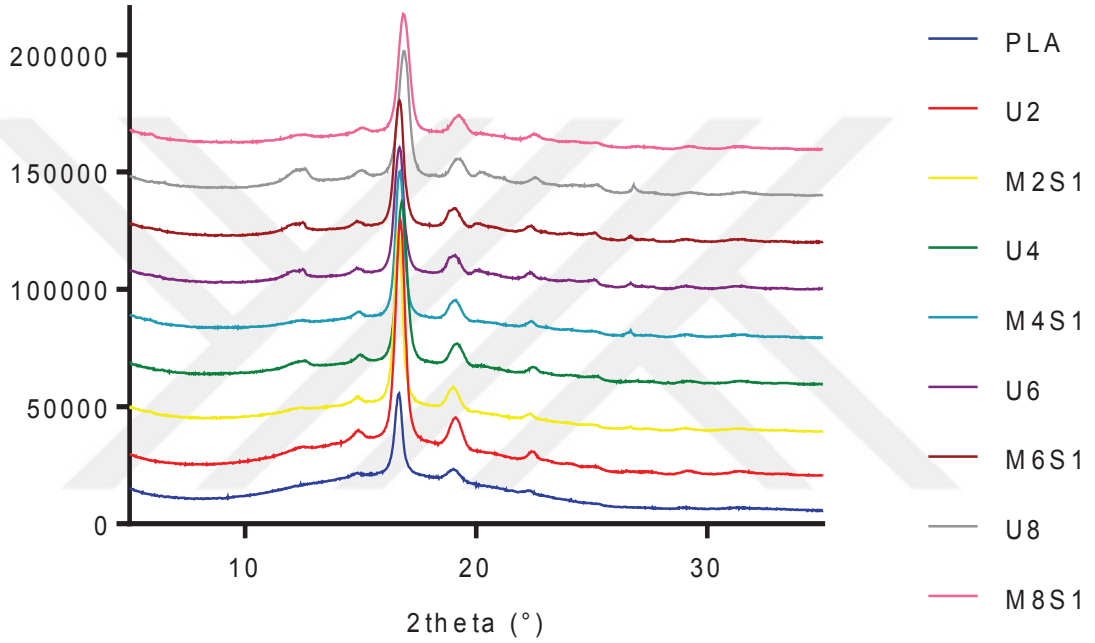

Figure 5.27. XRD Patterns of the Nanocomposite Films

According to Table 5.16, characteristic XRD peak of PLA at 2Θ = 16.7° was shifted with APTES modification by 0.2° for 2 and 6 wt% loaded films. Crystallinity of PLA was increased by 5.3% with 2 wt% of HNT addition. Crystallinity was furtherly increased by 11.6% with 2 wt% APTES modified HNT incorporation. However, at higher m-HNT concentrations, crystallinity was decreased due to poor dispersion and agglomerations of m-HNTs (Gorrasi et al. 2014, De Silva et al. 2016). An increase in the crystallinity of the modified HNT incorporated film was also obtained from the DSC analysis, however, the crystallinity values are much lower.

Table 5.16. Peak Positions and % Crystallinity of the Films

	Peak Position	% Crystallinity
PLA	16.7	55.9
U2	16.8	61.2
M2S1	16.6	72.8
U4	16.8	67.8
M4S1	16.8	60.9
U6	16.8	67.8
M6S1	17.0	54.3
U8	16.9	58.5
M8S1	16.9	60.7

5.4.2.2. Mechanical Properties

Mechanical properties of PLA/HNT nanocomposite films were represented in Figures 5.28-5.34. According to Figure 5.28, Young's modulus of the unmodified HNTs was increased with HNT addition up to 6 (w/w) %, then it was decreased probably due to HNT agglomerations within PLA matrix. 2% HNT addition increased Young's modulus of PLA by 4.7% while m-HNT addition provided 17.0% increase in the modulus. Higher m-HNT loadings did not influence Young's modulus significantly.

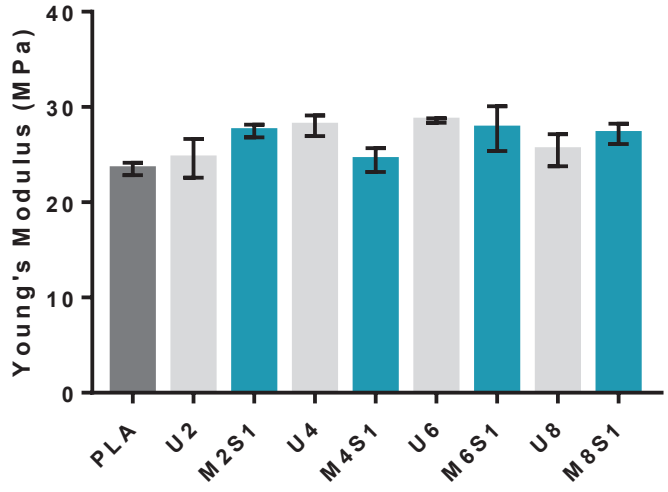

Figure 5.28. Young's Modulus of PLA/HNT Films at Various HNT Loadings

Krishnaiah et al. prepared 24% (w/w) APTES modified HNT and PLA nanocomposites by melt-mixing. They obtained an increment in the tensile strength of PLA from 49.5 MPa to 51.8 MPa and 55.9 MPa for 2% unmodified and modified HNT

incorporated films, respectively. According to Figure 5.29, the ultimate tensile strength of PLA was decreased from 57.2 MPa to 53.2 MPa with 2% unmodified HNT addition. On the contrary, 2% m-HNT incorporation increased the ultimate tensile strength of PLA from 57.2 to to 59.2 MPa due to better interfacial strength of APTES modified HNTs and the polymer matrix. Compared to Krishnaiah et al, in our study, similar improvement in the tensile strength was obtained with APTES modified HNT, using much lower, only 1% APTES concentration (Krishnaiah et al, 2017).

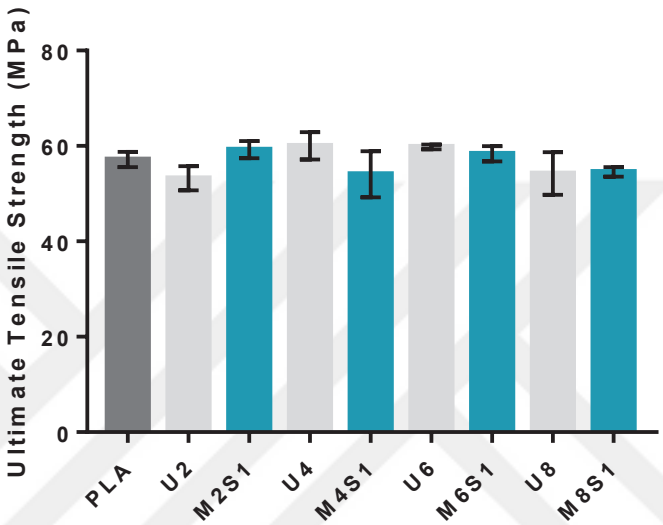

Figure 5.29. Ultimate Tensile Strength of PLA/HNT Films at Various HNT Loadings

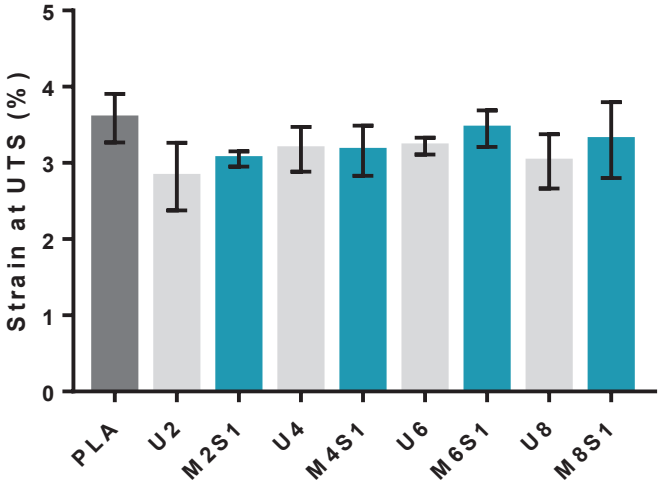

Figure 5.30. Strain at UTS of PLA/HNT Films at Various HNT Loadings

According to Figure 5.30, strain of PLA at the maximum tensile strength point was decreased with HNT addition. Modified HNT/PLA nanocomposites had better strain

than unmodified HNT incorporated ones. However, strain of the nanocomposites was not changed significantly. All strain values ranged between 2.8 and 4.4%.

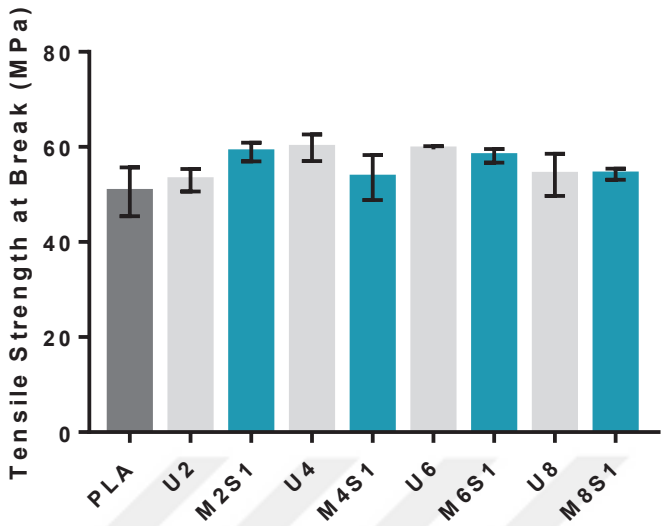

Figure 5.31. Tensile Strength at Break of PLA/HNT Films at Various HNT Loadings

Figure 5.31 includes tensile strength of PLA and the nanocomposite films at break point. Similar to Young's modulus, better interfacial adhesion was obtained by 2% m-HNT addition than 2% unmodified HNT addition. 2% HNT addition improved PLA's tensile strength at break by 4.7% while 2% m-HNT incorporation improved the tensile strength at break by 16.6% due to better interfacial affinity between the nanofiller and the polymer matrix as well as dispersion levels. Higher loadings did not improve strength at break of PLA more than 2% wt HNT and m-HNT containing nanocomposites due to HNT agglomeration.

Kim et al. prepared unmodified HNT/PLA nanocomposites by melt-mixing with 1, 3, 5, 7 and 9 % (w/w) HNT addition. Dispersion of HNT in PLA matrix was best at 5 wt% in their study according to SEM images. HNT addition resulted in a tougher behavior due to the decrease in the tensile strength and Young's modulus values with the increasing HNT content. The elongation at break and toughness values in their nanocomposites were increased up to 5 wt% HNT loading, where the interfacial interaction between the nanofiller and the polymer matrix is the best, then these values decreased for higher HNT loadings.

However, strain at break and toughness of our nanocomposites were decreased both with HNT and m-HNT incorporation (Figures 5.32 and Figure 5.33) as observed in many polymeric composites. Again, m-HNTs gave higher strain values. Essential oils can

be loaded into HNTs to improve toughness and elongation of the nanocomposites due to their plasticizing effect. Additionally, the essential oil addition may provide antimicrobial activity.

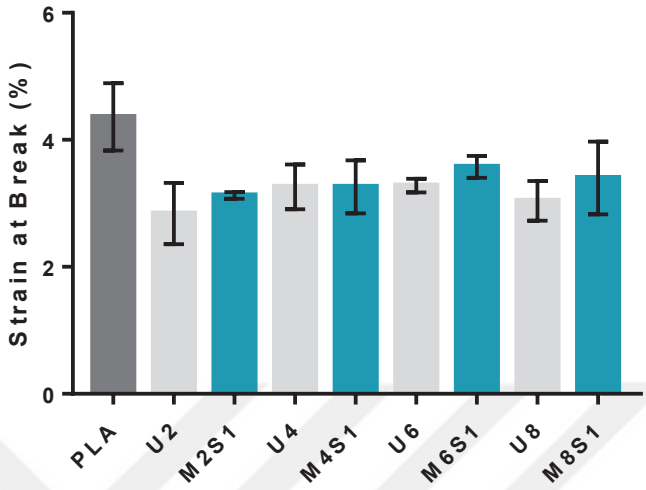

Figure 5.32. Strain at Break of PLA/HNT Films at Various HNT Loadings

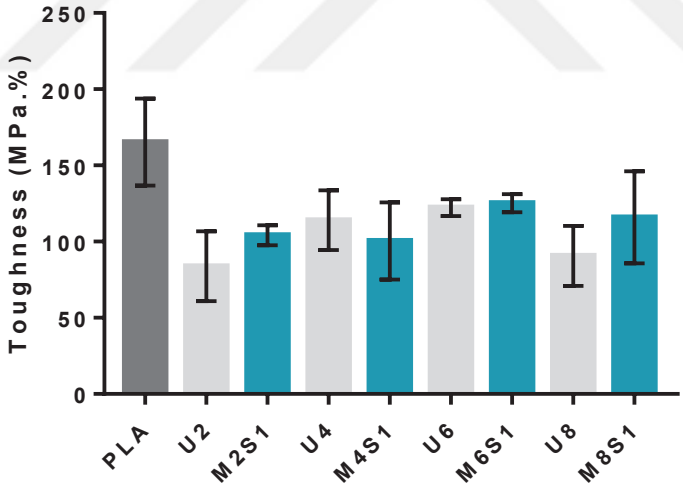

Figure 5.33. Toughness of PLA/HNT Films at Various HNT Loadings

In conclusion, halloysite addition enhanced mechanical properties of PLA films depending on HNT loading. Better mechanical properties were obtained with the incorporation of APTES modified HNTs. Best mechanical properties were reached with 2% m-HNT containing HNT/PLA nanocomposites (M2S1). In our study, HNT and m-HNT loadings higher than 2% resulted in poor dispersion and incompatibility.

De Silva et al. reported that tensile strength and tensile modulus of HNT/PLA nanocomposites produced by melt-mixing were significantly better than solution casted HNT/PLA nanocomposites (De Silva et al, 2016). Better dispersion and interfacial strength can be obtained by melt-mixing or by increasing the sonication power.

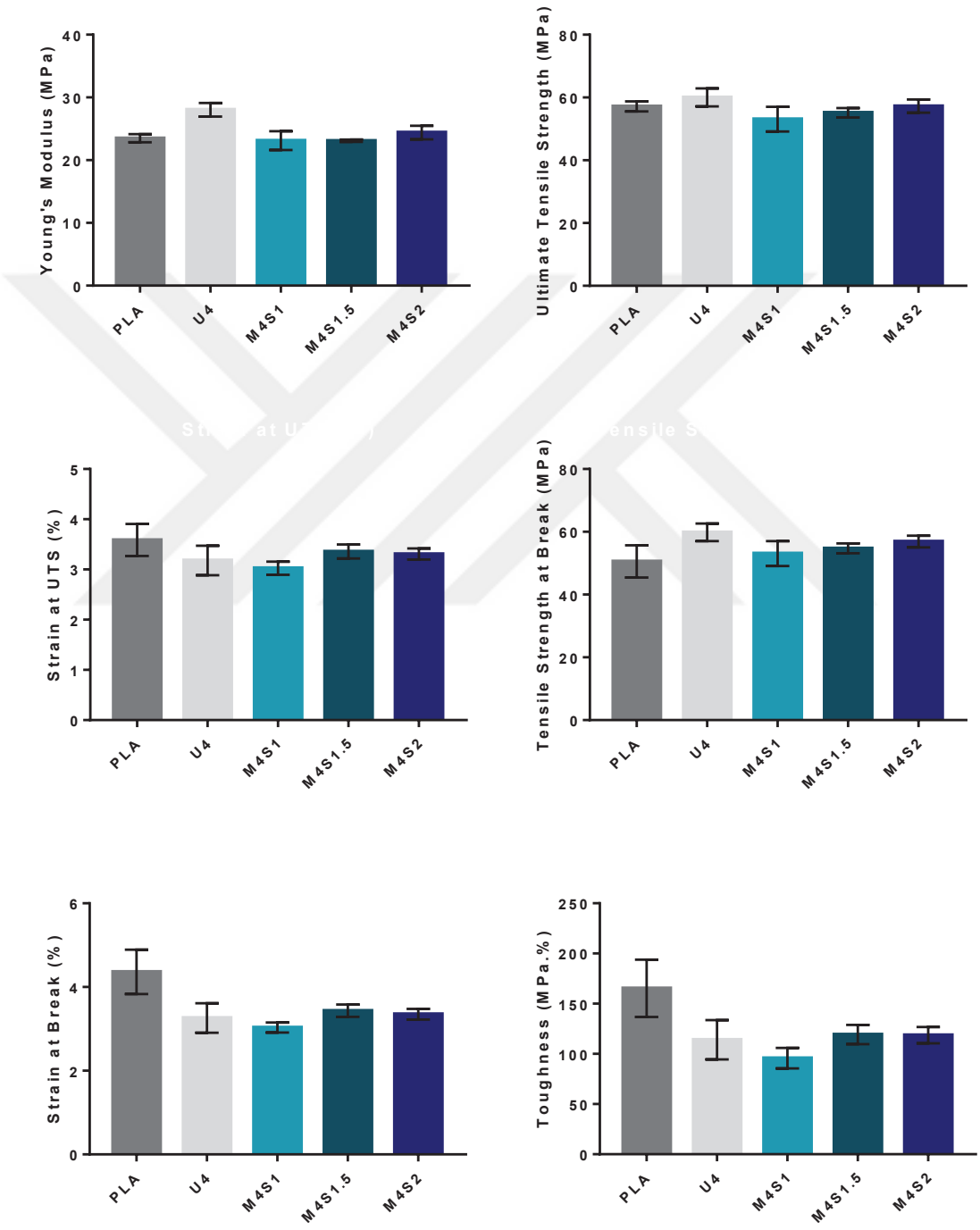

Figure 5.34. Mechanical Properties of 4 wt % HNT/m-HNT-PLA Nanocomposite Films

Figure 5.34 represents mechanical properties of 4 wt % HNT or m-HNT containing PLA nanocomposites with different APTES concentrations. According to Figure 5.34, 4 wt % HNT addition improved Young's modulus, ultimate tensile strength and tensile strength at break values. Further improvement could not be obtained with modification at 4% nanoclay loading. The decrease in strain and toughness may represent cross-linked and consequently shrunk structure for U4 and then mostly for M4S1 nanocomposites. Young's modulus, ultimate tensile strength and tensile strength at break values of APTES modified HNT containing nanocomposites were slightly increased with increasing APTES concentration. Nevertheless, there is no need to use double volume of APTES to obtain this slight improvement.

5.4.2.3. Transport Properties

Water vapor transmission rate of the nanocomposite films were measured according to ASTM F1249 standard, and water vapor permeability values were calculated.

5.4.2.3.1. Water Vapor Permeability (WVP)

Water vapor permeability of 4 wt% unmodified and modified HNTs were shown in Figure 5.35.

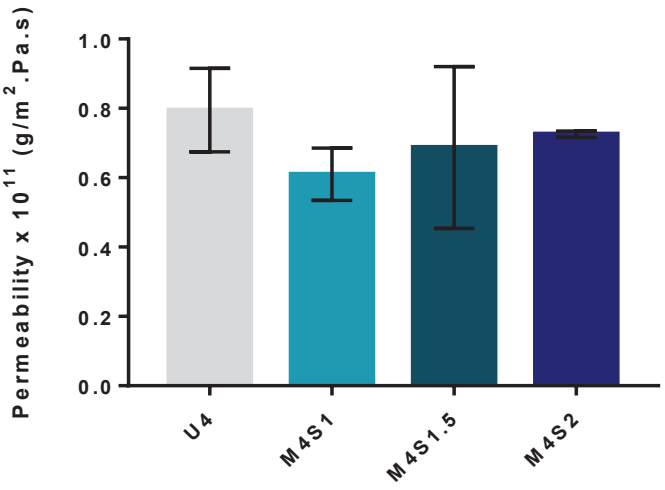

Figure 5.35. Water Vapor Permeability of the 4% wt HNT/m-HNT Containing Films

As seen in Figure 5.35, APTES modified HNT containing films have shown better barrier properties due to more uniform distribution of HNTs in PLA matrix. The best

water vapor barrier property was obtained with 1% APTES modified nanocomposite films.

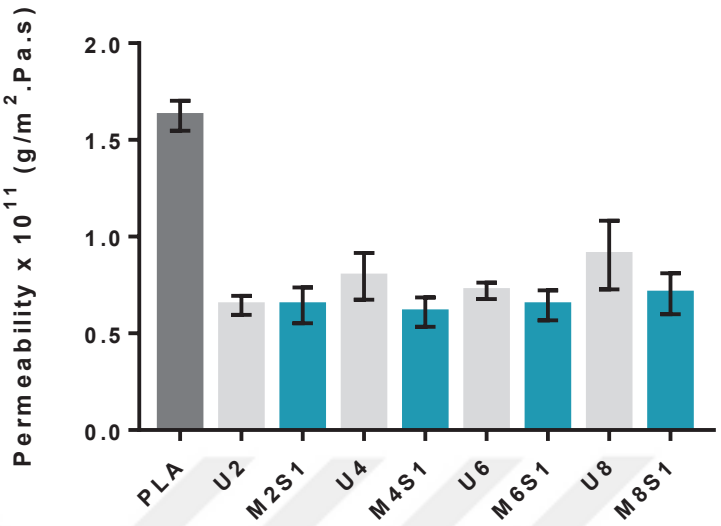

Figure 5.36. Water Vapor Permeability of PLA and Unmodified and Modified HNT Containing PLA Films

Water vapor permeability results shown in Figure 5.36 are the average of at least 2 measurements. HNT/PLA nanocomposites possessed better water vapor barrier properties than neat PLA films, due to the increased diffusion path and high aspect ratio of HNTs. Gorrasi et al. prepared HNT/PLA and 3-(trimethoxysilyl)propyl- methacrylate modified HNT/PLA nanocomposites and obtained lower WVP with m-HNTs up to 12 wt % m-HNTs while the WVP of unmodified HNT did not show significant decrease with increase from 3 wt % to 12 wt % HNTs into PLA (Gorrasi et al, 2014).

As stated in the study of Gorrasi et. al,(2014), addition of HNT into polymer decreased the diffusion and solubility of the films, therefore permeability decreased since P is the product of diffusivity (D) and solubility (S). Permeability of the nanocomposite films has decreased with the addition of modified HNT up to 6wt%. Modification of HNT's improved barrier properties of PLA as the silanization lead to better interfacial strength and more uniform distribution of HNTs in the polymeric matrix. However, the unmodified samples have only enhanced the barrier property for only 2 wt % HNT addition. Nanofiller addition was supposed to decrease WVP, contrariwise, WVP was increased after 6 wt%. Probably, the assemblage of HNTs at 8 wt% left polymer regions with lesser HNT contents compared to 6 wt% HNT containing nanocomposite. APTES

modification improved water vapor barrier property of PLA at 8 wt% too. Similar WVP values were obtained for all APTES modified nanocomposites.

5.4.2.4. Thermal Properties

Thermal properties of nanocomposites were determined by TGA and DSC analysis.

5.4.2.4.1. DSC

PLA used in this study has semi-crystalline structure. According to DSC results shown in Table 5.17, glass transition temperature (T_g) and melting temperature (T_m) of PLA was not significantly affected with HNT or m-HNT addition. Slight increase in melting temperature was noticed with addition of HNT. In compatible with XRD results, HNT addition increased crystallinity of PLA and m-HNT addition provided further increase in crystallinity of PLA films at 2% wt HNT/m-HNT concentration. Crystallinity of PLA was increased with 2% wt HNT addition by 3%, while m-HNT addition increased crystallinity by 4.9% at the same nanoclay concentration. Similar effect was observed in 4 wt% HNT and m-HNT containing nanocomposites but modification did not affected crystallinity at higher nanofiller loadings due to poor dispersion of HNT or m-HNTs.

Table 5.17. DSC Results of HNT/PLA and m-HNT/PLA Nanocomposites

	T_g	T_m	ΔH_m	X_c (%)
PLA	59.6	149.2	20.4	21.9
U2	59.6	149.8	22.7	24.9
M2S1	59.9	150.3	24.4	26.8
U4	59.6	150.0	21.1	23.6
M4S1	59.5	150.2	22.3	24.9
U6	59.8	150.4	21.2	24.2
M6S1	59.7	150.4	21.0	24.0
U8	59.8	150.6	19.5	22.8
M8S1	59.7	150.2	19.6	22.9

Krishnaiah et al. reported that crystallinity of PLA was increased with 2% HNT addition from 15.25% to 22.9%, while modification with a very high APTES concentration (24% wt) resulted in a decrease in crystallinity to 17.20% in contrary to our results.

5.4.2.4.2. TGA

Thermogravimetric changes of HNT and m-HNT containing PLA based film samples were shown in relative mass loss vs. temperature graph (Figure 5.37).

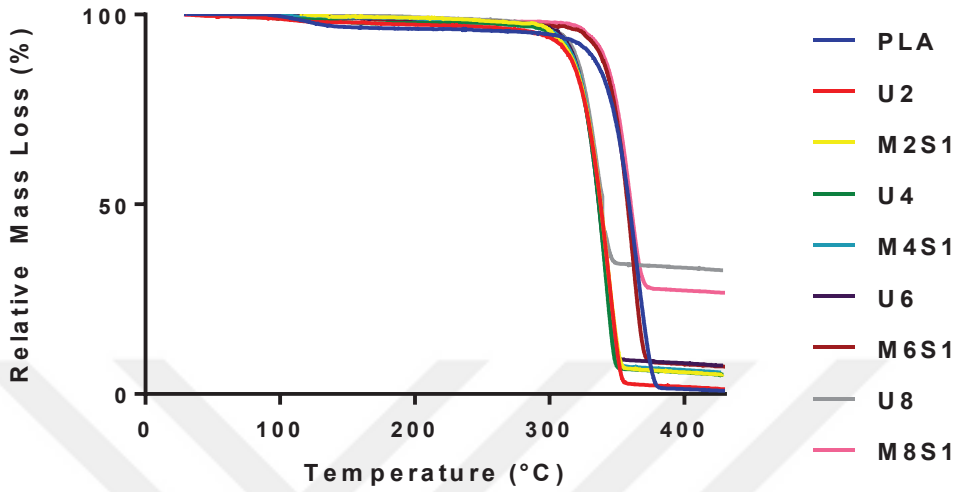

Figure 5.37. % Mass Loss of PLA/HNT and PLA/m-HNT Nanocomposite Films

According to Figure 5.37, there is one distinct mass loss peak for each film sample. This is the degradation peak for PLA. The mass loss derivative was plotted against temperature to determine peak, onset and endset temperatures and mass loss values (Figure 5.38).

Thermogravimetric properties of PLA, HNT/PLA and m-HNT/PLA nanocomposite films were listed on Table 5.18. According to Table 5.18, the degradation peak temperature was decreased by 2-3 °C for 2-4% wt HNT/m-HNT containing samples and 4-5 °C for 6-8% wt HNT/m-HNT containing samples. The increase in the temperature at 5% mass loss and the degradation peak temperature with unmodified and modified HNT addition indicates that the thermal stability of PLA was slightly decreased from 365 to 360 °C. The remaining mass percentages at maximum temperature were notably higher than the 8 wt % for U8 and M8S1 nanocomposites which represent the dispersion of unmodified and modified HNTs within PLA matrix was poor probably due to agglomerations of HNT and m-HNTs. The decrease in the degradation peak temperature may be also addressed to agglomerations of HNTs.

Although there are several studies showing that thermal properties of PLA was enhanced with HNT or m-HNT addition (De Silva et al. 2014, De Silva et al. 2016), there are also some reports in the literature that thermal properties of PLA was decreased

similar to this study (Chen et al. 2017, Krishnaiah et al. 2017, Chen at al. 2018). Additionally, the lowest onset decomposition temperature of the nanocomposite films was 330.7 °C and the process temperature of these nanocomposites is much lower than the decomposition temperatures and therefore, these nanocomposites are suitable for food packaging applications.

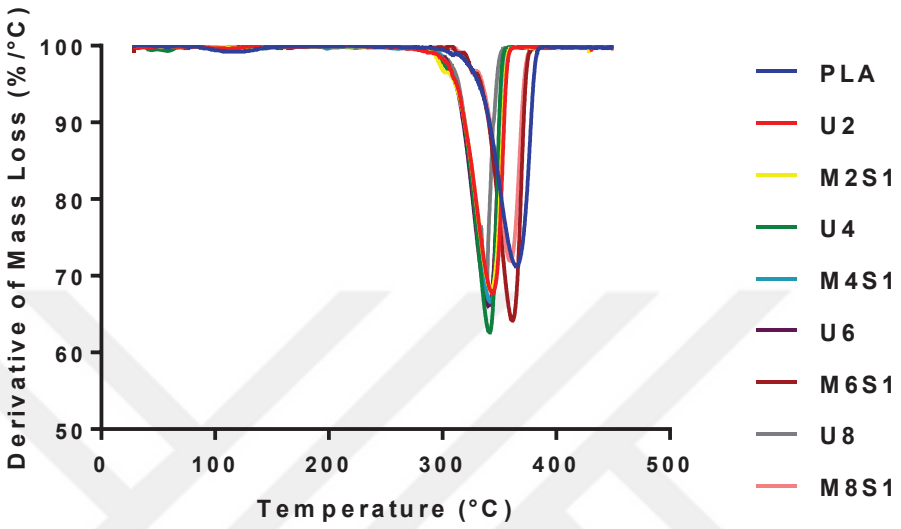

Figure 5.38. Derivative of Mass Loss vs. Temperature

Table 5.18. Thermogravimetric Properties of the Nanocomposite Films

	T at 5% Mass Loss	Onset Temperature (°C)	Degradation Peak (°C)	Remaining Mass % at Tmax
PLA	331.8	333.9	365.0	0.5
U2	307.9	330.7	362.0	1.3
M2S1	322.6	333.4	363.0	5.1
U4	321.6	335.1	361.5	5.0
M4S1	324.9	334.3	362.8	5.7
U6	327.1	332.3	360.8	7.4
M6S1	324.3	335.2	360.4	6.7
U8	328.0	344.7	359.5	32.6
M8S1	327.3	334.6	359.6	26.2

5.4.2.5. Surface Wettability

Effects of HNT loading and silane modification on the contact angle of the films were investigated. Figure 5.39 shows the effect of silane concentration on contact angle results of PLA nanocomposites containing 4 wt% HNTs. It was seen that, HNT addition

decreased the contact angle due to hydrophilicity of HNT. However, all modified samples slightly improved the hydrophilicity of HNTs. Best surface hydrophobicity was obtained with M4S1 nanocomposites that includes 1% silane modification.

Contact angle results revealed that HNT addition decreased PLA's contact angle by 7° at most. m-HNT/PLA samples provided better hydrophobicity than unmodified HNT/PLA samples. Contact angle of nanocomposite films with increasing HNT loading was not changed and also their standard deviation regions coincide with each other (Figure 5.40).

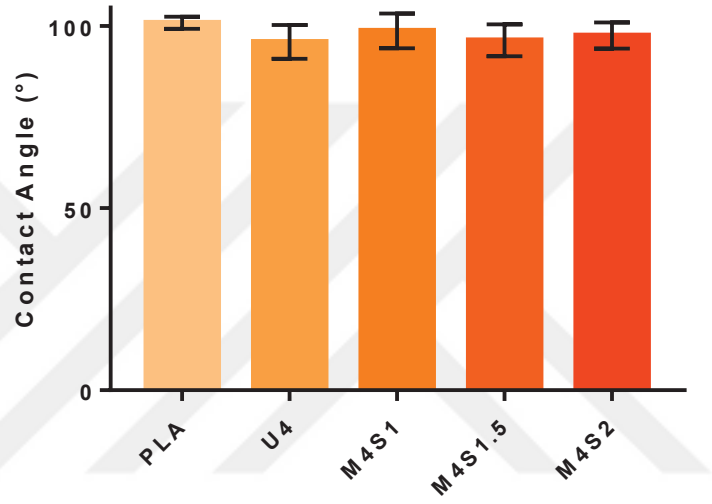

Figure 5.39. Contact Angle vs. Silane Concentration

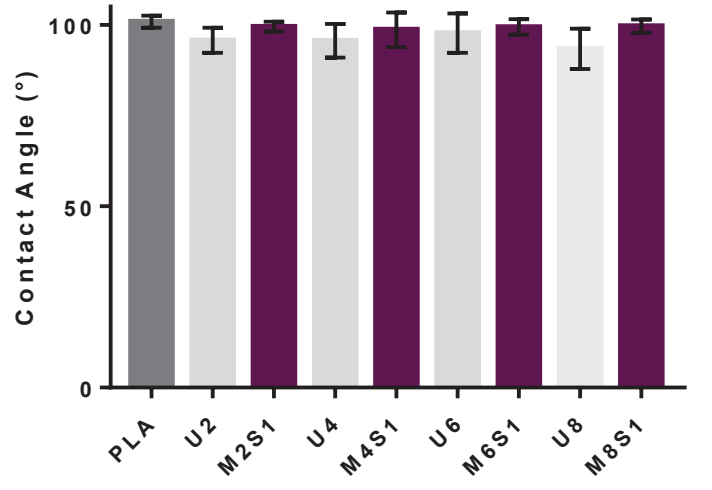

Figure 5.40. Contact Angle of PLA/HNT Nanocomposites

Chen et al. (2017) reported that the HNT addition by 2-15 wt % did not influence surface wettability of PLA significantly. The contact angle of their films had a mean value of 72.12 ± 3.7° (Chen et al, 2017). Chen et al. (2018) reported that APTES modification (with 100% (v/w) APTES and 6h of reaction time) did not influence surface wettability of PLA (74.9 ± 8°) (Chen et al, 2018). Indeed, the surface wettability of our nanocomposites was not changed much with HNT addition or APTES modification similarly to literature. Our films represented a more hydrophobic structure with an average contact angle of 97.6 ± 2.3°.

5.4.2.6. Optical Properties

Optical properties of packaging films are quite important to protect food from UV light and to enable customers to observe the food product to understand whether it is fresh or not. In addition, the change in color measurements helped the scientist to determine dispersion of clays in the nanocomposite films.

Optical properties of the prepared PLA, HNT/PLA and m-HNT/PLA films after 4-6 weeks of aging were listed on Table 5.19. As seen from the table, HNT loading into PLA matrix had slight effect on the color of the nanocomposite films.

Table 5.19. Optical Properties of the Films

	L	a	b	ΔE
PLA	86.36 ± 0.68	0.49 ± 0.04	0.95 ± 0.13	-
U2	87.17 ± 0.18	0.23 ± 0.04	2.28 ± 0.24	1.59 ± 0.21
M2S1	87.77 ± 0.60	0.36 ± 0.03	1.47 ± 0.05	1.54 ± 0.52
U4	87.86 ± 0.70	0.19 ± 0.08	1.78 ± 0.43	1.86 ± 0.49
M4S1	87.05 ± 0.28	0.28 ± 0.04	1.73 ± 0.24	1.10 ± 0.27
U6	87.45 ± 0.48	0.08 ± 0.06	2.16 ± 0.24	1.75 ± 0.16
M6S1	86.90 ± 0.10	0.19 ± 0.06	2.15 ± 0.15	1.36 ± 0.11
U8	86.53 ± 0.61	0.18 ± 0.12	2.70 ± 0.41	1.89 ± 0.43
M8S1	86.48 ± 0.19	0.05 ± 0.04	2.38 ± 0.06	1.51 ± 0.07

As known, if the total color difference (ΔE) is less than 3-4, the change in the color cannot be observed by naked human eye (Oğuzlu & Tıhmınlıoğlu, 2010). All of the nanocomposite films had ΔE values less than 2.0. Increase in HNT content slightly

increase ΔE. Organosilane modification decreased ΔE in all concentrations compared to the unmodified samples.

5.4.2.7. Morphological Properties

Morphology of the fracture surface of HNT and m-HNT containing PLA nanocomposite film samples was examined by SEM. Back-scatter images of nanocomposite film samples were represented in Figures 5.41 and 5.42.

Molecular mass differences within nanocomposites can be observed by back scatter imaging. Figure 5.41 shows fracture surfaces of PLA nanocomposite films containing 2 and 4 wt % HNTs. It is observed that although atomic masses of Al and Si atoms are greater than C atom, 2 and 4 wt% HNT and m-HNT containing samples both have shown compatibility with PLA matrix, since there was no brightness difference between HNT or m-HNT with PLA.

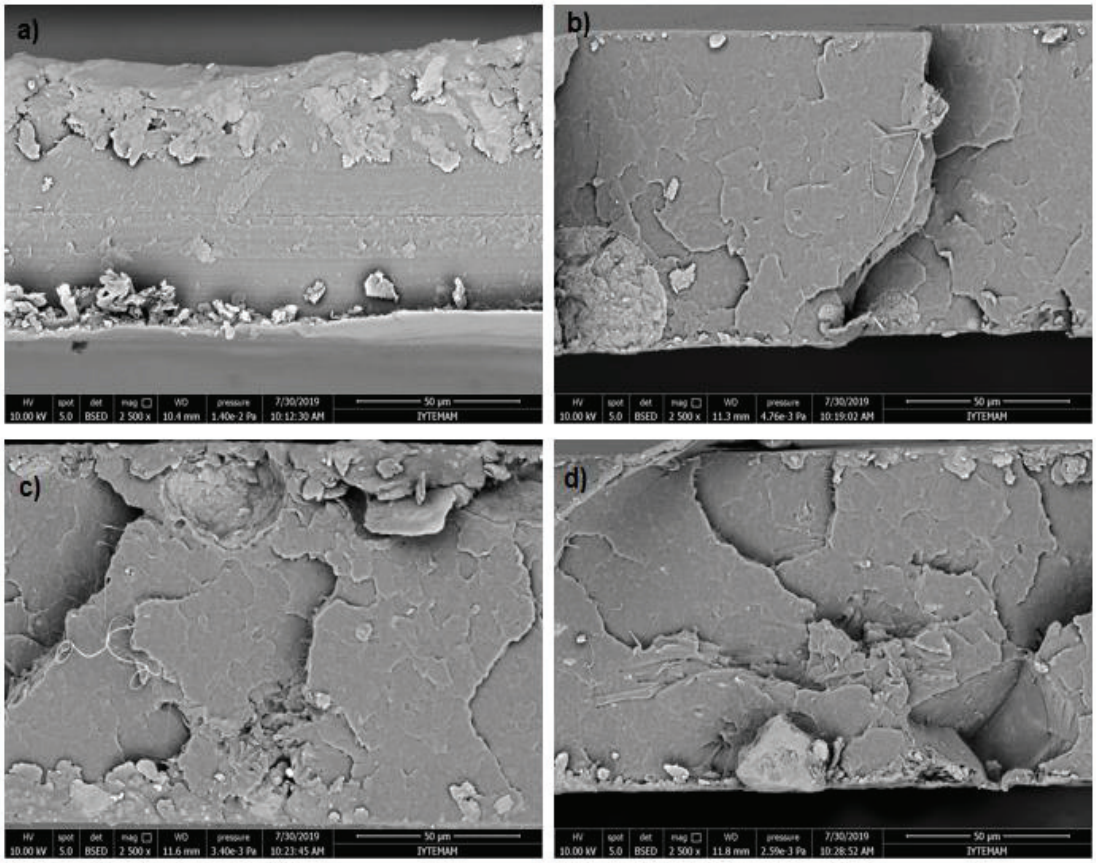

Figure 5.41. SEM Images of the Fracture Surface of the Nanocomposite Films (a) U2, (b) M2S1, (c) U4, (d) M4S1

Agglomerations of HNT and m-HNT were observed in all samples but especially for 2 wt% modified HNT loaded samples showed better dispersion and compatibility between the polymer matrix and nanotubes.

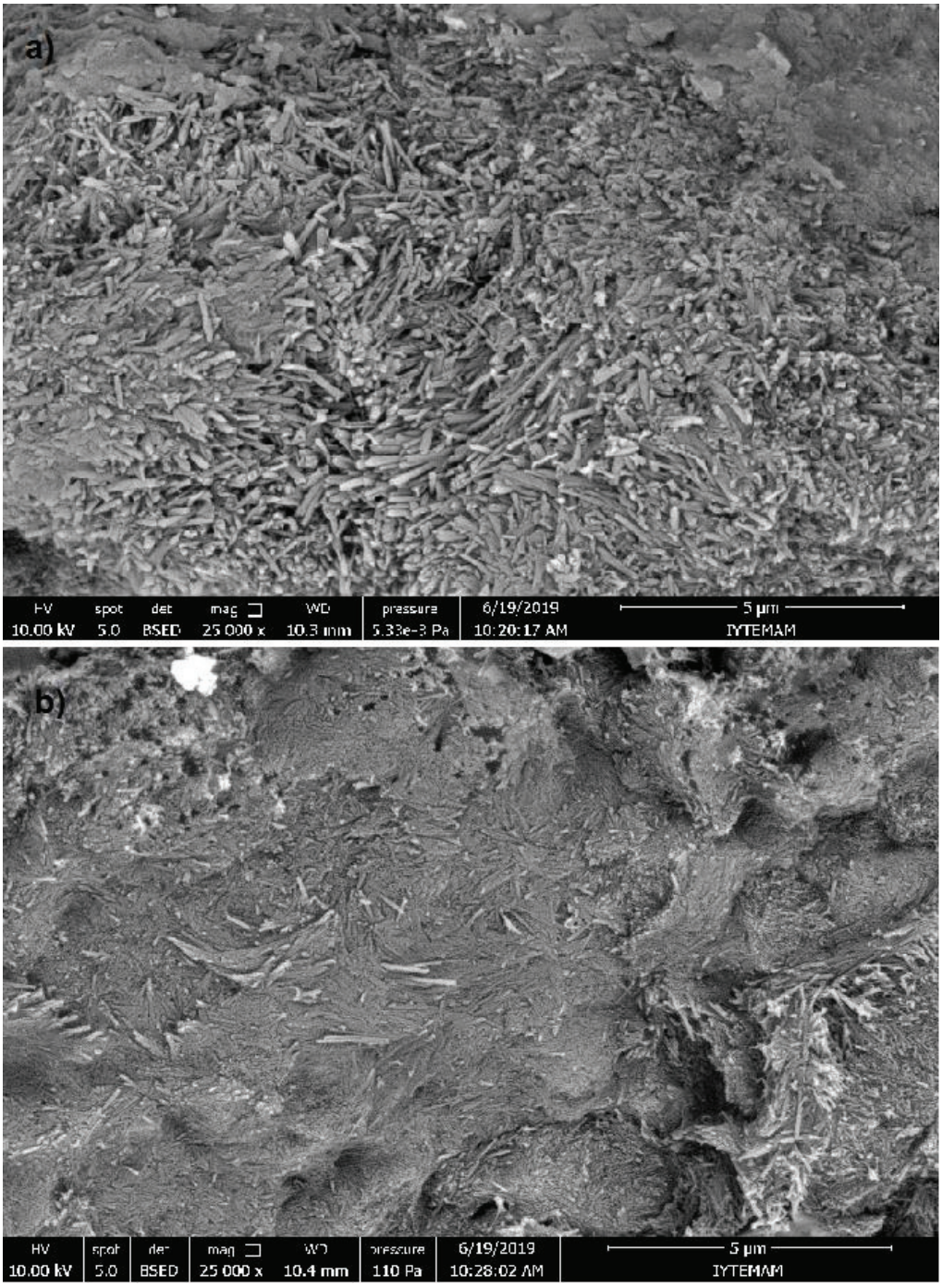

Figure 5.42. SEM Images of the Fracture Surface of the Nanocomposite Films (a) U6, (b) M6S1

According to Figure 5.42, both unmodified and modified HNTs had affinity with the polymer. U6 sample had more voids between nanotubes and PLA, than M6 sample.

Also, tubular shapes of HNTs are more visible and not embedded into PLA matrix for U6 nanocomposites. Therefore, it can be said that modified HNT sample has shown better interfacial adhesion with PLA than the unmodified HNT sample.

CHAPTER 6

CONCLUSION AND RECOMMENDATIONS

PLA is a suitable to substitute of petroleum based packaging materials due to its excellent biodegradability as well as synthesis from renewable agricultural stocks. Nanoclay addition into PLA matrix can enhance thermal, mechanical and barrier properties of PLA. HNTs are natural, tubular, layered nanoclay minerals with unique surface chemistry. Therefore, HNT can be incorporated into PLA to enhance PLA's drawbacks.

Organosilane modification is a widely used method to modify nanoadditives to enhance the compatibility between the nanoadditive and the polymer matrix. Aminopropyltriethoxysilane (APTES) is a prominent silane coupling agent to enhance interfacial strength between the filler and the polymer. As a consequence, overall properties of the nanocomposite material were improved.

In this study, HNTs were modified with APTES at different pH and APTES concentrations. Effect of sonication, drying temperature and time were investigated. PLA/HNT and PLA/mHNT nanocomposites were prepared and their mechanical and barrier properties were investigated.

HNTs were successfully modified with APTES and optimum APTES concentration was determined to be 1% (v/w). The effect of pH on the silane modification was investigated. At relatively low pH (3.50), lower APTES concentrations (1-2 wt%) are enough to catch similar properties obtained with higher concentrations (15%) at high pH values. When the overall cost of the nanocomposite is considered, it is more cost effective to use lower concentrations of silane coupling agents to obtain similar properties.

Sonication improved tensile properties of PLA. Solution casting conditions of PLA were optimized at 70 °C and 2 days of drying in a vacuum oven after drying in a fume hood. The water on PLA films should be removed quickly to prevent plasticization of PLA.

Additional peaks and chemical shifting in the FTIR, XRD and XPS spectra of the modified HNT samples prove silane bonding onto HNT surface. According to XPS results, the best silylation efficiency was reached with 2% APTES. However, the best performance for APTES modification was 1% (v/w) based on all characterization results of HNTs (FTIR and XRD results) as well as tensile, barrier and contact angle results of the nanocomposite films.

Best improvements in the properties of PLA films were obtained with 2 wt % APTES modified HNT (with 1% APTES) containing samples. Therefore, the nanocomposite films produced in this study with high transparency and good barrier property can be a suitable candidate for fresh food packaging applications.

The power of sonication can be increased for further investigation of higher HNT loadings in order to improve the dispersion levels. For antimicrobial food packaging applications, essential oils can be loaded into HNT lumen to provide antibacterial activity and to increase elongation and toughness of the nanocomposite films due to their plasticizing effect. Better tensile strength and modulus can be obtained by melt-compounding method instead of solvent casting.

REFERENCES

Abdullayev, E., Joshi, A., Wei, W., Zhao, Y., & Lvov, Y. (2012). Enlargement of Halloysite Clay Nanotube Lumen by Selective Etching of Aluminum Oxide. *ACS Nano 6*(8), 7216–7226.

Atikler, U., Preparation and Characterization of Polypropylene- Cellulose Composites, *MSc. Thesis, İzmir Institute of Technology, Chemical Engineering Department, İzmir* (2004).

Auras, R., Harte, B., & Selke, S. (2004). An Overview of Polylactides as Packaging Materials. *Macromolecular Bioscience, 4*(9) 835–864.

Barick, A. K., & Tripathy, D. K. (2011). Effect of organically modified layered silicate nanoclay on the dynamic viscoelastic properties of thermoplastic polyurethane nanocomposites. *Applied Clay Science, 52*(3), 312-321.

Barrientos-Ramírez, S., Oca-Ramírez, G. M. De, & Ramos-Fernández, E. V. (2011). Surface modification of natural halloysite clay nanotubes with aminosilanes . Application as catalyst supports in the atom transfer radical polymerization of methyl methacrylate. *Applied Catalysis A :General 406*(1-2), 22–33.

Chen, Y., Geever, L. M., Killion, J. A., Lyons, J. G., Higginbotham, C. L., & Devine, D. M. (2017). Halloysite nanotube reinforced polylactic acid composite. *Polymer Composites*, *38*(10), 2166-2173.

Chen, Y., Murphy, A., Scholz, D., Geever, L. M., Lyons, J. G., & Devine, D. M. (2018). Surface-modified halloysite nanotubes reinforced poly (lactic acid) for use in biodegradable coronary stents. *Journal of Applied Polymer Science, 135*(30), 1–13.

Cho, T. W., & Kim, S. W. (2011). Morphologies and Properties of Nanocomposite Films Based on a Biodegradable Poly (ester) urethane Elastomer. *Journal of Applied Polymer Science, 121*(3), 1622-1630.

De Silva, R. T., Soheilmoghaddam, M., Goh, K. L., Wahit, M. U., Bee, S. A. H., Chai, S. P., & Pasbakhsh, P. (2016). Influence of the processing methods on the properties of poly (lactic acid)/halloysite nanocomposites. *Polymer Composites*, *37*(3), 861-869.

Dewangan, B., & Marathe, U. (2018). Nanocomposites for Food Packaging Applications. *Novel Applications in Polymers and Waste Management*, 138–162.

Drown, E. K., Mohanty, A. K., Parulekar, Y., Hasija, D., & Harte, B. R. (2007). The surface characteristics of organoclays and their effect on the properties of poly(trimethylene terephthalate) nanocomposites. *Composites Science And Technology*, *67*, 3168–3175.

Drumright, B. R. E., Gruber, P. R., & Henton, D. E. (2000). Polylactic Acid Technology. *Advanced Materials 12*(23), 1841–1846.

Engelberg, I., & Kohn, J. (1991). Physico-mechanical properties of degradable polymers used in medical applications : a comparative study. *Biomaterials 12*, 292–304.

Erdogan, A. R., Kaygusuz, I., & Kaynak, C. (2014). Influences of Aminosilanization of

Halloysite Nanotubes on the Mechanical Properties of Polyamide-6 nanocomposites. *Polymer Composites 35*(7), 1350-1361.

Farah, S., Anderson, D. G., & Langer, R. (2016). Physical and mechanical properties of PLA , and their functions in widespread applications — A comprehensive review. *Advanced Drug Delivery Reviews*, *107*, 367–392.

Garcia-Garcia, D., Ferri, J. M., Ripoll, L., Lopez-Martinez, J., & Balart, R. (2017). Characterization of selectively etched halloysite nanotubes by acid treatment. *Applied Surface Science*, *422*, 616–625.

Garlotta, D. (2002). A Literature Review of Poly (Lactic Acid). *Journal of Polymers and Environment 9*(2), 63-84.

Glotov, A., Stavitskaya, A., Chudakov, Y., Ivanov, E., Huang, W., Vinokurov, V., Zolotukhina, A., Maximov, A., Karakhanov, E., & Lvov, Y. (2018). Mesoporous Metal Catalysts Templated on Clay Nanotubes. *Bulletin of the Chemical Society of Japan, 92*(1), 61-69.

Gorrasi, G., Pantani, R., Murariu, M., & Dubois, P. (2014). PLA/Halloysite Nanocomposite Films: Water Vapor Barrier Properties and Specific Key Characteristics. *Macromolecular Materials and Engineering*, *299*(1), 104-115.

Hanemann, T., & Szabó, D. V. (2010). Polymer-Nanoparticle Composites: From Synthesis to Modern Applications. *Materials, 3*(6), 3468-3517.

Harito, C., Bavykin, D. V, & Yuliarto, B. (2019). Polymer nanocomposites having high filler content : synthesis , structures , properties , and applications. *Nanoscale, 11*(11), 4653–4682.

He, Y., Xu, W., Tang, R., Zhang, C., & Yang, Q. (2015). pH-Responsive nanovalves based on encapsulated halloysite for the controlled release of a corrosion inhibitor in epoxy coating. *RSC Advances*, *5*(110), 90609-90620.

Hemmatpour, H., Haddadi-asl, V., & Roghani-mamaqani, H. (2015). Synthesis of pH-sensitive poly (N , N-dimethylaminoethyl methacrylate)-grafted halloysite nanotubes for adsorption and controlled release of DPH and DS drugs. *Polymer*, *65*, 143–153.

Jamshidian, M., Tehrany, E. A., Imran, M., & Jacquot, M. (2010). Poly-Lactic Acid : Production , Applications , Nanocomposites , and Release Studies. *Comprehensive reviews in food science and food safety, 9*(5), 552–571.

Jang, S. H., Jang S. R., Lee, G. M., Ryu, J. H., Park, S. I., & Park, N. H. (2017). Halloysite nanocapsules containing thyme essential oil: preparation, characterization, and application in packaging materials. *Journal of food science, 82*(9), 2113-2120.

Kim, Y. H., Kwon, S. H., Choi, H. J., Choi, K., Kao, N., Bhattacharya, S. N., & Gupta, R. K. (2016). Thermal , Mechanical , and Rheological Characterization of Polylactic Acid / Halloysite Nanotube Nanocomposites. *Journal of Macromolecular Science, Part B, 55*(7), 680-692.

Krishnaiah, P., Thevy, C., & Manickam, S. (2017). Development of silane grafted halloysite nanotube reinforced polylactide nanocomposites for the enhancement of mechanical , thermal and dynamic-mechanical properties. *Applied Clay Science*,

135, 583–595.

Lee, M. H., Seo, H., & Park, H. J. (2017). Thyme Oil Encapsulated in Halloysite Nanotubes for Antimicrobial Packaging System. *Journal of Food Science, 82*(4), 922-932.

Li, H., Zhu, X., Xu, J., Peng, W., Zhong, S., & Wang, Y. (2016). The combination of adsorption by functionalized halloysite nanotubes and encapsulation by polyelectrolyte coatings for sustained drug delivery. *RSC Advances 6*(59) 54463–54470.

Li, Y. Q., Fu, S. Y., Yang, Y., & Mai, Y. W. (2008). Facile Synthesis of Highly Transparent Polymer Nanocomposites by Introduction of Core–Shell Structured Nanoparticles. *Chemistry of Materials, 20*(8), 2637–2643.

Li, Y., Ren, P. G., Zhang, Q., Shen, T. T., Ci, J. H., & Fang, C. Q. (2013). Properties of poly (lactic acid)/organo-montmorillonite nanocomposites prepared by solution intercalation. *Journal of Macromolecular Science, Part B, 52*(8), 1041-1055.

Liu, M., Wu, C., Jiao, Y., Xiong, S., & Zhou, C. (2013). Chitosan–halloysite nanotubes nanocomposite scaffolds for tissue engineering. *Journal of Materials Chemistry B*, *1*(15), 2078–2089.

Loste, J., Lopez-Cuesta, J., Billon, L., Garay, H., & Save, M. (2019). Transparent polymer nanocomposites : An overview on their synthesis and advanced properties. *Progress in Polymer Science*, *89*, 133–158.

Luo, B., Hsu, C. E., Li, J. H., Zhao, L. F., Liu, M. X., Wang, X. Y., & Zhou, C. (2013). Nano-composite of poly (L-lactide) and halloysite nanotubes surface grafted with L-lactide oligomer under microwave irradiation. *Journal of Biomedical Nanotechnology, 9*(4), 649–658.

Luo, C., Zou, Z., Luo, B., Wen, W., Li, H., & Liu, M. (2016). Enhanced mechanical properties and cytocompatibility of electrospun poly (l -lactide) composite fiber membranes assisted by polydopamine-coated halloysite nanotubes. *Applied Surface Science*, *369*, 82–91.

Lvov, Y., Wang, W., Zhang, L., & Fakhrullin, R. (2016). Halloysite clay nanotubes for loading and sustained release of functional compounds. *Advanced Materials, 28*(6) 1227–1250.

Marsh, K., & Bugusu, B. (2007). Food packaging-roles, materials, and environmental issues. *Journal of Food Science 72*(3), R39-R55.

Mehta, R., Kumar, V., Bhunia, H., & Upadhyay, S. N. (2006). Synthesis of poly (lactic acid): a review. *Journal of Macromolecular Science, Part C: Polymer Reviews, 45*(4), 325-349.

Mohan, T. P., Devchand, K., & Kanny, K. (2017). Barrier and biodegradable properties of corn starch-derived biopolymer film filled with nanoclay fillers. *Journal of Plastic Film & Sheeting, 33*(3), 309,336.

Molinaro, S., Cruz, M., Boaro, M., Sensidoni, A., Lagazio, C., Morris, M., & Kerry, J. (2013). Effect of nanoclay-type and PLA optical purity on the characteristics of PLA-based nanocomposite films. *Journal of Food Engineering*, *117*(1), 113–123.

Oguzlu, H., & Tihminlioglu, F. (2010). Preparation and barrier properties of chitosan-layered silicate nanocomposite films. *Macromolecular Symposia, 298*(1), 91-98.

Peixoto, A., Fernandes, A., Pereira, C., Pires, J., & Cristina, F. (2016). Microporous and Mesoporous Materials Physicochemical characterization of organosilylated halloysite clay nanotubes. *Microporous and Mesoporous Materials, 219,* 145-154.

Pluta, M., Bojda, J., Piorkowska, E., Murariu, M., Bonnaud, L., & Dubois, P. (2017). The effect of halloysite nanotubes and N , N ' - ethylenebis (stearamide) on the properties of polylactide nanocomposites with amorphous matrix. *Polymer Testing*, *61*, 35–45.

Rapacz-Kmita, A., Stodolak-Zych, E., Dudek, M., Szaraniec, B., Rozycka, A., Moisalek, M., & Mandecka-Kamien, L. (2013). Degradation of nanoclay-filled polylactide composites. *Physicochemical Problems of Mineral Processing 49*(1), 91–99.

Ray, S. S., & Okamoto, M. (2003). Polymer/layered silicate nanocomposites: a review from preparation to processing. *Progress in polymer science, 28*(11), 1539-1641.

Rhim, J. W., Park, H. M., & Ha, C. S. (2013). Bio-nanocomposites for food packaging applications. *Progress in Polymer Science, 38*(10-11), 1629-1652.

Rhim, J. (2011). Effect of clay contents on mechanical and water vapor barrier properties of agar-based nanocomposite films. *Carbohydrate Polymers*, *86*(2), 691–699.

Rong, M. Z., Zhang, M. Q., & Ruan, W. H. (2006). Surface modification of nanoscale fillers for improving properties of polymer nanocomposites : a review. *Materials Science and Technology 22*(7), 787–796.

Rouf, T. B., & Kokini, J. L. (2018). Natural Biopolymer-Based Nanocomposite Films for Packaging Applications. *Bionanocomposites for Packaging Applications* (pp. 149-177).

Ruiz-Hitzky, E., Darder, M., & Alcantara, A. C. S. (2014). Recent advances on fibrous clay-based nanocomposites. *Organic-Inorganic Hybrid Nanomaterials* (pp. 39-86).

Scarfato, P., Acierno, D., & Russo, P. (2015). Photooxidative weathering of biodegradable nanocomposite films containing halloysite. *Polymer Composites*, *36*(6), 1169-1175.

Schadler, L. S., Brinson, L. C., & Sawyer, W. G. (2007). Polymer Nanocomposites : A Small Part of the Story. *Jom, 59*(3), 53–60.

Schmidt, D., Shah, D., & Giannelis, E. P. (2002). New advances in polymer/layered silicate nanocomposites. *Current Opinion in Solid State and Materials Science, 6*(3), 205–212.

Shafiq, M., Yasin, T., & Saeed, S. (2011). Synthesis and characterization of linear low-density polyethylene/sepiolite nanocomposites. *Journal of Applied Polymer Science, 123*(3), 1718-1723.

Shen, V. K., Siderius, D. W., Krekelberg, W. P., and Hatch, H. W., Eds., NIST Standard Reference Simulation Website, NIST Standard Reference Database Number 69, National Institute of Standards and Technology, Gaithersburg MD, 20899,

https://doi.org10.18434/T4D303, (retrieved 26.07.2019).

Shi, Y., Tian, Z., Zhang, Y., Shen, H., & Jia, N. (2011). Functionalized halloysite nanotube-based carrier for intracellular delivery of antisense oligonucleotides. *Nanoscale Research Letters, 6*(1), 608.

Sing, K. S. W. (1985). Reporting physisorption data for gas/solid systems with special reference to the determination of surface area and porosity (Recommendations 1984). *Pure and Applied Chemistry, 57*(4), 603-619.

Sonchaeng, U., Iniguez-Franco, F.,Auras, R., Selke, S., Rubino, M., & Lim, L. T. (2018). Poly (lactic acid) mass transfer properties. *Progress of Polymer Science 86*, 85–121.

Sorrentino, A., Gorrasi, G., & Vittoria, V. (2007). Potential perspectives of bio-nanocomposites for food packaging applications. *Trends in Food Science and Technology, 18*(2), 84-95.

Strange, M., Plackett, D., Kaasgaard, M., & Krebs, F. C. (2008). Biodegradable polymer solar cells. *Solar Energy Materials and Solar Cells, 92*(7), 805–813.

Sun, L.; Boo, W.J.; Clearfield, A.; Sue, H.J.; Pham, H.Q. Barrier properties of model. *Epoxy Nanocomposites, Journal of Membrane Science, 2008, 318*(1-2), 128-136.

Sun, P., Liu, G., Lv, D., Dong, X., Wu, J., & Wang, D. (2015). Effective activation of halloysite nanotubes by piranha solution for amine modification via silane coupling chemistry. *RSC Advances*, *5*(65), 52916-52925.

Suppakul, P., Miltz, J., Sonneveld, K., & Bigger, S. W. (2003). Active packaging technologies with an emphasis on antimicrobial packaging and its applications. *Journal of Food Science, 68*(2), 408-420.

Tayal, A.; & Khan, S. A. (2000). Degradation of a water-soluble polymer: molecular weight changes and chain scission characteristics. *Macromolecules, 33*(26), 9488-9493.

Thangavelu, K., & Subramani, K. B. (2016). Sustainable Biopolymer Fibers — Production , Properties and Applications. *Sustainable Fibres for Fashion Industry* (pp. 109-140)

Thuo, M., Oyola-Reynoso, S., Wang, Z., Chen, J., Çınar, S., Chang, B. (2015). Revisiting the Challenges in Fabricating Uniform Coatings with Polyfunctional Molecules on High Surface Energy Materials. *Coatings 5*(4), 1002–1018.

Tsai, F., Li, P., Liu, Z., Feng, G., Zhu, P., Wang, C., Yeh, J. (2012). Drawing and ultimate tenacity properties of polyamide 6 / attapulgite composite fibers. *Journal of Applied Polymer Science, 126*(6), 1906-1916.

Waché, R., Klopffer, M., Gonzalez, S., Waché, R., Klopffer, M., Gonzalez, S., Gonzalez, S. (2015). Characterization of polymer layered silicate nanocomposites by rheology and permeability methods : impact of the interface quality. *Oil & Gas Science and Technology-Revue d'lFP Energies nouvelles, 70*(2), 267-277.

Wang, R., Li, Z., Wang, Y., Liu, W., Deng, L., Jiao, W., & Yang, F. (2013). Effects of modified attapulgite on the properties of attapulgite/epoxy nanocomposites. *Polymer Composites, 34*(1), 22-31.

Wu, W., Cao, X., Zhang, Y., & He, G. (2013). Polylactide/halloysite nanotube nanocomposites : thermal , mechanical properties , and foam processing. Journal of *Applied Polymer Science, 130*(1), 443–452.

Xu, W., Luo, B., Wen, W., Xie, W., Wang, X., Liu, M., & Zhou, C. (2015). Surface modification of halloysite nanotubes with l-lactic acid: An effective route to high-performance poly (l-lactide) composites. *Journal of Applied Polymer Science, 132*(7).

Yu, J. H., Hsieh, A. J., & Rutledge, G. C. (2010). Novel Transparent PMMA Composites for Optical Tagging. (No. ARL-TR-5354) (Army Research Lab Aberdeen Proving Ground MD Weapons And Materials Research Directorate).

Yuan, P., Southon, P. D., & Liu, Z. (2012). Organosilane functionalization of halloysite nanotubes for enhanced loading and controlled release. *Nanotechnology, 23*(37), 375705.

Yuan, P., Southon, P. D., Liu, Z., Green, M. E. R., Hook, J. M., Antill, S. J., & Kepert, C. J. (2008). Functionalization of halloysite clay nanotubes by grafting with γ - aminopropyltriethoxysilane. *The Journal of Physical Chemistry C, 112*(40), 15742–15751.

Yuan, P., Tan, D., Annabi-Bergaya, F., Yan, W., Fan, M., Liu, D., & He, H. (2012). Changes in structure , morphology , porosity , and surface activity of mesoporous halloysite nanotubes under heating. *Clays and Clay Minerals, 60*(6), 561–573.

Zeng, G., He, Y., Zhan, Y., Zhang, L., Shi, H., & Yu, Z. (2016). Preparation of a Novel Poly(vinylidene fluoride) Ultra filtration Membrane by Incorporation of 3‐Aminopropyltriethoxysilane-Grafted Halloysite Nanotubes for Oil/Water Separation. *Industrial and Engineering Chemistry Research, 55*(6), 1760-1767.

Zhang, X., Guo, R., Xu, J., Lan, Y., & Jiao, Y. (2015). Poly (L-lactide)/ halloysite nanotube electrospun mats as dual-drug delivery systems and their therapeutic efficacy in infected full-thickness burns. *Journal of Biomaterials Applications, 30*(5), 512–525.

Zhang, Y., He, X., Ouyang, J., & Yang, H. (2013). Palladium nanoparticles deposited on silanized halloysite nanotubes: synthesis, characterization and enhanced catalytic property. *Scientific Reports, 3,* 2948.

WEB_1 http://phantomplastics.com/functional-fillers/halloysite/

APPENDIX A

FTIR & SEM RESULTS

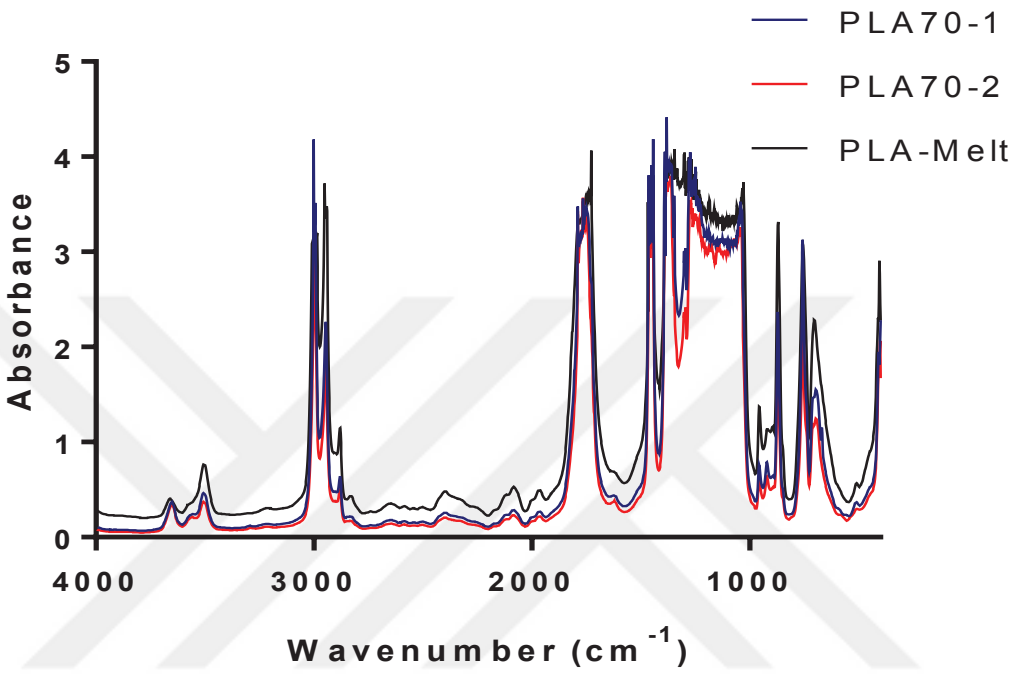

Figure A1. FTIR Spectra of 70-1, 70-2 and melt PLA

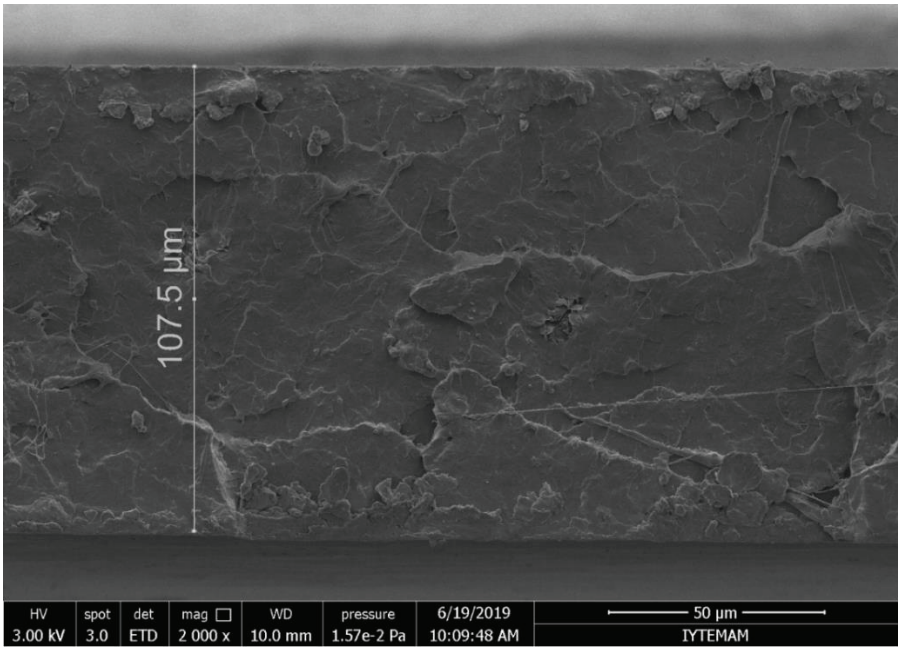

Figure A2. SEM Image of Fracture Surface of PLA